Nd:YAG LASER LAB EXPERIMENTS

by

Edward A. Teppo
Laser Designator/Rangefinder Branch
Infrared Systems Division
Weapons Development Department

This is an informal report containing preliminary information. It is not an official report of the Naval Weapons Center and must not be used as a basis for action unless enclosed in official correspondence in which the purpose of the transmittal is made clear.

NAVAL WEAPONS CENTER

China Lake, California

93555

82 11 10 077

Nd:YAG LASER LAB EXPERIMENTS

by

Edward A. Teppo
Laser Designator/Rangefinder Branch
Infrared Systems Division
Weapons Development Department

7/4) 939-3341

Approved: *[signature]*

D. C. IWAMURA, *Head*
Laser Designator/Rangefinder Branch

CONTENTS

INTRODUCTION

A compilation of the unclassified Nd:YAG laser lab experiments and related analyses performed in the Laser Designator/Rangefinder Branch, Naval Weapons Center, China Lake, Calif., during the period October 1970–December 1971 is presented. The Nd:YAG laser lab was initiated by the author in October 1970 and, hence, some of the tests performed were necessarily of an introductory nature. To expedite the preparation of this report, the author's memoranda with only minor modifications are provided as appendixes.

The purposes of the Nd:YAG laser lab effort follow:

1. Perform tests and analyses toward optimization of Nd:YAG laser system design and performance with emphasis on the laser resonator;

2. Test new promising laser materials and design concepts;

3. Perform incoming inspection of laser components;

4. Support the in-house designator/rangefinder design effort;

5. Increase awareness of laser design constraints and limitations due to state-of-the-art in laser technology;

6. Improve state-of-the-art whenever possible.

The two most important properties of a Q-switched Nd:YAG laser are its efficiency and its raw-beam divergence. Hence, most of the laser lab effort has been directed toward improving and understanding those dependent variables that dictate the laser efficiency and beam divergence.

The subject matter has been arranged into the appendixes listed.

Appendix A: Resonator Component Evaluation
Appendix B: Flashlamps and Flashlamp-Drive Circuit Design
Appendix C: Pump Cavity Design
Appendix D: Q-Switching of Lithium Niobate Modulator
Appendix E: Resonator Output Properties

Appendix F: Beam Uniformity Tests
Appendix G: Laser Coolant Studies
Appendix H: Related Subjects

In most cases, clarifying notes have been added at the end of the individual appendixes to aid the reader in understanding the terminology used and to relate the subject matter to other enclosed appendixes.

For the most part, the laser lab tests were made at a 10-Hz pulse-repetition rate with an 8-J/pulse input level.

Finally, considerable laser design effort is in progress; these areas of investigation are identified in Appendix H.

Appendix A
RESONATOR COMPONENT EVALUATION

Appendix A.1

CALCITE PRISM IN RESONATOR DESIGN

1. The portable designator (PD) resonator layout is being modified to reduce its weight, cost, complexity, and length. The anticipated over-all length is less than 7.5 inches. The new resonator design is for a lightweight laser quite unlike the PD. Some of the PD resonator com-ponents are being used in the lightweight unit to reduce its cost and development time.

2. Among the resonator components considered for modification was the 40-deg calcite prism. Described here are the angle of minimum deviation, the fold mirror incidence angle, and the output beam-to-resonator opti-cal-axis beam separation, both in angle and magnitude per unit length, as a function of the calcite prism wedge angle. The insertion loss effects of reflection from high incidence angle AR-coated surfaces will not be considered here. This topic will be pursued later should a larger wedge angle prism appear desirable from the resonator layout standpoint.

3. Figure A.1-1 gives the angle of minimum deviation for the principal ray as a function of the wedge angle. Since the resonator is being designed so that the resonator optical axis through the laser rod and the modulator are parallel, the incidence angle of the radiation at the fold mirror is one-half of the prism deviation angle. Since the radia-tion travels within the prism parallel to the prism base, the prism base is oriented at this same angle; i.e., one-half of the deviation angle from the optical axis of the resonator. As the wedge angle increases, the resonator length can be shortened, but it is also widened. The pumping cavity length in the present design establishes the resonator length.

4. Figure A.1-2 shows the difference angle between the resonator optical axis and the output beam. The larger the wedge angle, the larger the deviation angle and the larger the difference angle. The magnitude of the difference angle establishes at what distance from the prism the resonator beam and the output beam are fully separated.

5. Figure A.1-3 gives the separation of the centerline of the beams per inch of distance from the prism center.

6. The equation for the angle of minimum deviation is given by

$$n_p = [\sin (\psi + \Phi)/2]/(\sin \Phi/2) \tag{a}$$

$$n_p = (\sin \psi/2 \cos \Phi/2 + \cos \psi/2 \sin \Phi/2)/\sin \Phi/2 \tag{b}$$

$$n_p = \sin \psi/2 \cot \Phi/2 + \cos \psi/2 \tag{c}$$
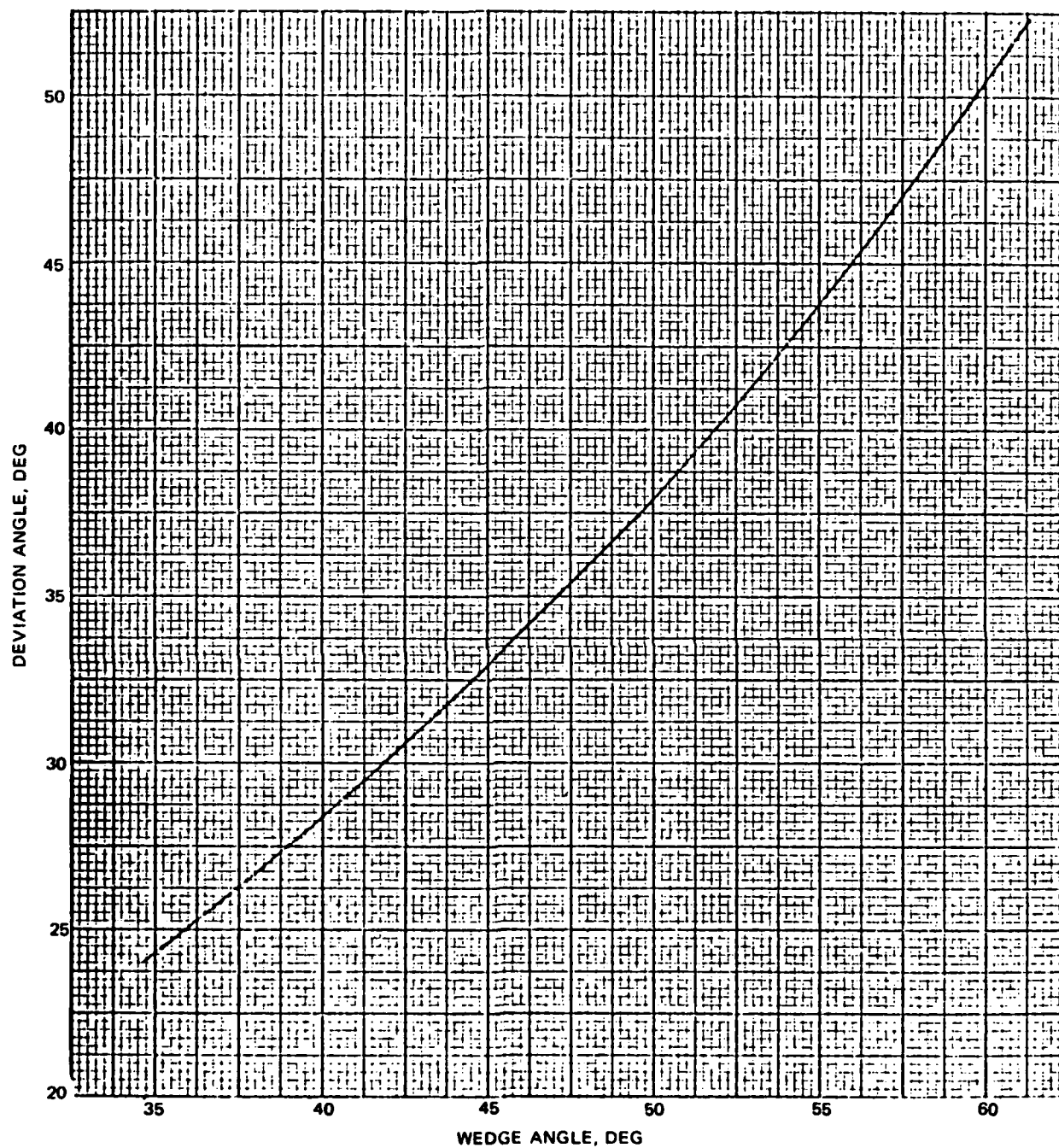
FIG. A.1-1. Angle of Minimum Deviation Versus Wedge Angle.
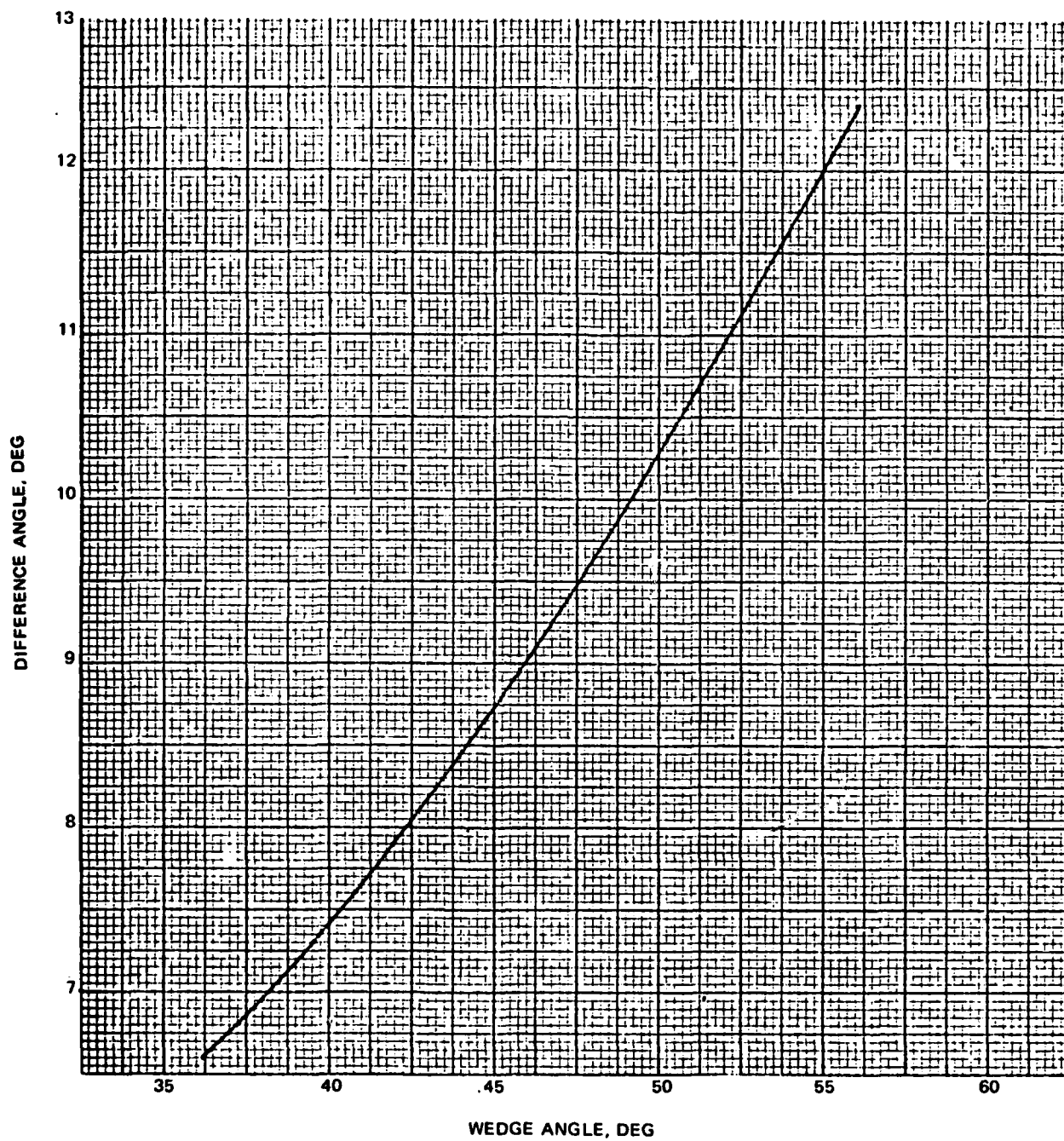
FIG. A.1-2.   Difference Angle Versus Wedge Angle.
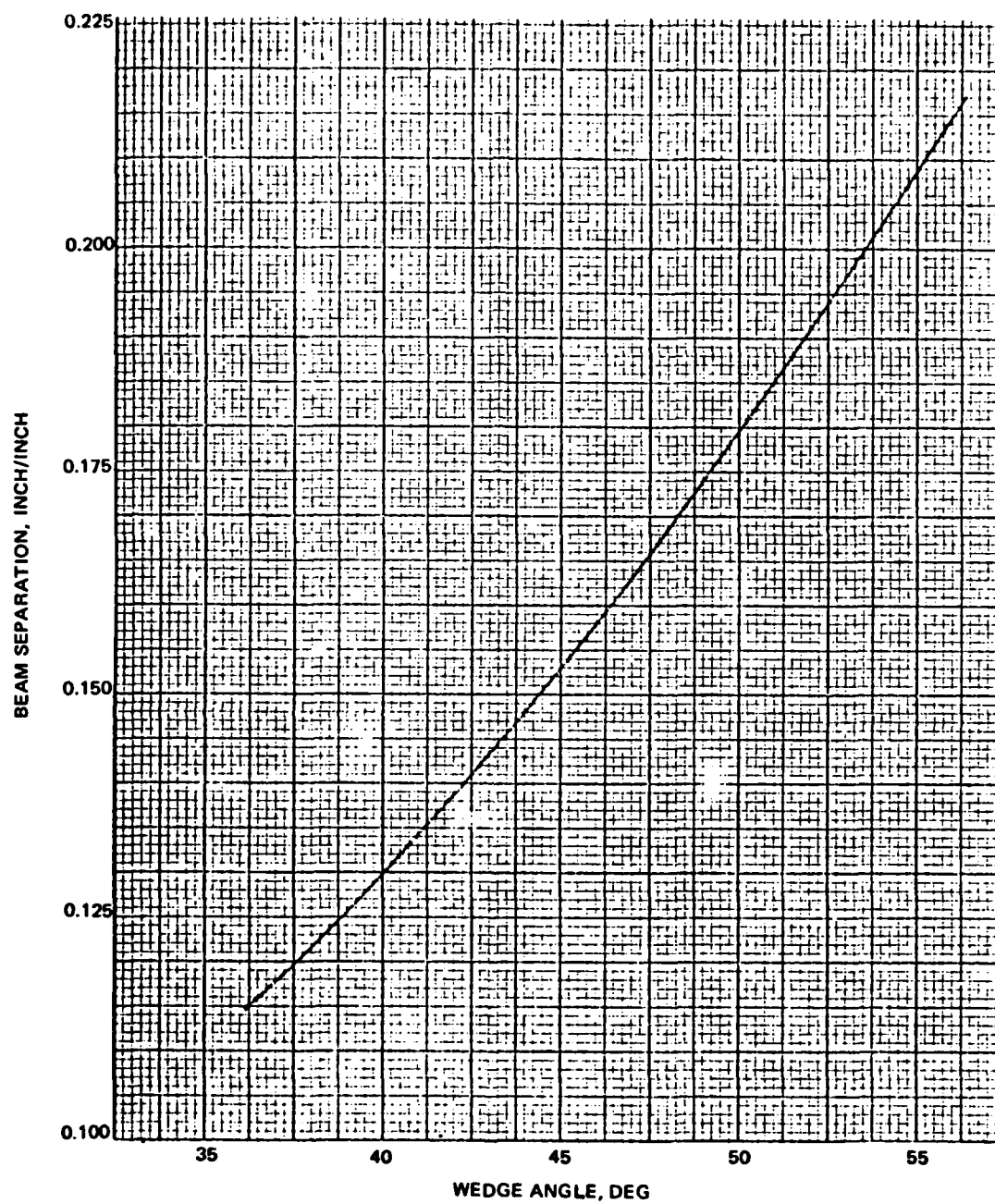
FIG. A.1-3. Beam Separation Versus Wedge Angle.

$$\tan \Phi/2 = (\sin \psi/2)/(n_p - \cos \psi/2) \tag{d}$$

which is plotted in Fig. A.1-1.

7. From the geometry given in Fig. A.1-4,

$$\sin (\psi + \Phi)/2 - n_s \sin \beta; \ 2\Theta = \psi + \Phi \tag{e}$$
$$90° - \beta + \Phi + \gamma = 180°$$
$$\gamma = 90° + \beta - \Phi; \ 90° - \gamma = \Phi - \beta \tag{f}$$
$$n_s \sin (\Phi - \beta) = \sin \eta \tag{g}$$

FIG. A.1-4.

The deviation angle is given by

$$\psi' = \Phi - \beta + \eta - (90° - \gamma) \qquad \text{(h)}$$

$$\psi' = (\psi - \Phi)/2 + \sin^{-1} [n_s \sin (\Phi - \beta)] \qquad \text{(i)}$$

where β is derivable from e. But we also have

$$n_p \sin \Phi/2 = \sin (\psi + \Phi)/2 \qquad \text{(j)}$$

$$\psi = 2 \sin^{-1} (n_p \sin \Phi/2) - \Phi \qquad \text{(k)}$$

$$d\psi = \psi - \psi', \text{ the difference angle} \qquad \text{(l)}$$

$$d\psi = (\psi + \Phi)/2 - \sin^{-1} [n_s \sin (\Phi - \beta)]$$

$$d\psi = \sin^{-1} (n_p \sin \Phi/2) - \sin^{-1} [n_s \sin (\Phi - \beta)] \qquad \text{(m)}$$

which is plotted in Fig. A.1-2.

8. The beam separation d at a distance s can be found from the law of cosines:

$$d^2 = s^2 + s^2 - 2s^2 \cos (\psi' - \psi) \qquad \text{(n)}$$

$$d = 1.414s [1 - \cos (\psi' - \psi)]^{\frac{1}{2}} \qquad \text{(o)}$$

which is plotted in Fig. A.1-3.

9. Table A.1-1 shows the data points derived to plot the data of Fig. A.1-1 through A.1-3.

10. The data provided here apply only to calcite prisms at 1.06 microns.

TABLE A.1-1. Plotting Table.

Deviation angle, ψ	Wedge angle, Φ	Difference angle, $\psi - \psi'$	Beam separation, inch/inch
25°	36°00'	6°35'	0.115
30°	41°52'	7°56'	0.138
35°	47°10'	9°23'	0.164
40°	51°54'	10°54'	0.190
45°	56°04'	12°25'	0.216

NOTES:

1. The modified resonator discussed resulted in what has become known as the "T-beam" and is discussed in A.2 of Appendix A.

2. The beam separation d established in paragraph 8 and shown in Fig. A.1-3 is not exact but is an acceptable approximation. The beam separation value determines how close the output fold mirror can be placed to the calcite prism using the 2-element, time-varying reflectance resonator (TVR).

3. The data supplied here were used in the placement of the output fold mirror in the T-beam resonator. The T-beam resonator uses a 40-deg calcite prism.

Appendix A-2

T-BEAM RESONATOR LAYOUT
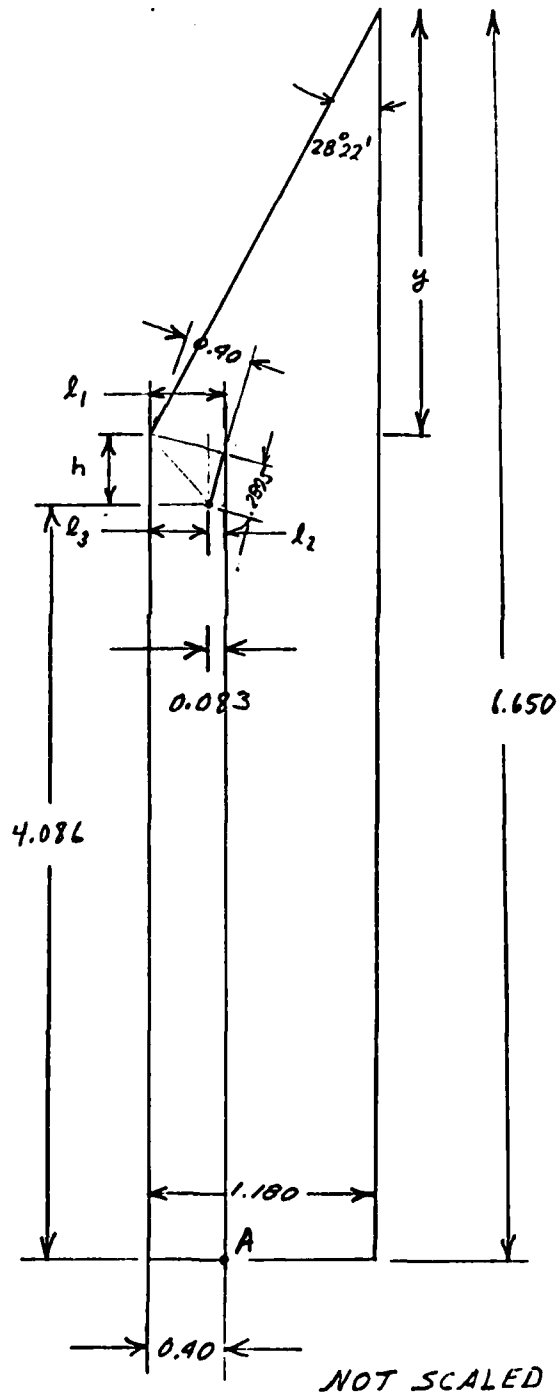
FIG. A.2-1.

Geometrics

1. $\tan 28°22' = \dfrac{1.180}{y}$

    $y = (1.180)\cot 28°22' = (1.180)(1.852) = 2.185$

2. $\cos 14°11' = \ell_1/0.400$

    $\ell_1 = (0.400)\cos 14°11' = (0.400)(.9695) = 0.3878$

3. $\sin 14°11' = \ell_2/0.2895$

    $\ell_2 = (0.2895)\sin 14°11' = (0.2895)(.2450) = 0.07093$

4. $\ell_3 = \ell_1 - \ell_2 = 0.3878 - 0.0709 = 0.3169$

5. The displacement of the prism mount corner from the 0.400 REF dimension is then

    $d = 0.400 - 0.3169 = 0.0831$

6. Its location is also needed vertically. Then

    $h^2 + \ell_3{}^2 = (0.40)^2 + (0.2895)^2$

    $h^2 = 0.1600 + 0.0838 - 0.1004 = 0.1434$

    $h = 0.3787$

7. So from the REF plate, it lies at

    $D = 6.650 - y - h = 6.650 - (y + h) = 6.650 - 2.564$

    $D = 4.086$

8. This, then, defines the corner of the calcite prism mount with respect to the inner end-plate surface and the main beam channel surface, with respect to a position in space, at A.

Resonator Design Check

1. $\cos 14°11' = 0.294/\ell_2$

   $\ell_2 = 0.294/\cos 14°11' = \dfrac{0.2940}{0.96952}$

   $\ell_2 = 0.30324$

2. $\sin 14°11' = \ell_1/\ell_2$

   $\ell_1 = \ell_2 \sin 14°11'$

   $\ell_1 = (0.30324)(0.245)$

   $\quad = 0.0743$

3. $\sin 14°11' = \dfrac{\ell_3}{0.235 - \ell_1}$

   $\ell_3 = (0.235 - \ell_1)\sin 14°11'$

   $\quad = (0.1607)(0.245)$

   $\ell_3 = 0.0394$

Therefore the reference length is

   $6.650 + \ell_2 + \ell_3$

   $= 6.650 + 0.30324 + 0.0394$

   $= 6.9926$

Block length = 7.287

FIG. A.2-2.

ENERGY OUTPUT DIRECTION
(IF END DUMP)

END REFLECTOR
(OR DUMP MIRROR)

END REFLECTOR

QUARTER-WAVE PLATE
POSITION (IF USED)

MODULATOR

ALIGNMENT WEDGES

ENERGY OUTPUT DIRECTION
(2-ELEMENT TVR)

DUMP MIRROR

(IF NOT END-DUMP
CONFIGURED)

PUMP CAVITY

TOP VIEW

CALCITE PRISM

FOLD MIRROR
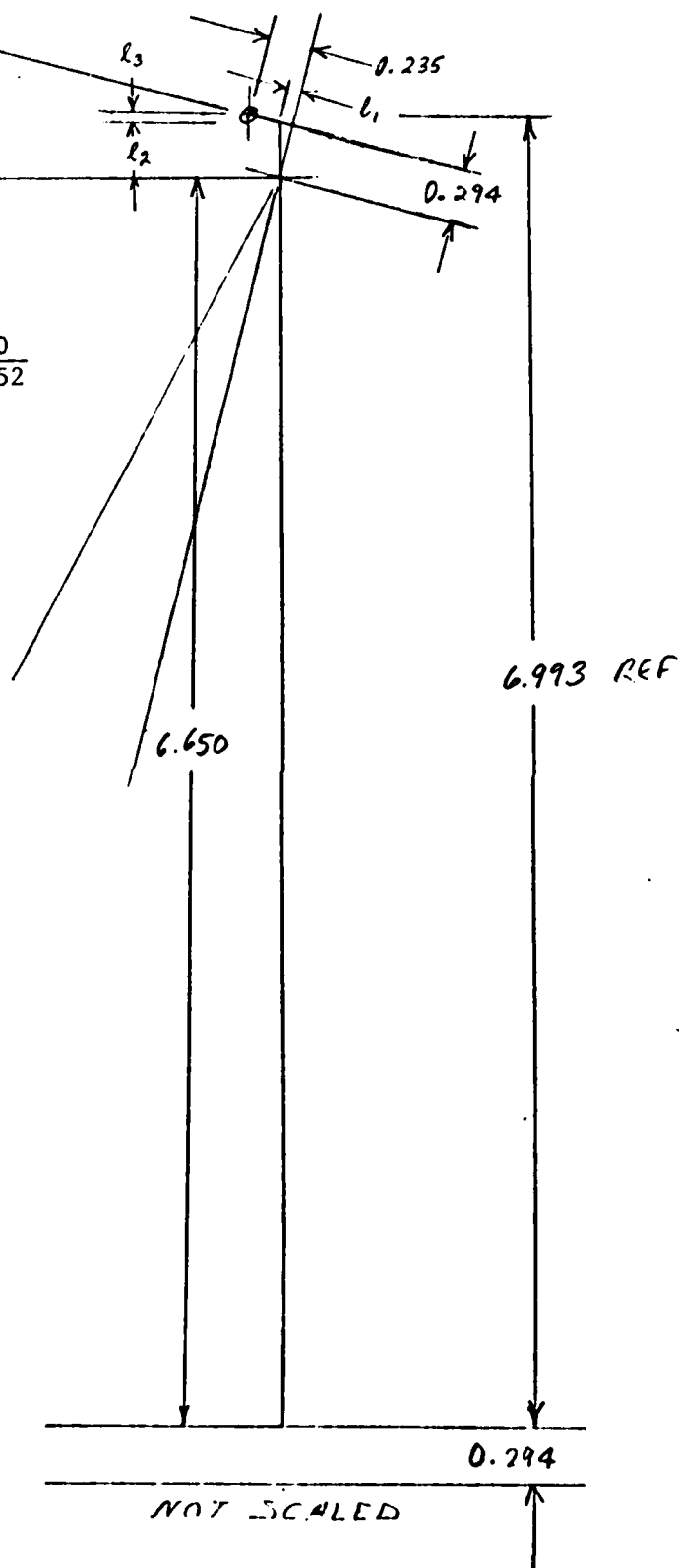
FIG. A.2-3. Assembled T-Beam Layout.
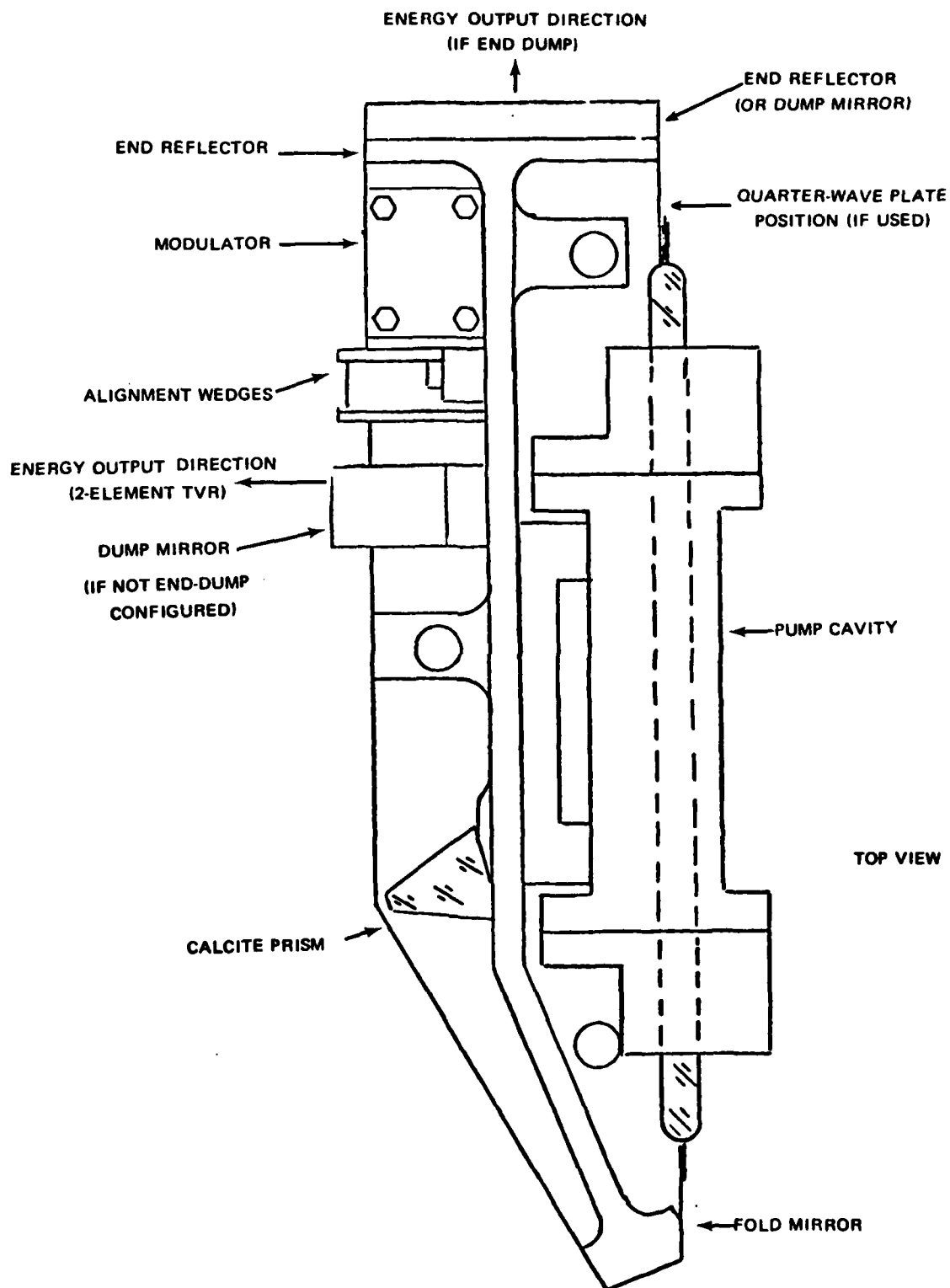
NOTES:

1. Figures A.2-1 and A.2-2 show the dimensions and initial calculations made to define the T-beam layout.

2. Figure A.2-3 shows the T-beam configuration resulting from these prior calculations and shows the resonator components installed on the T-beam structure.

3. Thermal stability tests on the T-beam resonator are given in E.2.

4. The assembled T-beam resonator weighs 14 ounces.

Appendix A-3

AN IMPROVED CORRECTING PRISM

1. The PD resonator uses a 40° calcite prism as the polarizing element. The dispersion of calcite causes the angle of deviation for different wavelengths to vary, the longest wavelength of radiation being deflected the least. As a result, the use of a helium-neon laser (6328 Å) for resonator alignment requires that this wavelength be made parallel to the optical axis of the resonator; i.e., the 1.06μ path. The (color) correcting prism provides that function.

2. The correcting prism used by the PD manufacturer had the following characteristics:

   a. The isosceles correcting prism is set so that the 6328 Å light strikes it at the angle of minimum deviation.

   b. The angular correction Δ required is 37'47" = 0.6297°.

   c. Assuming that borosilicate crown glass is of refractive index n, then the wedge angle α of the prism required is 1°12'17" and is given by

$$\alpha = 2 \tan^{-1} [(\sin \Delta/2)/n - \cos(\Delta/2)] \tag{1}$$

where the parameters as given above are substituted in Eq. 1 to provide α.

3. Consider now the right-angle correcting prism shown in Fig. A.3-1, drawn grossly out of proportion for convenience in the discussion to follow. The path marked "A" corresponds to the optical axis of the resonator (or the 1.06μ radiation path). The angle Δ is the difference in propagation direction from the calcite prism of the laser and the alignment wavelength. The requirement of the right-angle correcting prism then is to deviate the 6328 Å radiation from path B to path A' which is parallel to path A.

4. From the diagram in Fig. A.3-1, it follows that

$$\alpha = \beta \tag{a}$$

$$\beta' = \alpha + \Delta \tag{b}$$

$$n \sin \beta = \sin \beta' \quad \text{(Snell's law)} \tag{c}$$

$$n \sin \alpha = \sin (\alpha + \Delta) \tag{d}$$

Expanding the sine function in (d) yields

$$n \sin \alpha = \sin \alpha \cos \Delta + \sin \Delta \cos \alpha$$

or

$$n \tan \alpha = \tan \alpha \cos \Delta + \sin \Delta$$
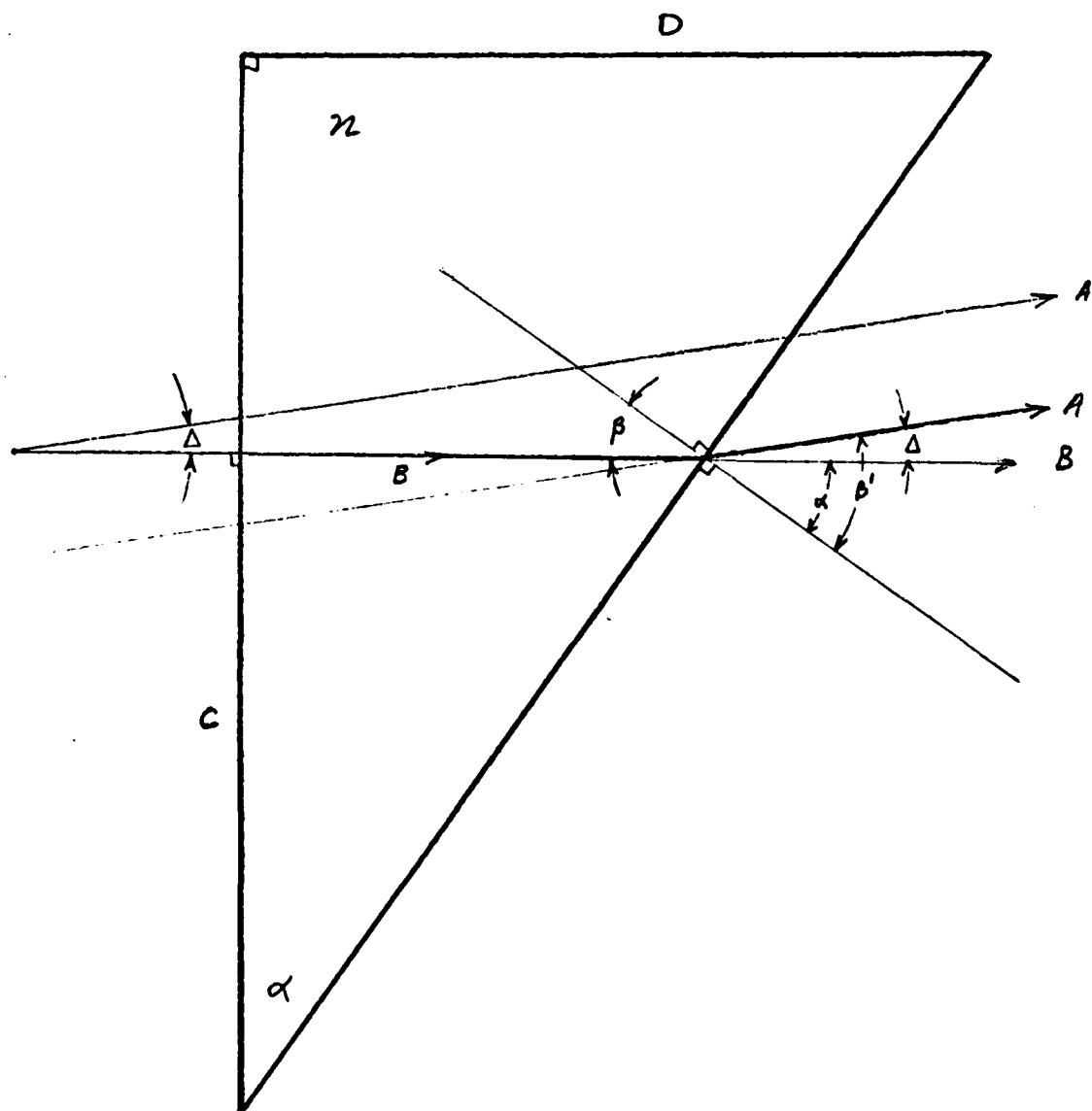
$$\tan \alpha = \sin \Delta / (n - \cos \Delta)$$

FIG. A.3-1. Right-Angle Correcting Prism.

The right-angle correcting prism wedge angle is given by

$$\alpha = \tan^{-1} \left[\sin \Delta / (n - \cos \Delta) \right] \tag{2}$$

By substituting the values of $\Delta = 0.6297°$ and $n = 1.52266$, it follows that $\alpha = 1°10'$, approximately. Comparing this value to that in Eq. 1, the correcting prism wedge angles are nearly equal. In the limit of very small α, it is seen that Eq. 1 and 2 correspond.

5. The isosceles prism used by the PD manufacturer requires the polishing of two surfaces of equal inclination to the base assuming a glass blank is used. The right-angle correcting prism needs polishing only at one surface with an inclination established from two flat surfaces C and D. The fabrication cost of the right-angle correcting prism is less than 50% of the cost for the isosceles color-correcting prism. The estimated cost of eight right-angle correcting prisms is less than $400 as provided by the Optics Technology Branch. (These prisms have been delivered to the Laser Designator/Rangefinder Branch.)

6. The right-angle correcting prism has the alignment beam at normal incidence. Therefore, the reflected beam is collinear to the incident beam and its alignment is easily achieved. The isosceles prism requires light incident at the minimum angle of deviation; i.e., a skewed reflection.

7. The use of right-angle correcting prisms is thus recommended for laser alignment and similar applications because of reduced cost of fabrication and convenience in alignment.

NOTES:

1. For alignment of the resonator, the correcting prism is placed between the calcite prism and the dump mirrors. The correcting prism is also used when tracing the path of the output beam; for example, to an aperture of a beam expander.

2. The right-angle correcting prisms are being used exclusively for He-Ne alignment of the T-beam resonator.

Appendix A-4

TWO-REFLECTIVE SURFACE, TWO-COLOR MIRROR

1. Figure A.4-1 shows the PD resonator layout. The fold mirror provides the capability of obtaining an effective resonator optical path length of more than twice its physical length. The fold mirror must have adequate reflectivity at He-Ne wavelength to provide ease in resonator alignment as well as high reflectivity at the laser wavelength. Hence, the terminology of "two-color" mirror is used since it must be highly reflective at the two wavelengths.

1. 100% END MIRROR	5. TWO-COLOR FOLD MIRROR
2. LITHIUM NIOBATE MODULATOR	6. Nd:YAG LASER POD
3. ALIGNMENT WEDGES	7. QUARTER-WAVE PLATE
4. CALCITE PRISM POLARIZER	8. 100% END MIRROR
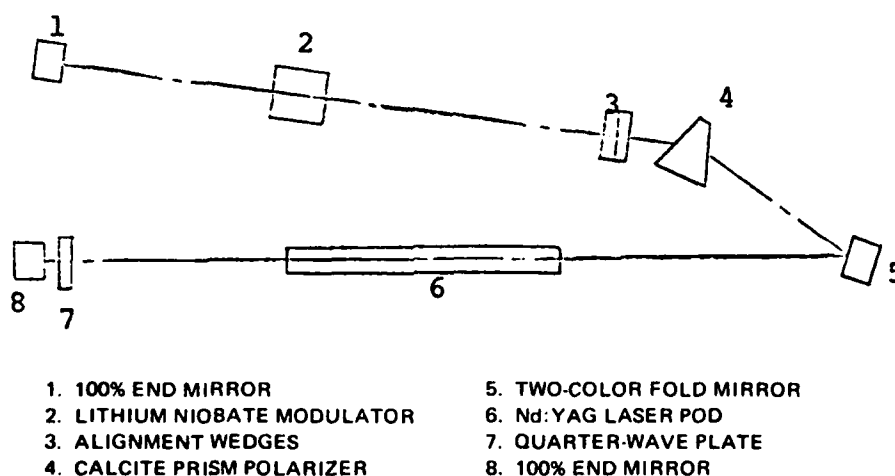
FIG. A.4-1. PD Resonator Layout.

2. The use of a two-color mirror causes the 1.06μ wavelength to be less reflective than if a single wavelength coating were used. Though this reduced reflectivity represents an insertion loss (few tenths of one percent) to the resonator, this is not the major shortcoming of a two-color mirror. Mirror vendors will not allow user specifications on these mirrors requiring a power density capability in excess of 50 MW/cm^2. The possibility of physical damage to the fold mirror is evident.

3. Figure A.4-2 shows a proposed two-reflective surface, two-color mirror. The 1.06μ wavelength is made highly reflective on the front (left) surface; the 6328 Å alignment wavelength is made highly reflective on the back (right) surface. This concept provides a higher reflectivity and a higher power density capability at the crucial front surface. The 6328 Å coating need not be of high quality as compared to the two-color mirror approach.

4. Ray path A, A' is a typical incoming beam direction. Ray A corresponds to the reflected laser radiation path; ray A' to the 6328 Å He-Ne wavelength path. The wedge angle α is the mirror surface deviation from true parallelism. For ray A, $\beta = \eta$. Due to angle α, $\beta \neq \eta$ for ray A'. It is required then to calculate an allowable α to ensure lasing will occur when the resonator is aligned using this proposed fold mirror design. From Fig. A.4-2 it follows that

$$\sin \beta = \eta \text{ sub } \beta' \qquad \text{(Snell's law)} \qquad \text{(a)}$$

$$\beta' + \alpha = \gamma' \qquad \text{(b)}$$

$$\gamma = \gamma' \qquad \text{(c)}$$

$$\gamma' + \alpha = \eta' \qquad \text{(d)}$$

$$n \sin \eta' = \sin \eta' \qquad \text{(e)}$$

By substitution,

$$\sin \beta = n \sin (\gamma' - \alpha) \qquad \text{(f)}$$

$$\sin \beta = n \sin (\eta' - \alpha - \alpha) = n \sin (\eta' - 2\alpha) \qquad \text{(g)}$$

$$\sin \beta = n[\sin \eta' \cos 2\alpha - \cos \eta' \sin 2\alpha] \qquad \text{(h)}$$

$$\sin \beta = \sin \eta \cos 2\alpha - n \sin 2\alpha \cos \eta' \qquad \text{(i)}$$

then finally

$$\sin \beta = \sin \eta \cos 2\alpha - [n^2 - \sin^2\eta]^{1/2} \sin 2\alpha \qquad \text{(1)}$$

which describes the reflected ray angle of A' from the mirror normal with respect to the known input angle β, the wedge angle α, and the refractive index of the proposed mirror design.

5. Equation 1 can be simplified by using the small angle approximation. This yields

$$2\alpha = (\sin \eta - \sin \beta) (n^2 - \sin^2\eta)^{-1/2}$$

$$2\alpha = \Delta \cos \beta/(n^2 - \sin^2\eta)^{1/2} \qquad \text{(2)}$$

where it was assumed that η differs from β by a small angle Δ. The angle Δ then represents the 6328 Å beam misalignment upon reflection. The end mirrors of the resonator must be aligned to its optical axis within about 100 arc-seconds to ensure that laser action occurs prior to active operation. So it requires that Δ is less than 100 arc-seconds, substituting the parameters in Eq. 2,
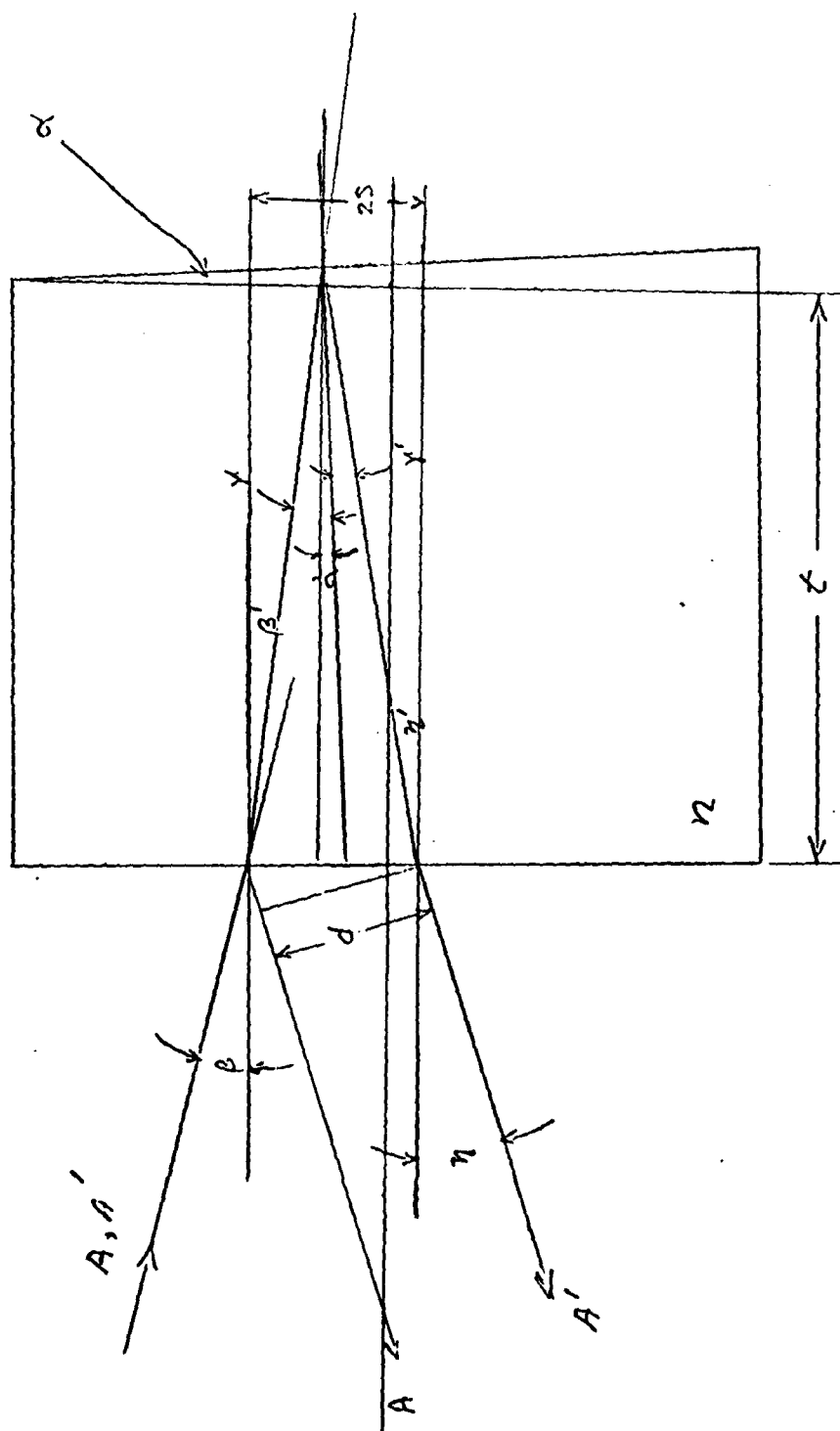
FIG. A.4-2. Mirror Geometry.

$2\alpha < 100 \ (0.951)/1.5$

$\alpha < 31$ arcsec

as the required accuracy of the parallelism of the mirror surface to make this concept practicable.

6. One other calculation is needed. In Fig. A.4-2, dimension d is the shift in the alignment beam axis with respect to the optical axis of the resonator after two passes through a mirror of thickness t. So now assume that $\alpha = 0$; i.e., $\beta = \eta$. From the mirror geometry, one sees that

$2S \cos \beta = d$ (a)

$2t \tan \beta' = S$ (b)

$\sin \beta = n \sin \beta'$ (c)

which yields

$$d = 4t \cos \beta \sin \beta / (n^2 - \sin^2 \beta)^{1/2} \tag{3}$$

For the PD resonator, $t = 0.50$ inch, $\beta = 18°$, $n = 1.523$. So by substituting, it follows that

$d = 0.392$ inch $= 10$ mm

But this is larger than the diameter of the laser rod! The beam displacement decreases directly as t decreases. An allowable displacement of 2 mm causes the mirror thickness to be 0.100 inch which is difficult to accept. (Thin mirrors are more subject to thermal distortion and deformation due to to mechanical stresses of the mirror mount.) Note too that the deflections in angle and distance apply only for a single pass and two passes are required for alignment.

7. So what seemed to be a feasible solution to the two-color mirror problem is destroyed by other physical requirements of the fold mirror itself.

NOTES:

1. The surface damage problem remains when the two-color fold mirror (with increased reflectivity at He-Ne wavelength) is used. This complicates the alignment of the resonator if it cannot be safely used.

2. The high reflectivity at 6328 Å is more important for aligning the modulator than it is for aligning the resonator end reflectors.

A misaligned lithium niobate modulator behaves as if a DC field were present at the cell and so complicates the requirements for optimum Q-switching. The "Maltese Cross" is used for modulator alignment rather than using surface reflection.

3. The T-beam resonator uses a 5-mm mirror thickness.

4. Beam uniformity measurements have shown that the *maximum* peak-power density in the resonator may be four times larger than the *average* peak-power density. All in-house lasers have an *average* peak-power density in excess of 50 MW/cm^2.

Appendix A-5

END REFLECTOR MISALIGNMENT SENSITIVITY

1. The end-mirror misalignment sensitivity was measured for the following mirror combinations: (1) two flats, (2) one flat plus one 10-meter (radius of curvature) end mirror, and (3) two 10-meter end mirrors. A T-beam resonator layout (less the fold mirror) was used for these tests. The mirror misalignment sensitivity to reduce the energy output by 10%-- using (1) two flats, (2) one flat plus one 10-meter mirror, and (3) two 10-meter mirrors--was 12, 15, and 21 arc-seconds, respectively (Fig. A.5-1 through A.5-3).

2. The requirement for maintaining resonator alignment over a wide temperature range of (say) -30^{ν}C to $+40°$C makes extreme demands of its stability, regardless of the end mirror curvature used. To alleviate this problem in a thermally unstable resonator, a roof-prism end reflector is often used and is placed so that its roof edge is perpendicular to the resonator distortion axis or plane. The roof-prism end reflector is less useful in resonators which use polarized radiation since, in this case, the roof edge needs to be either parallel or perpendicular to the resonator plane of polarization to keep its insertion loss low. If the resonator plane of polarization is neither parallel nor perpendicular to the roof edge, the roof-prism end reflector behaves similarly to a quarter-wave plate and end-mirror combination, in that the effective reflectivity of the resonator can be modified by rotating the roof prism about the resonator axis. Hence (in the T-beam for example), the roof edge needs to be aligned either parallel or perpendicular to the flashlamp-rod plane and must be perpendicular to the distortion plane of the resonator as well.

3. The test apparatus consisted of a 70% reflectivity, a flat-end dump mirror, the pump cavity, a calcite prism polarizer, and the second end reflector (either a mirror or a roof-prism end reflector). The roof prism used in these tests was obtained from a now defunct laser and had several burn spots near the roof edge. The insertion loss of this particular roof prism is not felt representative of such components available on the market today. The PD contractors found an output degradation of typically 15% in their related tests with roof-prism end reflectors. A 10-meter end mirror was tested first in the resonator for comparison purposes, and the misalignment sensitivity was done only in azimuth due to its misalignment symmetry. To get accurately calibrated end-reflector misalignment readings, a Lansing mirror mount was used on the test component. When the roof-prism end reflector was substituted for the 100% end mirror and then rotated about the roof-edge axis, no appreciable degradation in output energy occurred (as expected) over the adjustment

range of the Lansing mount; namely, about ±350 arc-seconds. A rotation about an axis perpendicular to the roof edge yields the misalignment sensitivity shown in Fig. A.5-4.

4. As stated earlier, the roof edge must be accurately aligned relative to the distortion axis of the resonator to make the component adaptable. Some compensation for effective reflectivity may be made with the quarter-wave plate if the distortion axis or its normal is only slightly different from the flashlamp-rod plane. Compared with a simple end mirror, generally the roof-prism end reflector (1) requires a more complex mounting structure, (2) increases the raw-beam divergence and beam non-uniformity, and (3) has a higher insertion loss. Thus its use should be limited to those cases where its unique misalignment sensitivity is required.
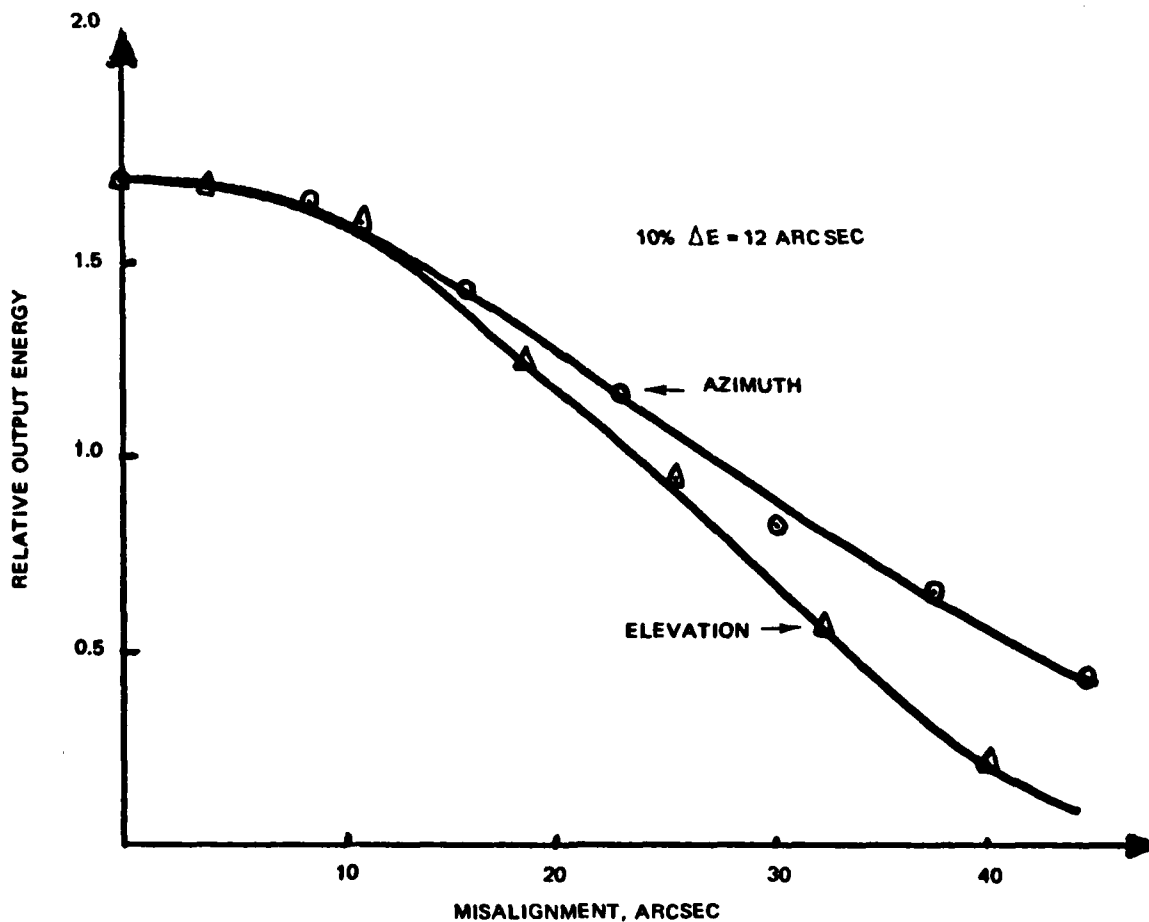
FIG. A.5-1. Mirror Misalignment Sensitivity; Two Flat End Mirrors.
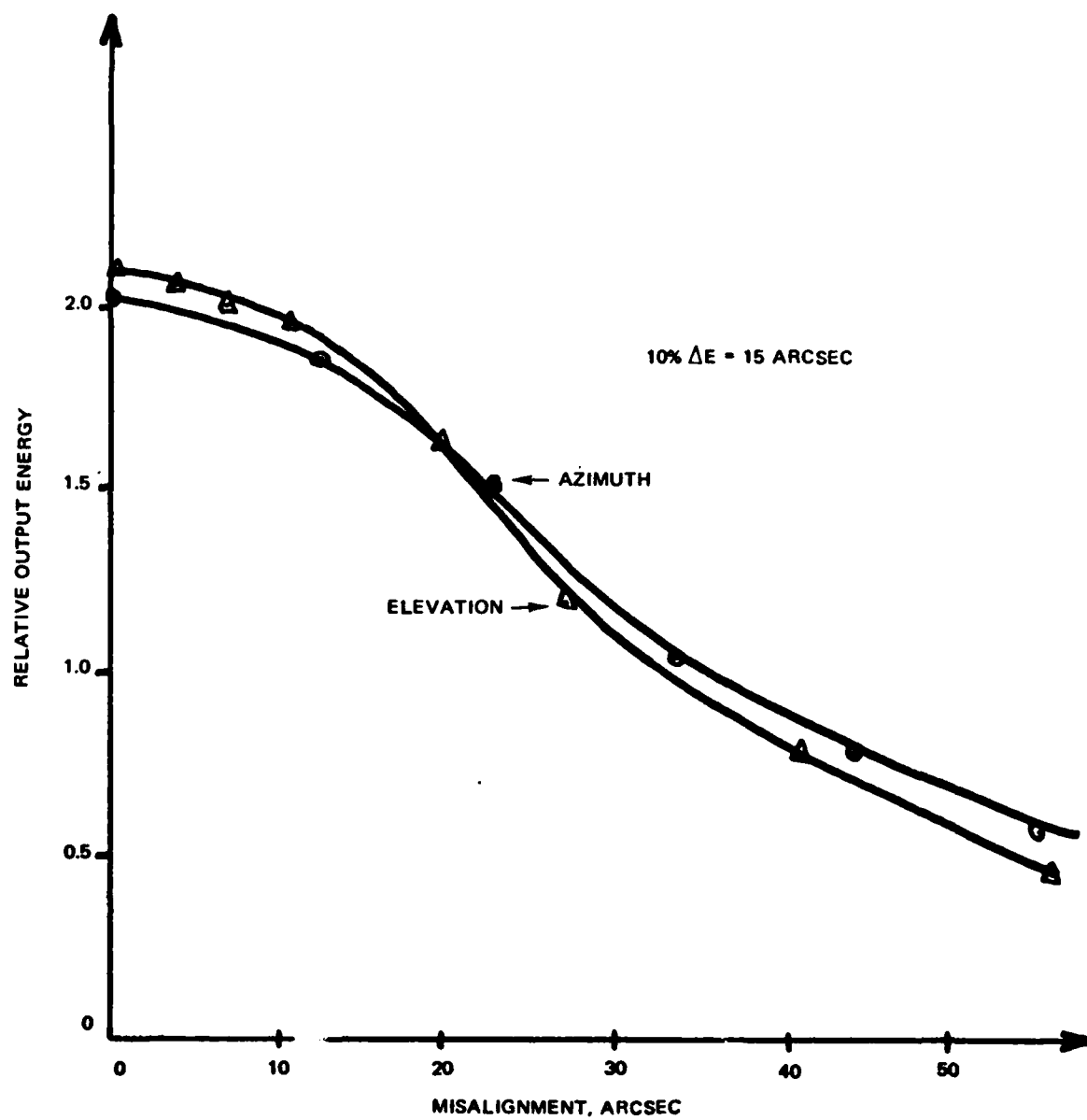
FIG. A.5-2. Mirror Misalignment Sensitivity; One Flat,
One 10-Meter End Mirror.
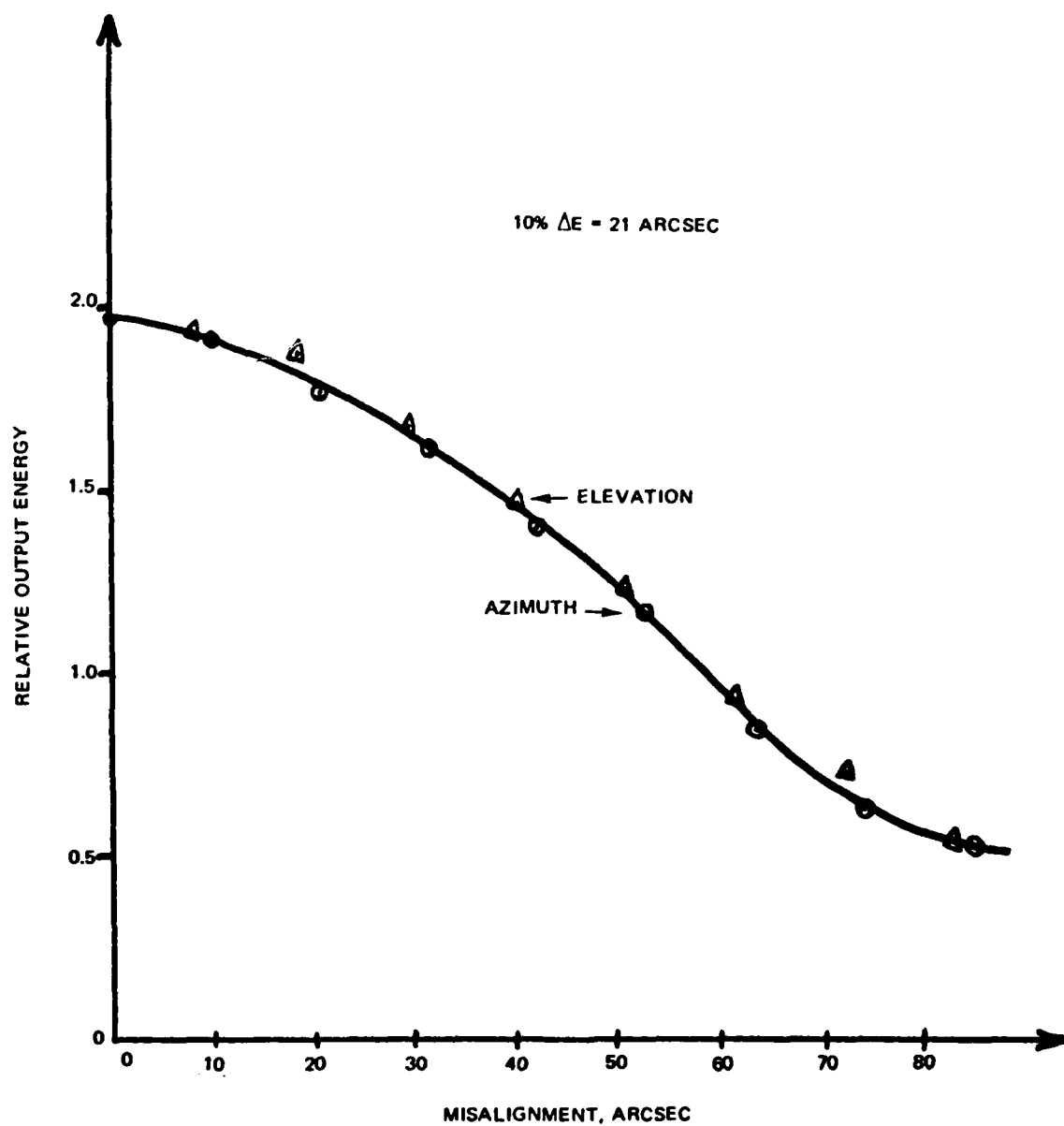
FIG. A.5-3. Mirror Misalignment Sensitivity; Two 10-Meter End Mirrors.
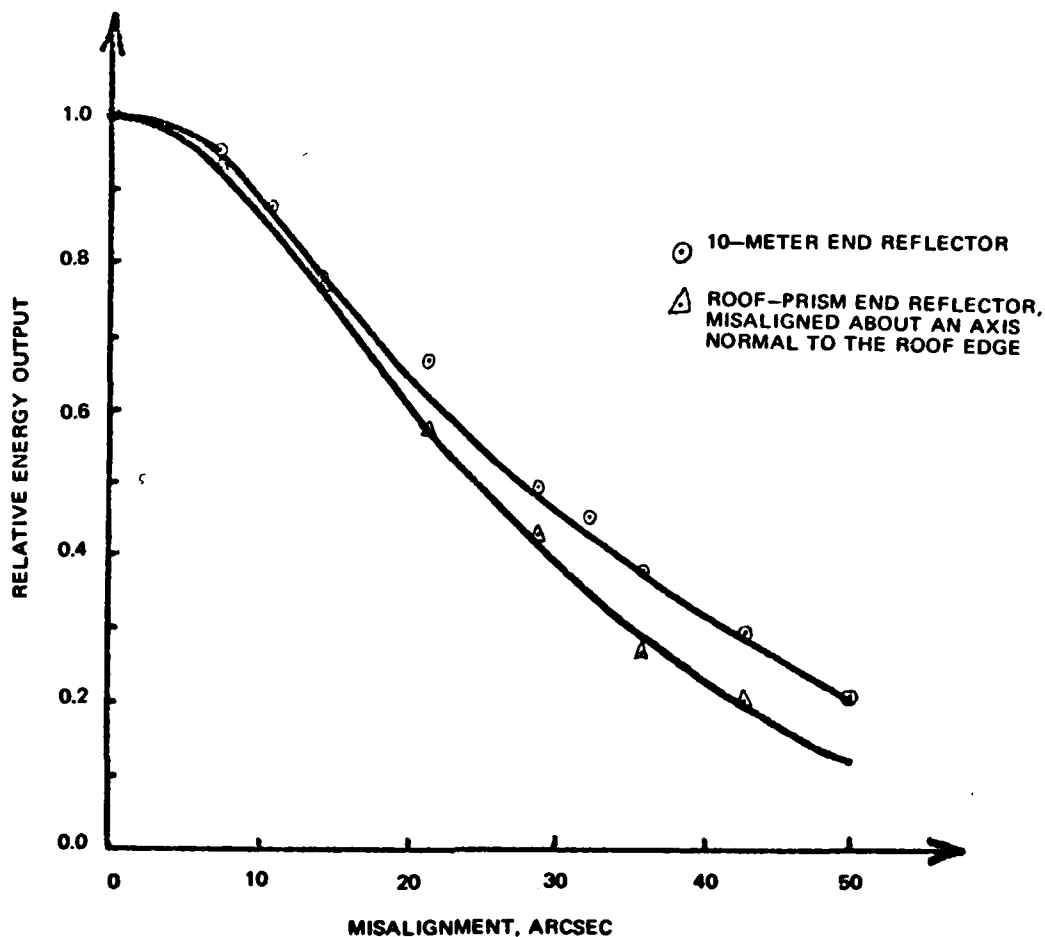
FIG. A.5-4. End Reflector Misalignment Sensitivity Data.

NOTES:

1. The fold mirror used in the T-beam increases the mirror misalignment sensitivity by a factor of two and is an undesirable feature.

2. The non-Q-switched beam uniformity using various end reflectors is shown in Appendix F-1.

3. The thermal stability of the T-beam has been very good; thus, the roof-prism end reflector has not been necessary.

4. The ability of the Lansing mount to misalign the resonator accurately and reproducibly within arc-seconds was tested with a Davidson two-axis autocollimator.

5. The difference in azimuth and elevation misalignment sensitivity is indicative of the Lansing mirror mount misalignment accuracy.

6. All laser resonators built in-house and in operating equipment are using one flat plus one 10-meter radius of curvature end mirror.

7. Laser manufacturer data are available showing that a short in-line resonator using one flat plus one 4-meter mirror has a 19-arcsec mirror misalignment tolerance (to reduce output energy by 10%).

Appendix A-6

INSERTION-LOSS MEASUREMENTS AND THE LOSS BUDGET

1. To establish the laser output reduction due to resonator component surface reflection and internal absorption and, in some cases, bire-fringence, tests were conducted on insertion loss. These tests involved inserting a known transmission element into the oscillator and noting the degradation in the laser output energy. The experimental results are expressed in terms of percent output energy degradation per 1% inserted loss. Three elements were used and their transmission data are given in Table A.6-1. The average value of test transmission measurements was used to plot the data in Fig. A.6-1. In terms of output energy, an insertion loss of 1% degrades the laser output by 4%. Two resonator elements were tested for insertion loss; namely, a quarter-wave plate and a damaged lithium niobate modulator used in the past bread-board resonator tests. They were found to degrade the output energy by 10% and 12%, respectively, implying a value of transmission of 97.5% and 97.0%, respectively.

TABLE A.6-1. Test Element Insertion-Loss Data.

Test element	Test 1 (Dr. Hills)	Test 2 (Dr. Olson)	Test 3 (Teppo)	Average transmission
Micro slide	90.5	90.0	89.8	90.1
Glass plate	88.0	87.0	88.1	87.7
End mirror	1.8*	---	---	1.8

* Valpey's value for reflectance was measured as 98.2%.

2. Since it has been established that an insertion loss of 1% reduces the laser output energy by 4%, a means is now available for estimating what the total energy output loss should be due to inserting all the resonator components (except the end mirrors and the laser rod itself). With this in mind, Table A.6-2 shows the output degradation anticipated by their use on the basis of the portable designator (PD) manufacturer's part specification figures. These part specification figures were estab-lished in discussion by the PD manufacturers with resonator component sources and represented, they felt, the state-of-the-art values. In practice, however, it readily becomes apparent that the insertion loss, for example, for a lithium niobate modulator is considerably more than 1.5%.
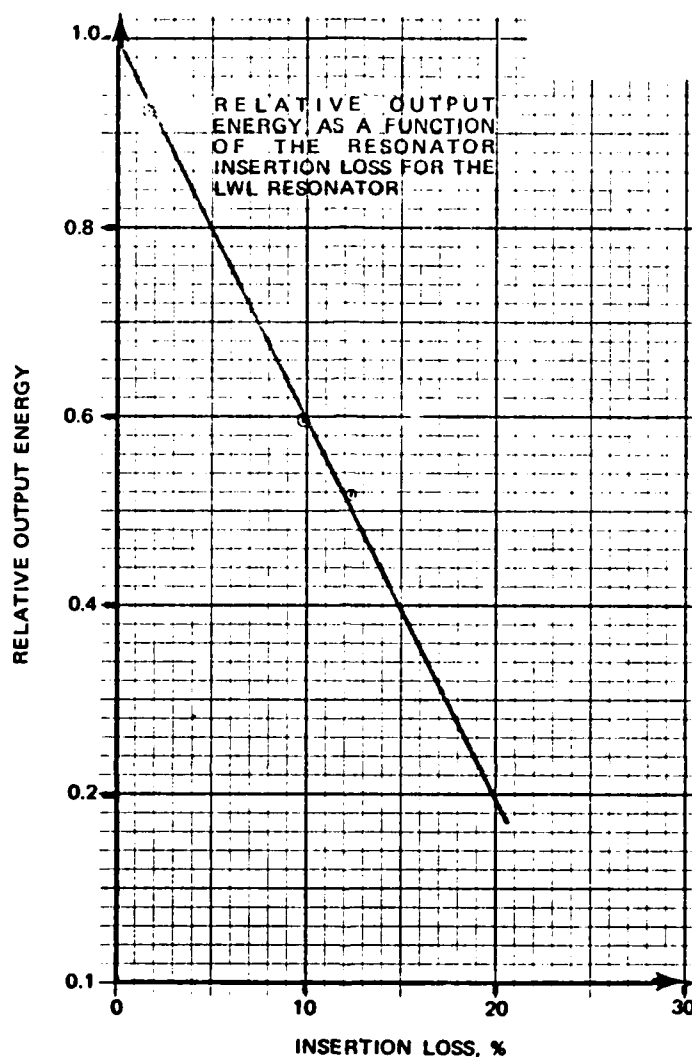
FIG. A.6-1. Insertion Loss Data Plot.

3. On the basis of these measurements, it became apparent that insertion-loss measurements on resonator components were urgently needed. As a result, a test apparatus was assembled to perform the data tests.

4. The resonator loss budget is the compilation of all the optical losses in the resonator. These optical losses may be due to surface reflectance, scattering, absorption, birefringence, or any other losses solely dependent on the passive properties of optical components. Paragraph 1 of Appendix A.6 shows that a resonator insertion loss of 1% reduces the output energy by approximately 4%. Paragraph 2 shows that, on the basis of

TABLE A.6-2. Resonator Component Loss Factors.

Resonator component	Loss mechanism	Loss value, %	Relative energy output
Alignment wedges	Surface reflection	0.60	1.00 0.986
Modulator:	Surface reflection Absorption Birefringence	0.30 0.50 3.0*	0.974 0.954 0.924
Fold mirror	Surface reflection	0.20	0.912
Calcite prism:	Anomalous birefringence Surface reflection	0.10 0.30	0.908 0.894
Quarter-wave plate	Surface reflection	0.40	0.882

Total output degradation....11.8%

* Represents an output loss only and is not an insertion loss per se.

the present optical part specifications, the total output energy degradation due to insertion of all resonator components should be less than 12%; whereas, in actual practice, the loss is nearly three times larger than this figure. Resonator optical components grossly out of specifications have been received in the past, and continued controls must be placed on their optical quality in the future. Three examples are given of attempted sale of poor quality laser resonator components.

a. A laser rod was received having an apparently severe optical distortion (as evident by Twyman-Green interferometer photograph) far worse than the part specification allowed. When the vendor was informed that the delivered part was being rejected, the vendor stated that the part could be kept by us and that he would supply another laser rod at no cost to us.

b. Two Pockel cells were received which measured essentially unity extinction ratio; i.e., its transmission did not change significantly when voltage was applied. Examination under crossed polarizers revealed that the Maltese Cross pattern would not form. These modulators were rejected and the vendor later agreed that the modulators were not salable.

c. A laser rod ordered as Lu:Nd:YAG was delivered by a laser rod vendor. Its interprogram showed that it was not within fringe count specification and so was not used. A substitute was supplied at no cost. Later spectroscopic analysis showed the laser rod to be Nd:YAG, not Lu:Nd:YAG.

These optical components were of poor optical quality in very evident ways. The fact that the vendors would attempt to deliver components with such obvious deficiencies suggests strongly that other optical components already accepted and in use may be far from meeting our specifications as well. For example: tests by the author indicated that the quarter-wave plate in the lightweight laser (LWL) degrades the output energy by over 10% alone! (The surface reflectance was measured for two quarter-wave plates in the same lot as the one presently in the LWL, and they were found to be 1.3% and 1.5% per surface reflecting at the laser wavelength.) Hence, it is important that the resonator loss budget be established and the optical losses per component be identified.

5. The laser rod end-face reflectance was measured using the test apparatus (Fig. A.6-2). An He-Ne alignment laser was used to allow visual observation of the CW Nd:YAG beam path. The Edgerton, Germeshausen, and Grier, Inc. (EG&G) IR High-Sensitivity Head input radiation was chopped, apertured, and filtered, and the signal was amplified at 200 Hz with readout on the PAR Model HR-8 Lock-In Amplifier. A low-reflectivity standard of fused silica (one surface ground optically flat, the other fine ground and spray painted black) was used for comparison to the laser rod end-face reflectance. The angle of incidence for all measurements was near 5 degrees. A roof prism (not shown) was used to deflect the transmitted radiation out of the detector field of view.

6. Table A.6-3 summarizes the laser rod end-face reflectivity measurements. The end-face reflectance varies by more than a factor of five with an average reflectance of 0.19% per surface for all rods tested. The part specification for end-face reflectance is usually 0.25% per surface maximum. Since Union Carbide now coats their own laser rods and Airtron now owns Lambda Optics, the laser rod end-face reflectance is established by the choice of laser rod vendor selected.

TABLE A.6-3. Laser Rod Reflectivity
Data Summary.

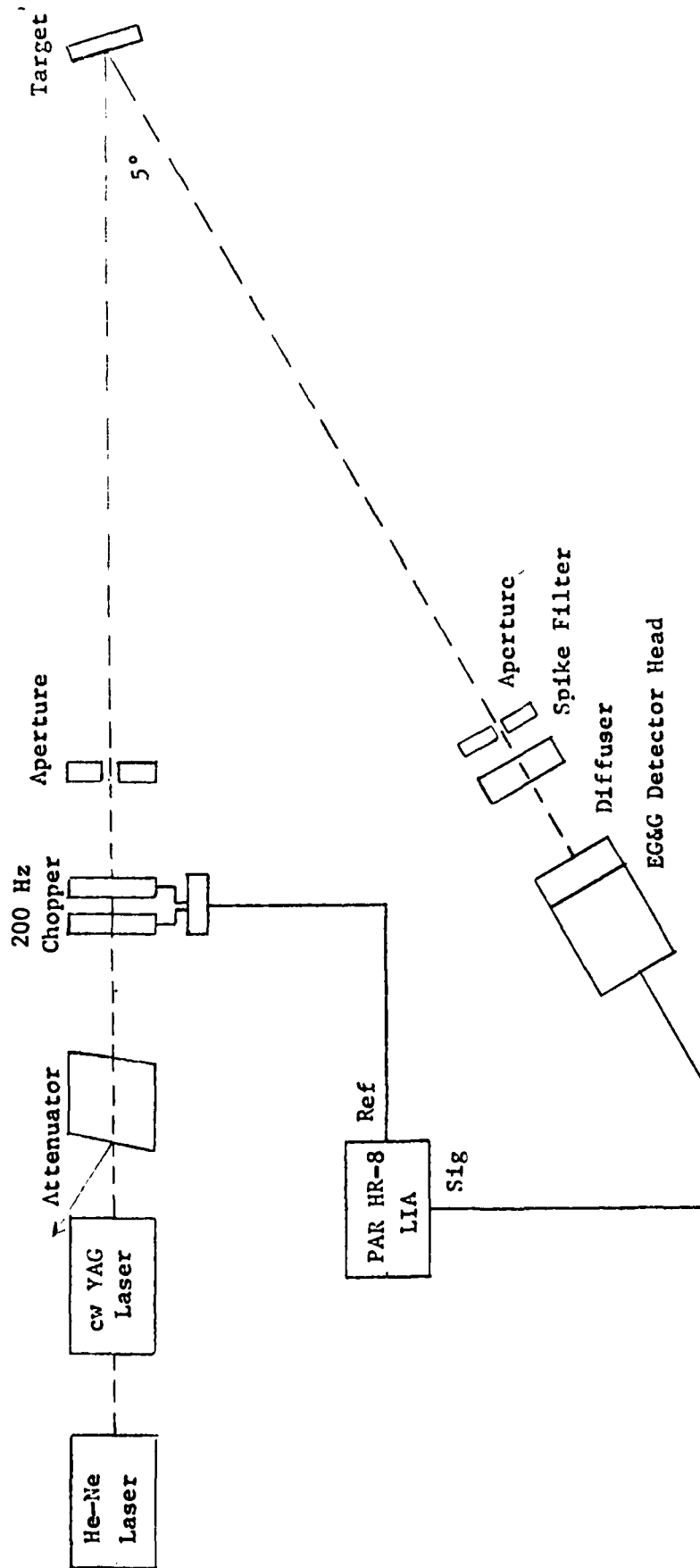| Part identification	R_1,%	R_2,%
Airtron #1910	0.21	0.30
TRW* #1317	0.06	0.07
Airtron #1266	0.38	0.23
Airtron #1225	0.28	0.29
TRW #1424	0.07	0.09
TRW #1338	0.07	0.19
TRW #1318	0.20	0.07
TRW #1071	0.20	0.08
Union Carbide wood box .	0.30	0.25
Airtron #1782	0.12	0.17
Union Carbide 5 mm	0.28	0.28

* Thompson, Ramo, Wooldridge, Inc.

FIG. A.6-2. Test Apparatus.

7.   Reflectivity measurements made on Pockel cell modulators, wave plates, and alignment wedges are described. Due to the thickness of these components, both end-face reflectances are measured simultaneously, and hence, the total surface reflectance is recorded. The two-pass absorption of (even) lithium niobate has a negligible effect on the surface reflectance measurements. The resonator components were placed in an XY mount to allow accurate positioning of the reflected radiation to the detector aperture. The low-reflectivity fused-silica glass plate provided the standard reflectance of 3.37%.

8.   Table A.6-4 summarizes the Pockel cell modulator reflectivity data taken. The reflectance R is the total surface reflectance. For purposes of comparison, two damaged modulators were also tested. The reflectivity measurements rely on specular surface reflectance, and loss due to scattering at the surface (as expected from damage sites) is not recorded. Excluding the damaged modulators reflectance values, the average reflectance per surface is 0.5%; whereas, the part specification value is 0.2% per surface. The 25-mm long modulator planned for use in the portable airborne designator, stabilized (PADS) unit (though not listed) had an average reflectance per surface of 0.16%.

TABLE A.6-4.   Modulator Reflectance
Data Summary.

Part identification	Reflectance R, %
Crystalab C-3	0.62
Crystalab C-4	0.66
Harshaw LN 357-2	0.60
Union Carbide L3N91C2	2.25
Union Carbide L3N98C2	0.36
Union Carbide L3N94C2	2.20
Crystalab C-1	0.68
Harshaw 376-2 (damaged) ...	0.97
Isomet 5121-2 (damaged) ...	0.24

9.   Table A.6-5 summarizes the wave-plate reflectivity data taken. The wave plates intended for use in the PD unit are included among those listed. The 10-mm diameter quarter-wave plates measured were from the same lot as the quarter-wave plate presently in use in the LWL unit and intended for the PADS unit if end dump is not used. Use of this quarter-wave plate degrades the output energy by 10-12%. The average reflectance per surface is 1.54%; whereas, the part specification now in use requires an average surface reflectance of not more than 0.2%. Use of an end dump

configuration would remove the quarter-wave plate from the resonator, and since it appears that the vendors are unable to approach the part specification for surface reflectance loss, further consideration should be given to the end dump approach. The end dump approach also reduces the likelihood of modulator surface damage due to erroneous reflectivity setting with the quarter-wave plate.

TABLE A.6-5. Wave-Plate Reflectance Data Summary.

Part identification	Reflectance R, %
Breadboard λ/4	1.12
λ/2 Plate #1	1.70
λ/2 Plate #2	0.83
λ/4 Plate #1	4.75
λ/4 Plate #2	5.95
10-mm λ/4 Plate #1	3.06
10-mm λ/4 Plate #2	2.56
Special Optics λ/4 1060C-1	3.26
Special Optics λ/4 1060C-2	1.94
Special Optics λ/4 1060C-3	5.68

10. Table A.6-6 summarizes the alignment-wedge reflectivity data. The 10-mm diameter alignment wedges were supplied by Del Optics and are appreciably lower in insertion loss than those the PD used. The average reflectance per surface for all alignment wedges measured is 0.53%; whereas, the 10-mm alignment wedges have an average surface reflectance considerably lower than this figure. The part specification figure is 0.2% reflectance per surface. It should be remembered that the resonator used two alignment wedges.

TABLE A.6-6. Alignment Wedge Reflectance Data Summary.

Part identification	Reflectance R, %
TRW Wedge #1	1.49
TRW Wedge #2	1.43
TRW Wedge #3	1.42
TRW Wedge #4	1.44
TRW Brass Mounted Wedge #1.	1.33
TRW Brass Mounted Wedge #2.	1.39
10-mm Wedge #1	0.15
10-mm Wedge #2	0.16
10-mm Wedge #3	0.71
10-mm Wedge #4	0.93

11. The resonator loss budget already shows that thus far only the laser rod average reflectance meets the part specification for surface reflectance. It is obvious from the tables that the vendor feels bound to deliver to part specifications in only an approximate way. Only two alignment wedges and most of the laser rods have complied with the surface reflectance specification. It also suggests perhaps that the surface reflectance specification is overly stringent and a part cost reduction may be possible if that specification is relaxed to more nearly the average experimental reflectance figure.

NOTES:

1. The terminology "LWL" refers to an in-house designed and built lightweight laser.

2. The terminology "PADS" refers to an in-house designed and built portable airborne designator, stabilized.

3. "End dump" refers to a resonator configuration using a partially transmitting end mirror as the output aperture.

4. The greatest improvement in resonator component quality has been in quarter-wave plate supplied by Del Optics. The insertion loss of their most recently supplied wave plate has been essentially negligible as compared to the values anticipated by the data of Table A.6-5. Del Optics showed an unusual willingness to solve the insertion loss problem, and they did.

5. Only a single calcite prism was tested and showed a surface reflectance of less than 0.5% per surface.

6. Birefringence loss measurements have not been performed.

7. The test apparatus shown in Fig. A.6-2 is being used to perform most of the incoming inspection of laser resonator components.

8. The quality of as-received laser resonator components has increased significantly in the past year.

9. The continuous wave (CW) YAG laser is made by Korad, and the 200-Hz chopper is made by Bulova.

10. The resonator components with "TRW wedges" designations (Table A.6-6) were delivered to the Navy at the termination of the PD contract, and the part manufacturer is not known.

Appendix A-7

LASER ROD COMPARISON

1. A non-Q-switched, end-dump laser resonator was used to measure the raw-beam divergence for three different Nd:YAG laser rods as a function of pulse repetition rate. The coolant used was FC-104 with a flow rate near 16 gal/hr, and the pump energy was 8 J/pulse. The laser resonator consisted only of a 50% reflectivity flat end mirror, a silvered cylindrical pump cavity, and a 10-meter radius of curvature high-reflectivity end mirror. A 40.6-inch focal-length lens was used to focus the output laser radiation on apertures of various size in the lens focal plane. The beam divergence value was based upon 85% energy content.

2. Figure A.7-1 shows the raw-beam divergence dependence on repetition rate for the three laser rods tested. The laser rods #1 and #2 have an average raw-beam divergence difference (at any particular pulse repetition rate) of almost one milliradian or about 25%. Incoming inspection of laser rods should therefore include a raw-beam divergence measurement in a *standard* laser resonator adequate for laser rod comparison. The data plotted show an average slope of approximately 0.075 mrad/Hz, which means that increasing the pulse repetition rate by 9 pps results in a raw-beam divergence increase of approximately 0.7 mrad. Hence a 20-Hz designator is expected to have a raw-beam divergence about 0.75 mrad larger than a 10-Hz designator using FC-104 coolant and the silvered cylindrical pump cavity design.

NOTES:

1. The tests discussed made the laser group aware of the wide variation possible in laser rod quality. The passive laser rod tests (distortion, fringe count, etc.) are not indicative of its performance while operating in a resonator.

2. The procurement of the highest quality laser rods available should be stressed. In systems requiring a laser beam expander, the small cost increase associated with improved raw-beam divergence figure is extremely practical as compared to the increased weight/cost of a larger beam expander and its design.

3. The increase in raw-beam divergence with pulse repetition rate is due to a radial thermal gradient as described in Appendixes C-5 and E-4.

4. Prior laboratory tests have shown that the raw-beam divergence of a non-Q-switched and of a Q-switched resonator are essentially equivalent.

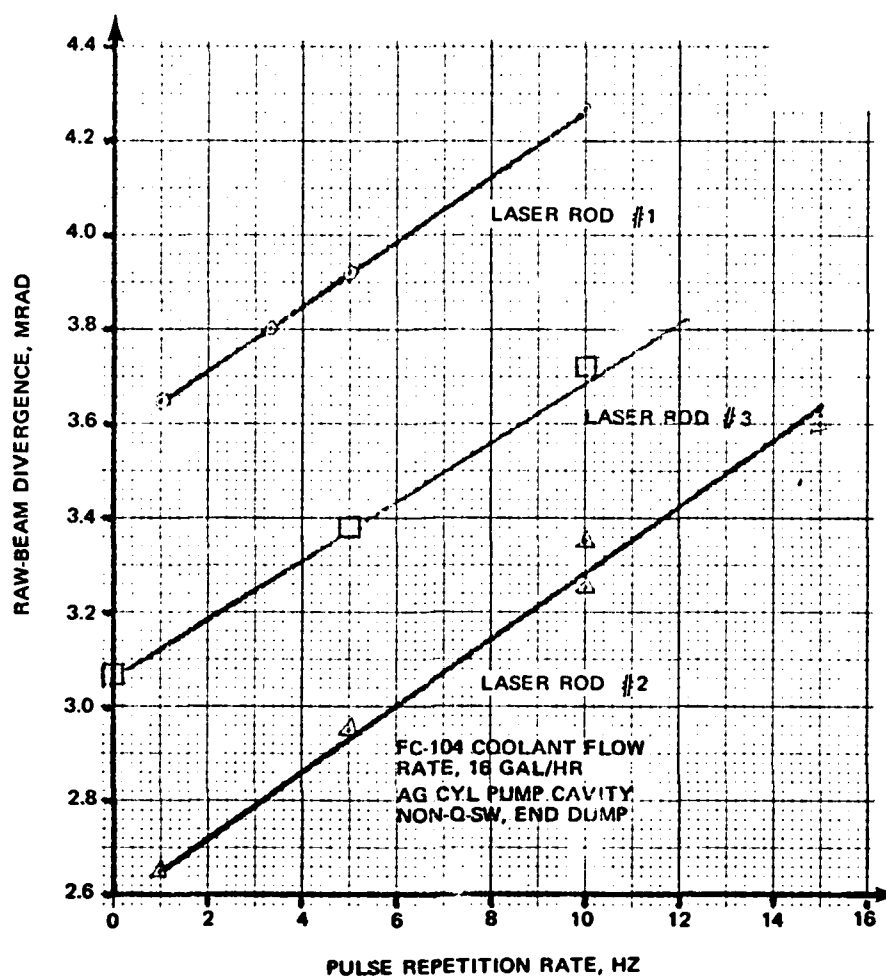5. The procurement of Lu:Nd:YAG laser rods is in progress.

38

FIG. A.7-1.   Raw-Beam Divergence Versus
Repetition Rate.

Appendix A-8

CONTACTLESS METHOD FOR LASER ROD
TEMPERATURE MEASUREMENT

1. In the use of a liquid-flow laser cooling system which has a limited duty cycle capability, the maximum operating time for a given ambient condition is established by the maximum allowable average coolant temperature or laser rod temperature. A pressurized gas flow laser cooling system (usually nitrogen gas) has a limited operating temperature established by a maximum allowable laser rod temperature of approximately 100°C. Normal test procedures for measuring laser rod temperature involve the use of thermocouples or thermistors which are indirectly coupled to the lateral surface of the laser rod. Such a test method usually requires that series triggering of the flashlamp be used. An interferometric technique to measure the laser rod temperature which requires no direct connection to the laser rod itself is described here. The interferometer is formed by reflections from the two end faces of the laser rod.

2. The interferometric test layout is shown in Fig. A.8-1. A beam expander is used to increase a single mode (TEM$_{oo}$) helium-neon laser output diameter to that of the laser rod under test. The laser rod axis is aligned parallel to the 6328Å (or probe source) beam. Some light is reflected from the front surface of the laser rod and some is internally reflected from the back surface as well which, when combined, form the interference fringes observed. The optical path length difference between the two reflections is given by

$$P = 2n \ell \tag{1}$$

where n is the refractive index of the laser rod (at the probe wavelength) and ℓ is the laser rod length. The phase difference between the two reflections is given by

$$\Phi = 2\pi P/\lambda = 4\pi n \ell/\lambda \tag{2}$$

If the two reflections have a phase difference which is a multiple of 2π, the back surface reflection will constructively interfere with the front surface reflection and a bright field exists at A. If the optical path length of the laser rod increases by $\lambda/2$ (or the product $n \cdot \ell$ changes by $\lambda/4$), a dark field (or perhaps a fringe which is dark) appears at A. As the laser rod heats due to flashlamp pumping, an alternately dark and bright field exists at A since both the laser rod length and its index of refraction increase linearly with temperature. The laser rod optical path length changes with temperature as
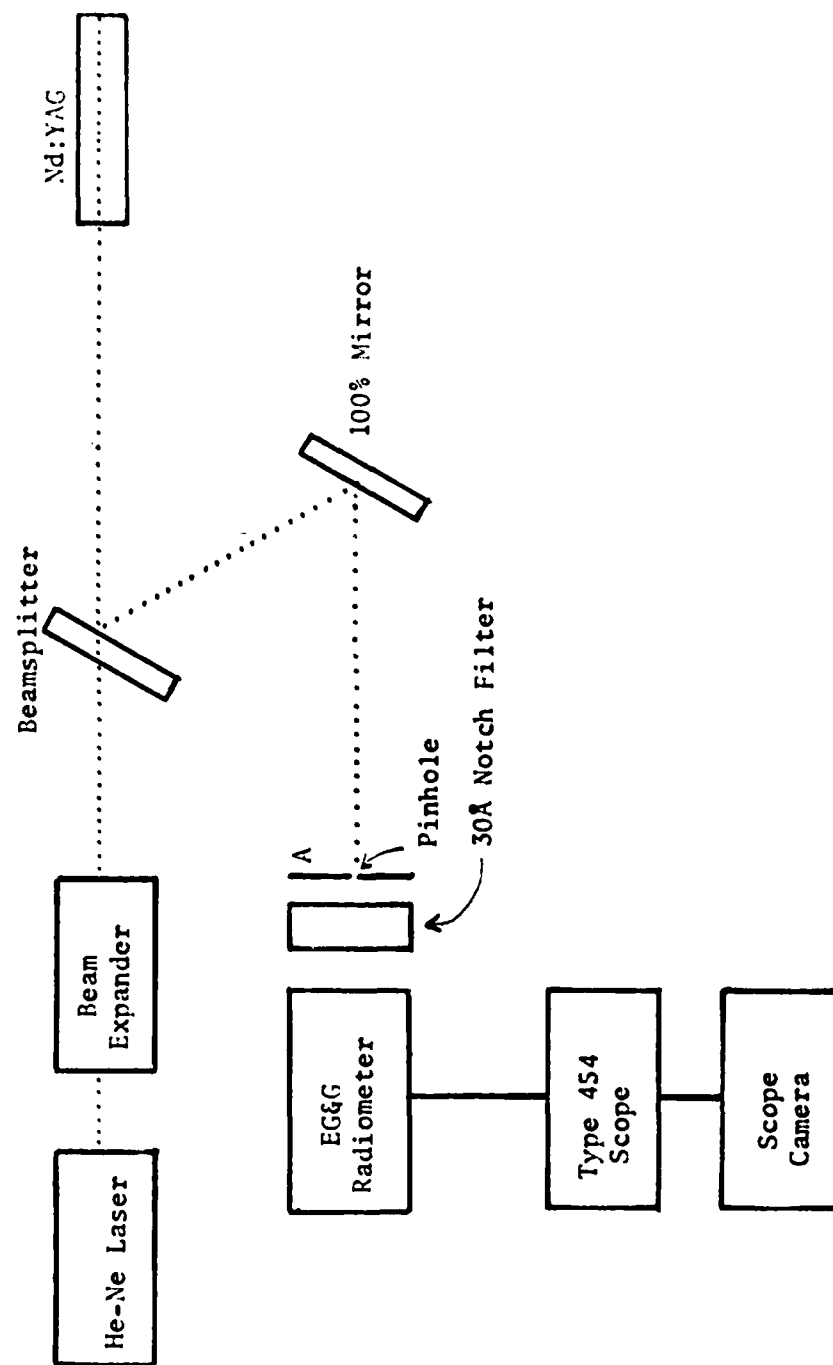
FIG. A.8-1. Interferometric Test Layout.

$$\Delta P/\Delta T = 2[n(d\ell/dT) + \ell(dn/dT)] \tag{3}$$

and so

$$\Delta P = \Delta T(\Delta P/\Delta T) = 2\ell[n\alpha + (dn/dT)]\Delta T \tag{4}$$

where

$n = 1.83$, the index of refraction of the laser rod

$\alpha = \ell^{-1} d\ell/dT = 6.9 \times 10^{-6}{}^\circ C^{-1}$, its linear expansion coefficient, and

$dn/dT = 7.3 \times 10^{-6}{}^\circ C^{-1}$, its thermal index coefficient.

In practice, since the laser rod has a slightly longer optical path length over its diameter, there is typically a wavelength of optical path length difference over its reflected interference pattern at A. Hence, a pin-hole, whose diameter is less than the dark fringe width, is used at A. The view at A then consists of dark fringes on a light background, the dark fringes being separated by one wavelength in optical path length. As the laser rod is heated (or cooled), the fringes move in only one direction (with some precautions on the experimenter's part) and so can be counted as they pass the pinhole at A. The total fringe count, N, using a radiometer detector as shown in Fig. A.8-1, is related to the increase in temperature of the laser rod due to flashlamp pumping since

$$2\ell[n\alpha + (dn/dT)]\Delta T = N\lambda \tag{5}$$

So then, by substituting in the actual values, it readily follows that

$$\Delta T = 0.207 \, N(^\circ C) \tag{6}$$

and the observed fringe count is directly related to the laser rod temperature change relative to its temperature under the ambient conditions.

3. The laser breadboard resonator was operated for several minutes at 8 J input energy and 10 pps. The laser rod had reached an equilibrium operating temperature condition since the fringe travel had stopped. The laser was then shut off. Simultaneously the scope trace and scope camera were started and almost all fringes were recorded (with some manipulation) as shown in Fig. A.8-2. (After about 15 seconds of cool-down time, the scope time base was changed to a 5-sec/div rate so that most of the fringes could be photographed.) Several more fringes were counted on the radiometer indicator unit, and it was found that the total fringe count, N, was 55. By substitution into Eq. 6, it is found that the average rod temperature had increased 11.4°C. This increase in the laser rod temperature is not representative of that for the

typical laser cooling system; e.g., the laser breadboard resonator cooling system is that of the PD unit which is capable of continuous operation at over 20 J input per pulse at 10 pps. If several minutes of cooldown time are expected in these fringe counting experiments, it is preferable that a strip chart recorder be used, since several hundred fringes may need to be counted to establish the equilibrium laser rod operating temperature.
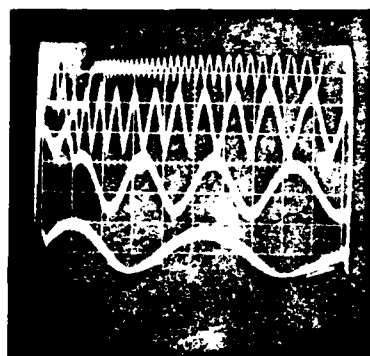
FIG. A.8-2. Laser Rod Cooling Fringe Count. Time base: 2 sec/div for about 15 sec; 5 sec/div thereafter.

4. The fringe counting photograph of Fig. A.8-2 also indicates the rate at which the laser rod cools with time toward the ambient air temperature and indirectly supplies information regarding the heat transfer (or film) coefficient, which is established by a consideration of the pump cavity geometry, the coolant mass flow rate, and physical properties of the coolant and laser rod.

NOTES:

1. The contactless method of measuring laser rod temperature was an offshoot of interferometric studies in laser pump cavity design as described in Appendix C-2.

2. The surface heat transfer coefficient for the laser rod using both FC-104 and water coolant is derived in Appendix C-5.

Appendix A-9

TECHNIQUE TO ACCURATELY SET EFFECTIVE REFLECTIVITY
IN A TWO-ELEMENT TVR RESONATOR

1. The present technique for measuring the effective reflectivity of a laser resonator involves the use of a calibrated end mirror and two calibrated radiometers. Since the calibrated end mirror has a very high reflectivity and the ambient light levels during the reflectivity calculations are subject to change, the PD manufacturers and the Laser Designator/Rangefinder Branch have damaged lithium niobate modulators inadvertently during this procedure. Since the T-beam will employ a 25-mm-long modulator, it was felt necessary to establish a better means of setting the resonator reflectivity to reduce the likelihood of damage to the 25-mm modulator in-house. The technique for the reflectivity calibration is described in the following paragraphs.

2. Figure A.9-1 shows the typical resonator layout. The quarter-wave plate encounters plane polarized light returning through the calcite prism. The polarized light passes through the quarter-wave plate twice which makes it behave somewhat like a half-wave plate (Fig. A.9-2). The polarizer axis (the orientation established by the calcite) is parallel to the plane of the page in Fig. A.9-1. The electric vector E describes that direction. The quartz quarter-wave plate optic axis and fast axis are orthogonal. The projections of E can be written as

$$E_{\perp} = E \cos \theta = E_m \sin wt \cos \theta \tag{1}$$

$$E_{\shortparallel} = E \sin \theta = E_m \sin wt \sin \theta \tag{2}$$

which represents a plane polarized waveform propagating at an angle θ to the quarter-wave plate fast axis. The E component encounters a phase shift of π upon two passes through the quarter-wave plate so that
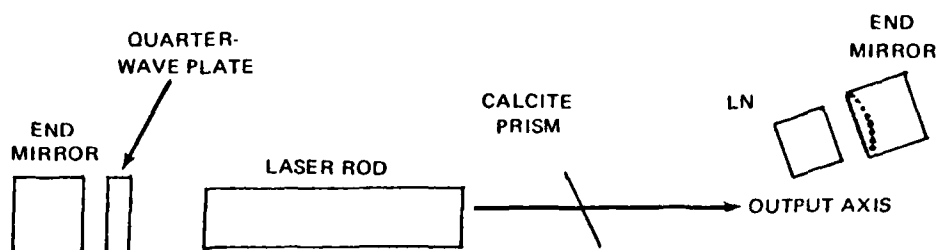
$$E_{\shortparallel} > - E_m \sin wt \sin \theta \tag{3}$$

Hence the components are still in phase. We are interested in the projection of our new electric vector E' along the polarizer axis. Hence it follows that

$$E_p = E^{\shortparallel} \cos 2\theta \tag{4}$$

The transmission is related to the wave amplitude squared so

$$T = E_p {}^*E_p = \cos^2 2\theta \tag{5}$$

ALL COMPONENTS ARE ON INDIVIDUAL ADJUSTABLE MOUNTS ALLOWING EASE IN
REPLACEMENT AND ALIGNMENT.

ONE END MIRROR IS IN A LANSING MOUNT ALLOWING FINE TUNING; THE OTHER
END MIRROR IS IN A TROPEL MOUNT TO GET THE "START-LASING" CONDITION.

THE MODULATOR IS ADJUSTABLE TO MAKE THE RESONATOR AXIS AND THE OPTIC
AXIS FIGURE PARALLEL USING THE MALTESE CROSS TECHNIQUE.

THE QUARTER-WAVE PLATE IS IN A CALIBRATED ROTATIONAL MOUNT BY WHICH
EFFECTIVE OUTPUT REFLECTIVITY CAN BE READ INDIRECTLY (WITHIN A FEW
PERCENT).
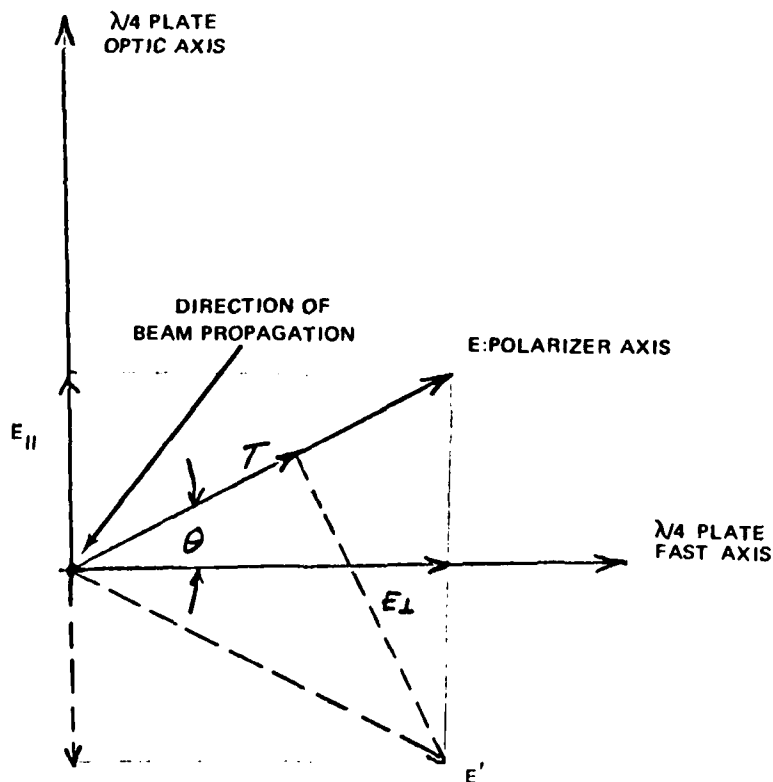
FIG. A.9-1   Resonator Layout.

FIG. A.9-2.   Beam Propagation to the
Quarter-Wave Plate.

by normalization of the incident intensity. In summary then, if one impresses plane polarized light at an angle from the fast axis of a quarter-wave plate, then after two passes, $\cos^2 2\theta$ of the incident energy remains in that incident plane of polarization. The reflectivity is given then by

$$R = 1 - T = \sin^2 2\theta \qquad (6)$$

3. Under careful test conditions, the effective reflectivity had been measured at the PD manufacturer's yielding the R(expt) values given in Table A.9-1. The values of R(theor) are given by Eq. 6.

TABLE A.9-1. Effective Reflectivity.

θ-value, deg	R_E(Expt), %	R_T(theor), %	$(R_E - R_T)$, %
10	21.3	11.7	9.6
15	29.5	25.0	4.5
19	39.0	38.0	1.0
25	59.0	58.8	0.2
30	74.0	75.0	1.0
35	87.0	88.1	1.1
40	96.0	96.85	0.85

As evident from Table A.9-1, the reflectivity values agree particularly well at high reflectivity values. Note too, that the laser rod birefringence was negligible in the reflectivity data obtained. Hence this theoretical method suggests a solution to the damage problem encountered in the past.

4. With the use of two-element time-varying reflectance (TVR), the power density internal and external to the resonator are related by

$$P_{in} = (1 + R)P_o/(1 - R) \qquad (7)$$

and for the case R = 0.70, it follows that

$$P_{in} = 5.67 \ E/t \ A_\ell \qquad (8)$$

where

    E = energy output, J
    t = pulse width
    A_ℓ = lasing area

Note that the entire rod does not lase. The author has shown experimentally that the lasing diameter is near 0.233 inch. Therefore, it follows that

$$P_{in} = 1.2\ E_{out}\ (mJ)(MW/cm^2); \tag{9}$$

that is, an energy output of 100 mJ produces a peak power density (assumed uniform over 0.233 inch) of 120 MW/cm^2. Once P_{in} is set, the allowable E_{out} (mJ) is set, given a reflectivity of 70%. To compensate for the difference of lasing diameter to physical diameter, the intraresonator power density becomes

$$P_{in} = 1.04\ E_{out}\ (mJ)(MW/cm^2) \tag{10}$$

5. The PD manufacturers have established 80 MW/cm^2 as the *safe* power density within the resonator. As is evident from Eq. 9, an energy output of 77 mJ is allowable at the optimum reflectivity of 70%. To obtain an energy output of 100 mJ without exceeding the safe power density within the resonator requires lowering the output reflectivity; i.e., detuning as the PD presently does. It can be shown directly that reducing the output reflectivity to 63% allows a 100 mJ output. The resonator is approximately 5% less efficient at this reflectivity setting. Hence the resonator can be operated at a reflectivity of 60% with an allowable energy output of more than 100 mJ. The technique for setting this resonator effective output reflectivity was suggested earlier. It must now be made to include the errors in setting that reflectivity value.

6. One other significant point regarding resonator power density needs to be made. Preliminary tests have indicated that the close-wrapped pump configuration produces a 12-nsec output pulse width. To obtain an energy output of 100 mJ without exceeding the safe power density then requires an effective reflectivity of about ??%. This causes a degradation in output of 18% or the output reduces to 72 mJ. As a result to achieve an output of 100 mJ, the pump energy must increase proportionally. Hence the use of a close-wrapped pumping configuration represents a considerable design compromise not to be pursued any further here.

7. To obtain an effective reflectivity of 60%, then one requires by Eq. 6 that $\theta = 25°23'$ with the incident plane of polarization. The quarter-wave plate makes an angle $\theta = 25°23'$ with the incident plane of polarization. The quarter-wave plate mount is shown in Fig. A.9-3, and the incident plane of polarization E_0 is also indicated. A means of setting the quarter-wave plate within its mount is needed, given θ. Before this is done, however, some estimates are needed on the possible error in reflectivity setting.

8. The possible sources of error in reflectivity setting are the retardation tolerance on the quarter-wave plate, the mounting tolerance itself, and effects of component birefringence. The mounting tolerance depends on the angle θ, as in Eq. 6.

INCIDENT PLANE
OF POLARIZATION

REFERENCE
SURFACE

SCALE = 4:1

λ /4 PLATE HOLDER
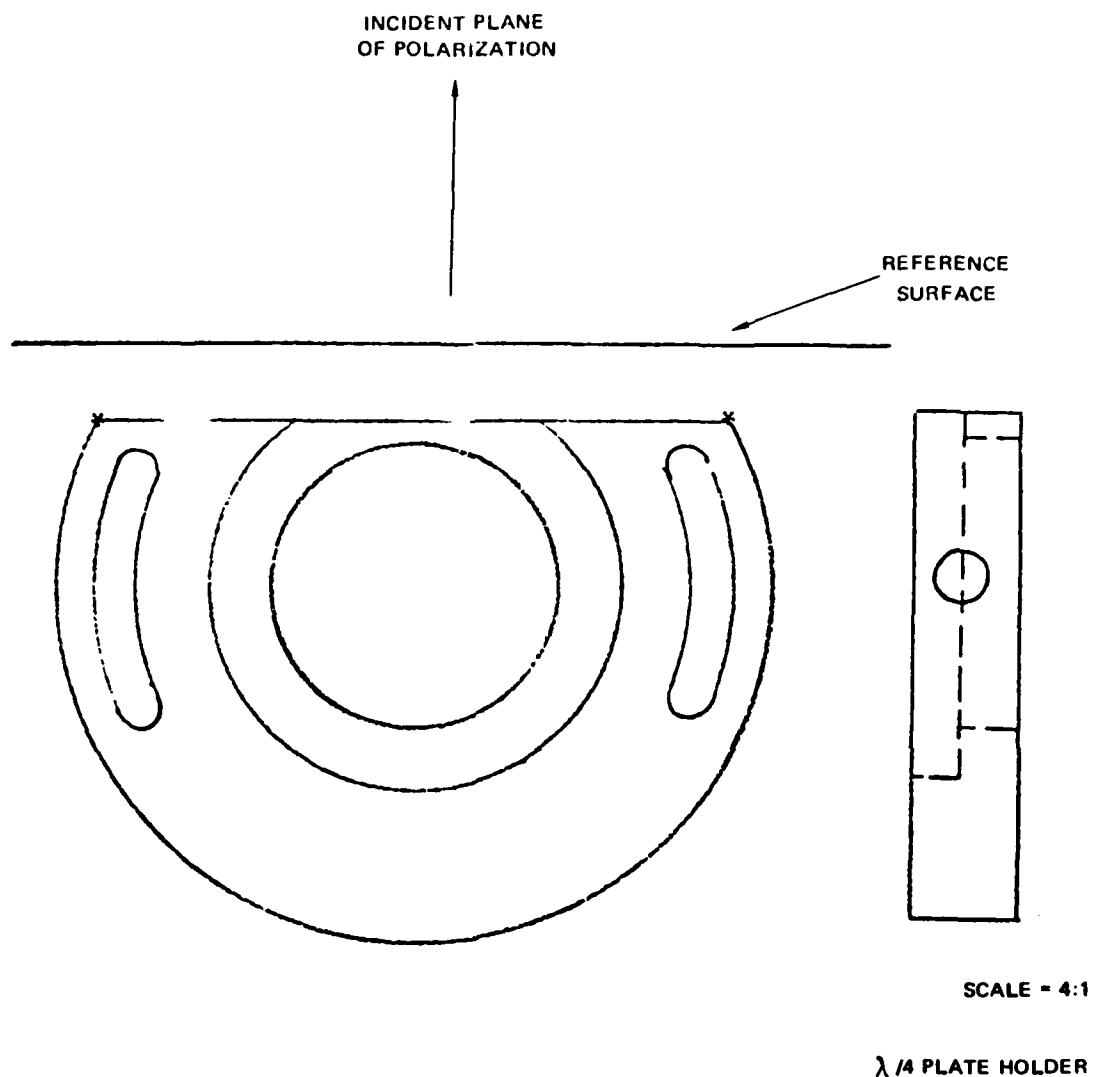
FIG. A.9-3.

$$dR/d\theta = 4 \sin 2\theta \cos 2\theta = 4 \sin 4\theta$$

or

$$dR = 1.96 \ d\theta \ \text{at} \ \theta = 25°23' \qquad\qquad (11)$$

indicating that as θ increases, R (and power density) increases. A reference surface is available to align the mounting structure accurately. Placement of the alignment scribes (*) within 0.005 inch causes dR = 1.2% as the maximum error in mounting tolerance.

9. The specifications for the laser rod indicate a maximum allowable birefringence of 0.5%. The birefringence of the calcite prism polarizer represents a loss to the resonator and need not be included here.

10. The final possible contributor to the reflectivity setting is the retardance tolerance on the quarter-wave plate. The specifications call out $\lambda/4 \pm \lambda/50$ as the tolerance. The net result of an error in the retardance is that, substituting in Eq. 2

$$E_{\parallel} = E_m \sin (wt + \pi + \frac{8\pi}{100}) \sin \theta$$

$$E_{\parallel} = E_m \sin (0.9686 \sin wt \pm 0.2487 \cos wt) \tag{12}$$

which causes the superposition of linearly polarized light and elliptically polarized light. Since the components are now equivalently out-of-phase with $E_{\perp}$, eliptically polarized light is transmitted by the quarter-wave plate. Because of this possible phase-retardance tolerance of 14°24', it can be shown that the effective reflectivity becomes

$$R = 4 \sin^2 \theta \cos^2 \theta \sin^2 (\frac{\pi}{2} \pm 7°12')$$

$$= 4 \ (0.42867)^2 \ (0.90346)^2 \ (0.99211)^2$$

$$R = 0.5906 = 59.06\% \tag{13}$$

So the reflectivity changes by approximately 1% maximum because of the retardance tolerance. Assuming that the errors are additive, the total possible error in reflectivity setting is about 2.6%.

11. The fast axis of the quarter-wave plate must lie at 25°23' from the incident plane of polarization to obtain an effective reflectivity of $60 \pm 2.6\%$. Figure A.9-4 describes the technique for marking the quarter-wave plate mounting structure to accomplish this. By the geometry, the distance

$$X = 0.2125 \ \tan 25°23' = 0.2125 \ (0.4745)$$

$$X = 0.101 \text{ inch} \tag{14}$$

Hence, a scribe mark at distance X from the centerline (horizontal on the T-beam) should correspond to the fast axis as marked on the quarter-wave plate. This then establishes the effective output reflectivity at 60% and ensures power density does not exceed the safe level derived by the PD manufacturers for output energies up to 100 mJ.

12. The use of a close-wrapped pumping configuration was discussed in paragraph 6. The considerable level of detuning required makes it less desirable for use in the T-beam. The safe level established by the PD manufacturers was established as that power density where few damaged modulators occurred statistically. It would appear that the use of a

FAST AXIS

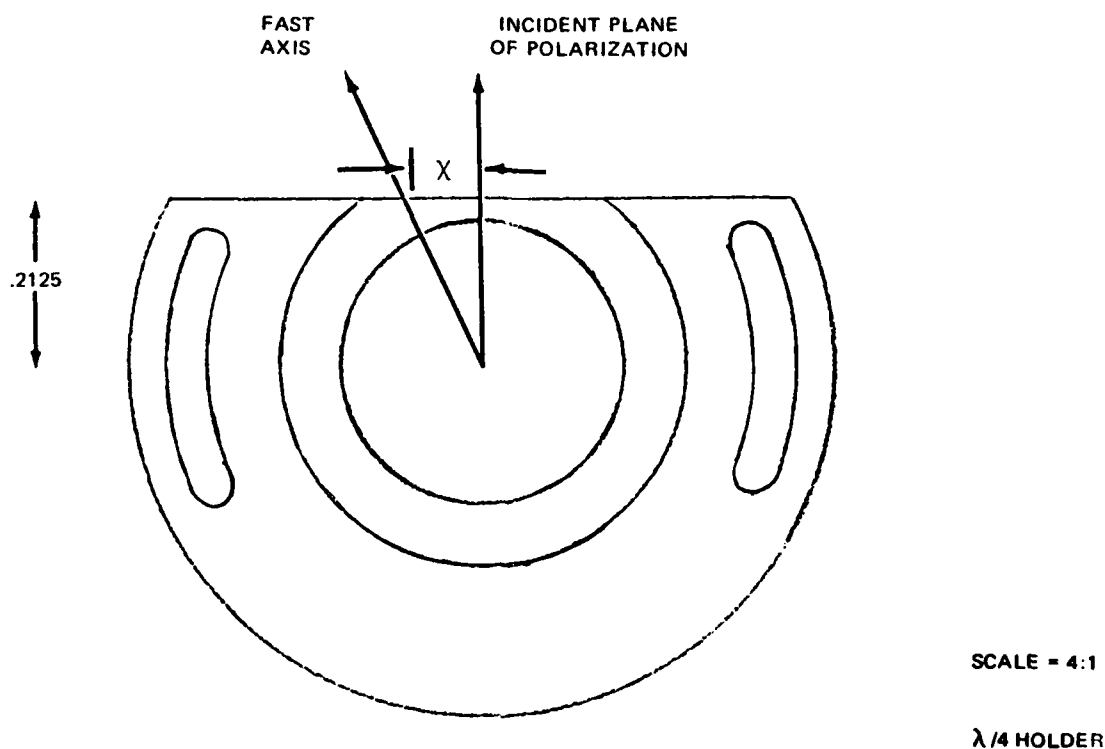INCIDENT PLANE OF POLARIZATION

X

.2125

SCALE = 4:1

λ/4 HOLDER

FIG. A.9-4.

cylindrical pumping enclosure for a given energy input would provide more output energy even if the modulator were damaged. Hence, the use of a cylindrical pumping enclosure with an effective output reflectivity of 60% seems a very reasonable design approach.

NOTES:

1. "Two-element TVR" is a resonator design approach which allows setting the effective reflectivity by rotating a component rather than by replacing one.

2. The relative energy output for the T-beam as a function of effective reflectivity is shown in Appendix H.3. There are cases where a "detuned" (reduced) reflectance from the optimum value possible is required to protect resonator components from the high-peak power density possible.

3. The quantitative discussion regarding the intraresonator peak-power density is not exact. The Q-switched beam uniformity is discussed in Appendix F.2 and shows that the maximum peak-power density is appreciably larger than P_{in} of Eq. 9 would indicate. However, the technique as described to set reflectivity remains correct and unaffected.

4. This technique for setting the effective reflectivity is presently in use and consistent with the technique described in paragraph 1 of these notes.

5. It is planned to scribe mark the T-beam showing the quarter-wave plate mount position required to set the reflectivity to any desired value (within reasonable angular increments).

Appendix A-10

ALIGNMENT WEDGE REQUIREMENT

1. The present T-beam has only a pair of alignment wedges for dynami-
cally tuning the resonator to optimize its operating efficiency. These
alignment wedges presently align one end mirror with respect to the
other end mirror, which has the laser rod (actually the entire pump cav-
ity assembly) aligned with it in an approximate way. The alignment of
the laser rod to this second end mirror is done by superposition of
reflected light (6328Å) from the end mirror surface and the nearest
laser rod end face. By applying torque to the pump cavity assembly
while lasing (with due regard for the high voltages there), the author
has shown that an increase in efficiency of about 20% is realizable.
It has been shown that an alignment wedge mismatch (in terms of wedge
angle) was the major cause of the efficiency loss. If the wedges are
not an accurately matched pair, it is possible that an accurate resonator
alignment is not possible. By applying torque to the pump cavity and
the subsequent torque on the T-beam assembly itself, more accurate align-
ment of one end reflector with respect to the other was realized.

NOTES:

1. The T-beam resonator has fixed, nonadjustable end mirrors. The
   manufacturing tolerances on the T-beam are such that improved
   resonator alignment is required. This alignment capability is
   provided by the wedges, which have an alignment capability, slightly
   larger than the error in mirror misalignment possible due to manu-
   facturing tolerances.

2. The insertion loss of the alignment wedges is described in Appendix
   A-6.

3. Neither an adjustable end mirror nor a second set of alignment wedges
   has been incorporated into the T-beam design as yet.

Appendix B

FLASHLAMPS AND FLASHLAMP DRIVE CIRCUIT DESIGN

Appendix B.1

KRYPTON- VERSUS XENON- FILLED FLASHLAMP PERFORMANCE COMPARISON

1. The major testing was to investigate the characteristics of new flash-lamps received recently, including xenon and krypton Germasil and xenon and krypton Heliosil flashlamps. The input energy for all the test results was 7.8 J, the capacitance (C) was 14.8 µF, and the inductance (L) was near 30 µH.

2. The results of the tests were as follows:

a. The peak current for the krypton-filled flashlamp is approximately the same as that of the xenon-filled flashlamp but is slightly lower.

b. The flashlamp parameter K_0 for a krypton flashlamp at 1,500 torr is slightly larger than a xenon flashlamp at 450 torr.

c. The peak of the current pulse is delayed from 20 µsec after the occurrence of the flashlamp trigger pulse (ϕ_{FLT}) with respect to the xenon flashlamp current waveform. Hence, it is anticipated that for the use of a krypton-filled flashlamp in the LWL, the timing delay of the pockel-cell trigger pulse (ϕ_{PCT}) with respect to ϕ_{FLT} should be increased by approximately 20 µsec as well.

d. The time separating the peak of the fluorescence curve and the peak of the flashlamp current curve is the same for both flashlamp types and is about 160 µsec.

e. The fluorescence output is approximately 10% higher in krypton, as compared to xenon. Hence, an efficiency increase of at least 10% should be realizable using krypton flashlamps since the LC character-istics are likely less than optimum for this lamp.

f. The reliable trigger voltage is approximately 50% higher for the krypton flashlamp as compared to the xenon flashlamp. It should be added that the cylindrical pump cavity is considerably more diffi-cult to parallel trigger than the close-coupled pump cavity.

g. The current pulse half-width is approximately 10% longer for krypton as compared to xenon flashlamps.

h. On the basis of the seven flashlamps tested, no quantitative conclusions were possible regarding the fluorescence level by flashlamps

using Germasil versus Heliosil envelopes. The reason for this was that the fluorescence level from flashlamp to flashlamp (of one gas-filled type) varied significantly.

i. Krypton-filled flashlamps show appreciably lower threshold energy levels but lower slope efficiencies than xenon-filled flashlamps. As a result the efficiency curves for these two gases will always cross. The crossover point depends mostly upon the pump cavity efficiency and the LC character of the discharge circuit used. Recent tests by Sylvania had the crossover point near 40 J.

j. The krypton-filled flashlamps are preferred over the xenon-filled flashlamps, especially at low pumping levels. The threshold level using Kr- and Xe-filled flashlamps was typically 1.75 and 3.07 J, respectively.

NOTES:

1. Considerable flashlamp data have been generated by International Lamp Corp., Inc. (ILC), manufacturer of the flashlamps used.

2. The terminology "ϕ_{FLT}" refers to the flashlamp trigger pulse and from whose time of occurrences the modulator trigger pulse (ϕ_{PCT}) is delayed. It has been found that the ($\phi_{FLT} - \phi_{PCT}$) time delay has increased from 105 μsec to near 120 μsec now that Kr rather than Xe flashlamps are in use. (The time delay required is established by efficiency and multiple-pulsing considerations.)

3. Kr-filled flashlamps at 1,000-torr fill pressure are most often used in in-house lasers.

4. The flashlamp trigger voltage is strongly dependent on the energy storage capacitor voltage at low-input pump levels.

5. The laser rod fluorescence measurements were made at 1 Hz using a spectroradiometer to read peak fluorescence output voltage.

6. The parameter K_0 was measured incorrectly here and is given instead in Appendix B-2.

7. Comparative lasing efficiency data of the Kr- versus Xe-filled flashlamps are supplied in Appendix E-3.

Appendix B.2

TIME DEPENDENCE OF Kr- AND Xe- FILLED
FLASHLAMP IMPEDANCE .

1. The flashlamp discharge circuit consists essentially of a fixed capaci-
tance, a fixed inductance, a fixed resistive loss, and a time-dependent
flashlamp impedance. The major resistive loss is in the windings of the
series inductor (which is present to increase the flashlamp pump pulse
duration and lower the peak current through the flashlamp). The time-
dependent flashlamp resistance has been measured by the author for both
krypton- and xenon-filled flashlamps. The series inductance and input
energy were varied, and the effect on the time dependence of the flash-
lamp resistance was noted. A fixed capacitance of 18.8 μF was used. The
fill pressure for the Xe- and Kr-filled flashlamp was 450 and 1,000 torr,
respectively. The series inductance of 11.3, 33.3, and 44.6 μH had a
measured resistance of 77, 240, and 317 mΩ, respectively. The flashlamp
parameter K_0 was also measured and the value obtained for xenon was in
agreement with the manufacturer's value. The flashlamp data obtained on
the time dependence of the flashlamp impedance and the agreed-upon value
of K_0 are to be used in an analysis of the flashlamp drive circuit design;
discussion is presented later in this report. The krypton flashlamp data
were taken to support the flashlamp drive circuit design for the PADS unit.

2. Figure B.2-1 shows the test schematic and equipment. A Tektronix, Inc.
P 6015 high-voltage probe and a Pearson Electronics, Inc. Model 410 pulse
current transformer were used to measure flashlamp voltage and current
simultaneously. Typical flashlamp voltage and current waveforms are shown
in Fig. B.2-2. Measurements for the voltage-to-current ratio were made
directly from the oscilloscope photographs taken. The time dependence of
the flashlamp resistance for both krypton- and xenon-filled flashlamps
for variable inductance and input energy is given in Fig. B.2-3 and -4.
Representative plotting data for xenon are given in Table B.2-1. The
product of flashlamp voltage and current (IV) is also listed.

3. The flashlamp parameter K_0 was established from the value of flashlamp
voltage and current at the minimum conducting resistance value. The aver-
age value of K_0 for xenon- and krypton-filled flashlamps yielded 26.0 and
26.2 Ω-A$^{1/2}$, respectively. The flashlamp manufacturer, ILC, Inc., claims
K_0 is near 25 Ω-A$^{1/2}$ for the xenon flashlamp used. No data were immediately
available for the krypton K_0 value at 1,000-torr fill pressure. It is
apparent from the data that the minimum conducting resistance for both
flashlamp types is approximately 1.5 Ω. It is also evident that, for a
given LC product and input energy, the krypton- and xenon-filled flashlamp
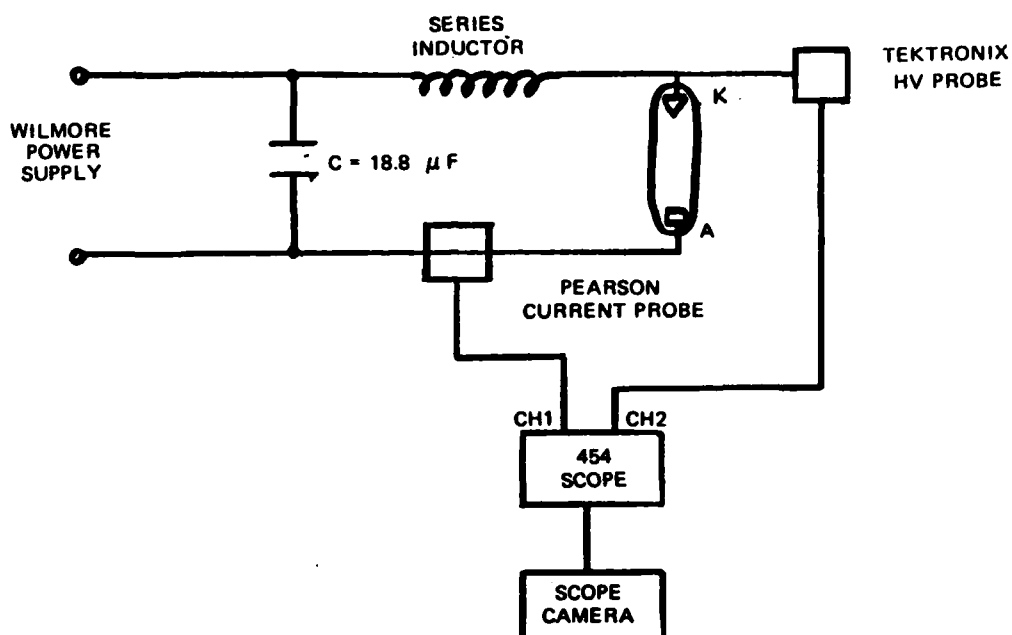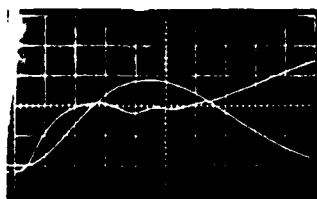pump pulse width, peak current, and K_0 value are essentially equal.

FIG. B.2-1. Test Schematic and Equipment.

NOTES:

1. The IV product shown in Table B.2-1 is used in the analysis of Appendix B-3.

2. The impedance waveforms of Fig. B.2-3 and -4, together with ILC, Inc. data, establish the worth of the delayed triggering concept described in Appendix B-5.

_V·40° A-30° Ko·23.1_

Time base, µsec/div.	10		10
Voltage, V/div..........	200	....	200
Current, A/div..........	100	....	100
Cap V, V..................	830	....	1,000
Inductor, µH............	33.3	....	33.3

Xe-filled flashlamp at 450 torr
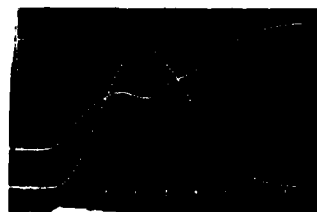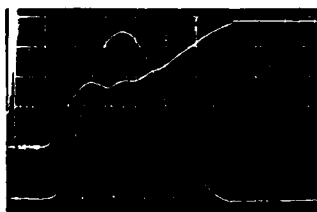
Time base, µsec/div.	20		10
Voltage, V/div........	200	....	200
Current, A/div........	50	....	100
Cap V, V................	862	....	942
Inductor, µH..........	33.3	....	11.3

Kr-filled flashlamp at 1,000 torr

FIG. B.2-2. Representative Voltage-Current
Waveforms for Xenon and Krypton.

$\frac{800}{250}$ _v_ _A_

FIG. B.2-3. Time Dependence of Xe Flashlamp Impedance for
Several Input Energies and Series Inductance Values.
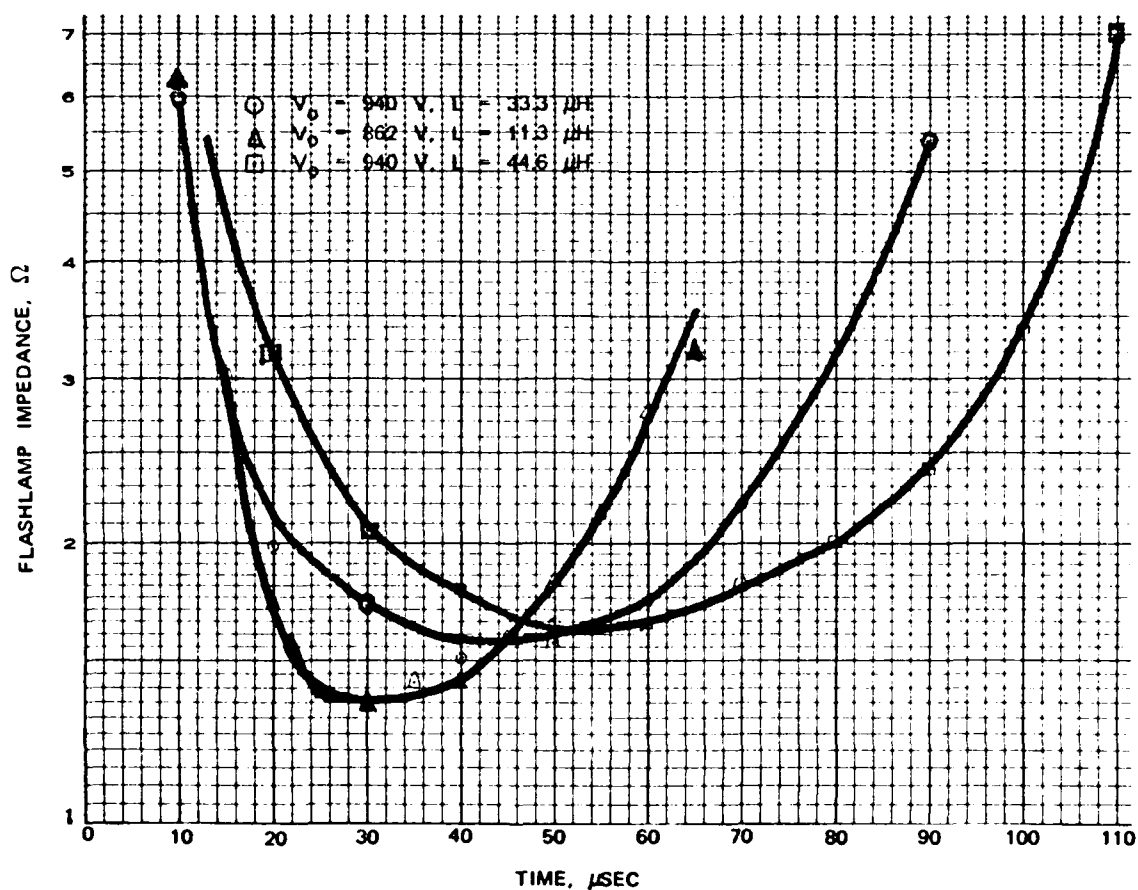
FIG. B.2-4. Time Dependence of Kr Flashlamp Impedance for
Several Input Energies and Series Inductance Values.

TABLE B.2-1. Representative Plotting Data for
Xenon-Filled Flashlamps.
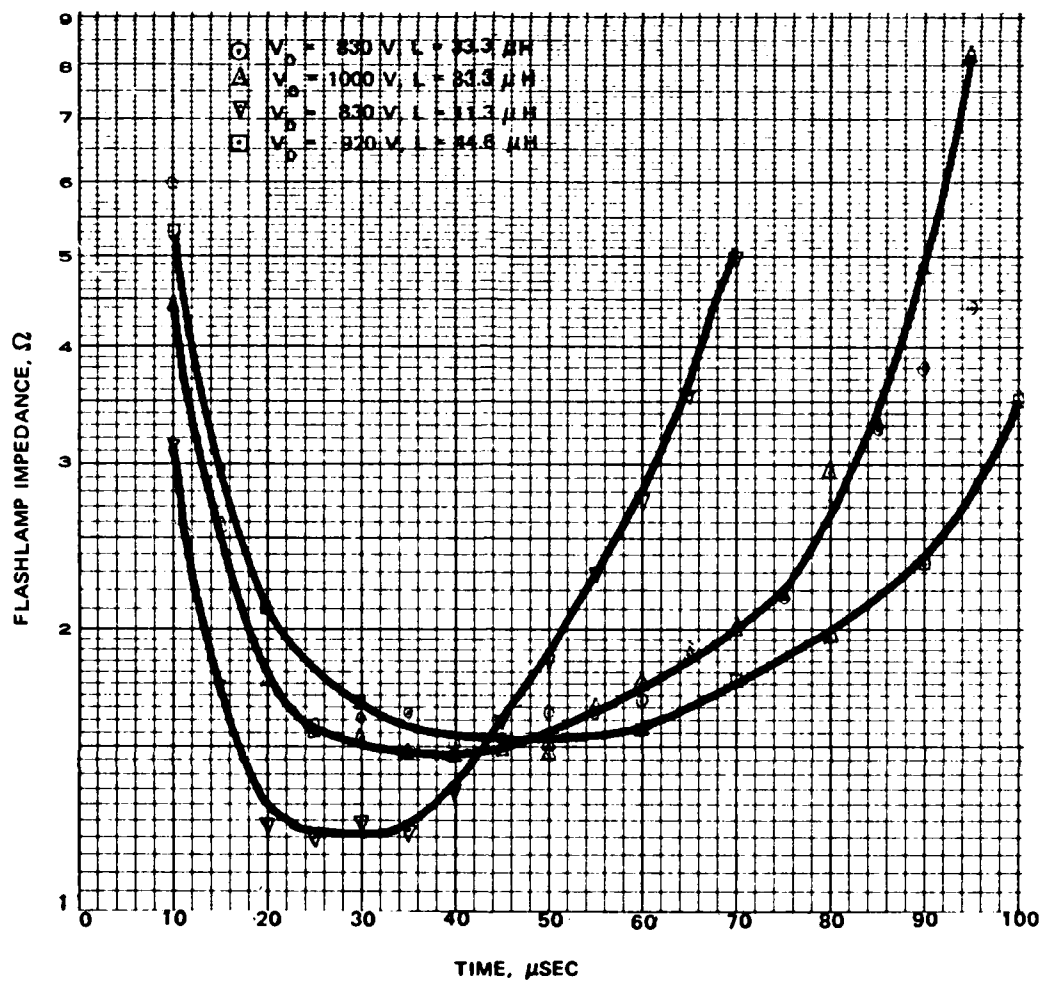
Case parameters: V_o = 1,000 V, L = 33.3 μH,
C = 18.8 μF

Time,	Flashlamp			
μsec	Voltage, V	Current, I	Resistance, R	Product, IV x 10^4
5.0	640	48	13.35	3.07
10.0	505	116	4.4	5.85
15.0	475	185	2.56	8.90
20.0	465	263	1.76	12.22
25.0	490	316	1.55	15.50
30.0	520	340	1.53	17.70
35.0	520	355	1.47	18.50
40.0	520	355	1.47	18.50
45.0	505	340	1.48	17.2
50.0	470	318	1.47 ◄	14.8
55.0	465	283	1.64	13.1
60.0	430	245	1.75	10.5
65.0	375	206	1.87	7.7
70.0	340	170	2.0	5.8
75.0	292	133	2.19	3.9
80.0	250	85	2.94	2.1
85.0	215	65	3.32	1.4
90.0	160	33	4.86	0.53
95.0	106	13	8.15	0.14
				177.4

$$K_0 = \frac{470}{\sqrt{318}} = 26.4$$

Appendix B.3

THEORY VERSUS PRACTICE FOR Xe-FILLED FLASHLAMPS

1. The reprint, presented in the following pages, describes the design considerations necessary to optimize a single mesh flashlamp drive circuit. A digital computer was used to solve a normalized nonlinear differential equation which describes the flashlamp drive circuit in general terms. The theory provides the values for the *optimum* inductance, capacitance, and energy storage voltage to be used after the input energy, pump pulse duration, shape factor α, and flashlamp parameter K_0 are known. It also provides an estimate of the series resistive loss for a given shape factor and LC product of the flashlamp drive circuit. The reprint is used extensively in establishing the results given in this B-3 portion of Appendix B, the purpose of which is to compare the theory given in the reprint with the experimentally measured flashlamp drive circuit parameters and interpret any differences which arise. At the same time the limitations of the theory will be made clear.

2. Appendix B-2 shows the time dependence of xenon- and krypton-filled flashlamp impedance for several input energies and inductance values (the equivalent of several values of Z_0 and shape factor α). The flashlamp parameter K_0 was also calculated as was the flashlamp voltage-current product IV (as given in Table B.2-1 of Appendix B-2) which corresponds to shape factor $\alpha = 0.70$. It is intended to compare the theory of the reprint with experimental results using equal flashlamp drive-circuit parameters throughout. By using Eq. 4, 5, and 13 of the reprint, the peak current, pump pulse duration, and resistive loss factor, shown in Table B.3-1, follow directly where the latter assumes a 240-mΩ inductor winding resistance and a shape factor of 0.70. The experimental loss factor was obtained by summing the IV product in 5-μsec intervals for the case parameters of Case #3, Table B.3-1, and comparing this energy to that stored on the energy storage capacitor. This case is also that provided in the plotting data of Appendix B-2, Table B.2-1. The loss factor discrepancy is resolvable from an examination of the normalized power input (P_N) characteristic defined by Eq. 10 in the reprint and in the results of Appendix B-2. The data of Table B.3-2 were used to plot the P_N and E_N curves defined in the reprint and given in Fig. B.3-1, which correspond to the case parameters #3 and the shape factor 0.70 of Fig. 5 in the reprint. From the P_N plots of Fig. B.3-1, it is apparent that the theory assumes a much lower conducting flashlamp resistance in the first 25 μsec of the current pulse than is actually present in practice. (The maximum amplitude difference in the P_N value is attributed to the difference in peak current between theory and experiment.) As a result, the effect of a series resistive loss is appreciably larger in theory than in practice since the average flashlamp impedance during the current pulse is much larger than Z_0. Those parameters such as peak current and pump pulse

TABLE B.3-1. Flashlamp Drive-Circuit Parameters, Theory Versus Practice.

Case parameters	Shape factor, α	Z_o, Ω	Peak current, A		Pulse width, μsec		Loss factor, %	
			Theor.	Experiment	Theor.	Experiment	Theor.	Experiment
#1: V_o = 830 V, L = 33.3 μH	0.766	1.333	322	285	75	85	15.0	6
#2: V_o = 910 V, L = 33.3 μH	0.734	1.333	362	320	75	85	16.3	7
#3: V_o = 1000 V, L = 33.3 μH	0.700	1.333	410	355	75	85	17.7	5.5

TABLE B.3-2. Plotting Data for P_N and E_N.

| t, μsec	τ	IV, 10^4	P_N	E_{in}, J	ΣE_{in}, J	$E_N (=\Sigma E_{in}/8.89$ J)
5.0	0.2	3.07	0.041	0.1535	0.15	0.017
10.0	0.4	5.85	0.078	0.292	0.44	0.05
15.0	0.6	8.90	0.119	0.445	0.89	0.10
20.0	0.8	12.22	0.163	0.611	1.50	0.17
25.0	1.0	15.50	0.207	0.775	2.28	0.257
30.0	1.2	17.70	0.236	0.885	3.16	0.356
35.0	1.4	18.5	0.247	0.925	4.08	0.460
40.0	1.6	18.5	0.247	0.925	5.01	0.565
45.0	1.8	17.2	0.229	0.860	5.87	0.661
50.0	2.0	14.8	0.197	0.740	6.61	0.746
55.0	2.2	13.1	0.175	0.655	7.26	0.818
60.0	2.4	10.5	0.140	0.525	7.79	0.877
65.0	2.6	7.7	0.1025	0.385	8.17	0.920
70.0	2.8	5.8	0.077	0.290	8.46	0.954
75.0	3.0	3.9	0.052	0.195	8.66	0.976
80.0	3.2	2.1	0.028	0.105	8.78	0.989
85.0	3.4	1.4	0.0187	0.070	8.85	0.9955
90.0	3.6	0.53	0.007	0.0265	8.88	0.999
95.0	3.8	0.14	0.00187	0.007	8.89	1.000
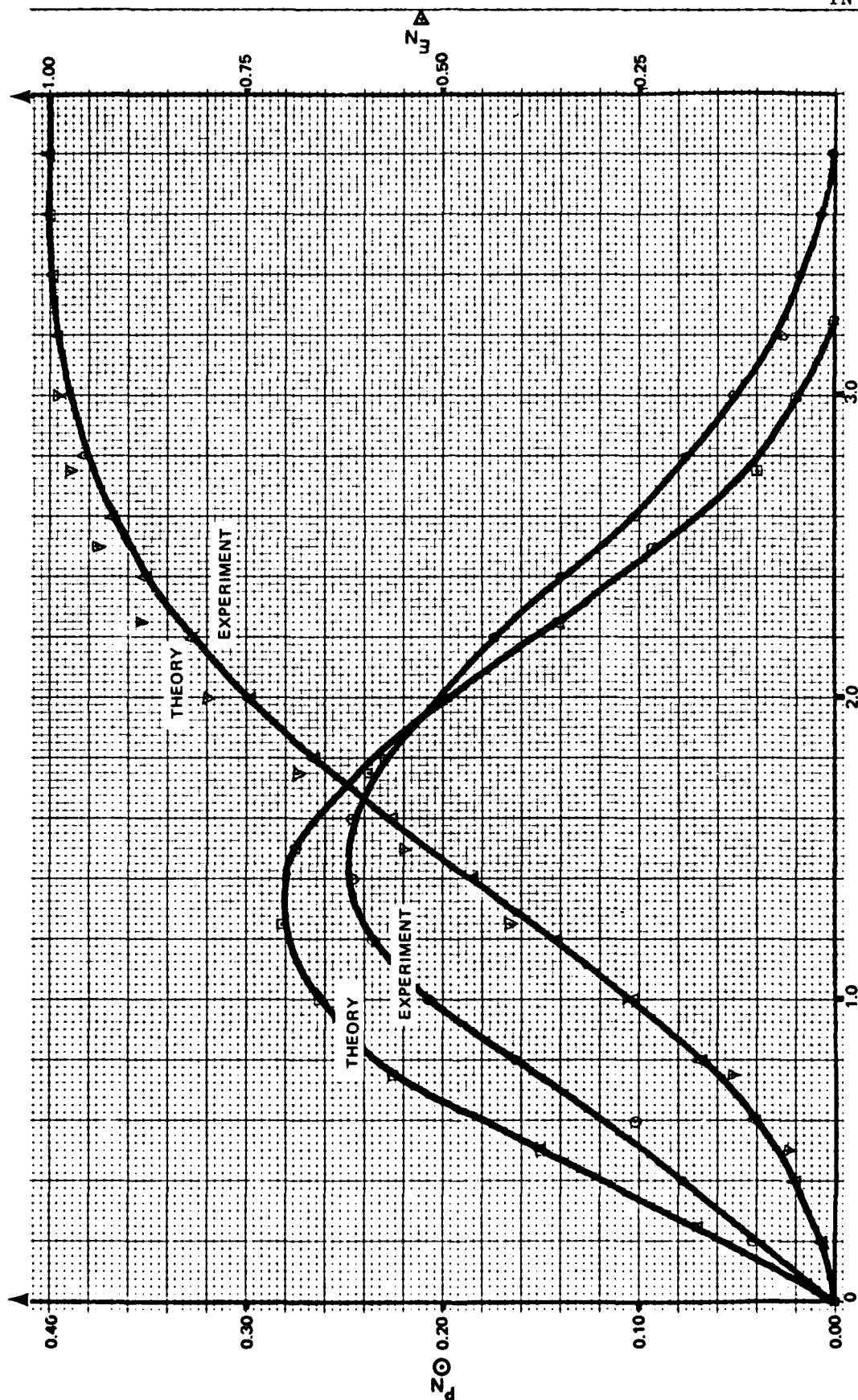
TIME PARAMETER τ

FIG. B.3-1.

duration are more dependent on the LC character of the discharge circuit than on the time dependence of the flashlamp impedance. Hence good agreement is present between theory and practice for these parameters. The increased flashlamp impedance in practice is attributed to a flashlamp arc diameter appreciably smaller than the maximum possible diameter of 4 mm and the fact that the flashlamp resistance varies inversely as the square of the arc diameter. As a result, the use of the theory of the reprint provides adequate design guidelines for the flashlamp drive circuit, except the resistive loss estimates are grossly in error.

NOTES:

1. The data generated here can be used to help show that the gain in efficiency using the delayed triggering concept is small as shown in Appendix B.5. From Table B.3-2 it is evident that about one J of energy (compared to the 9-J input) was used in complete arc formation (arc generally fills the capillary).

2. The PD manufacturers have done a study which indicates that, generally speaking, the flashlamp drive circuit is relatively flexible as to parameter selection without significantly affecting operating efficiency.

3. The impedance Z_0 is a flashlamp drive circuit parameter and is not the true flashlamp impedance. However, Appendixes B-3 and B-4 do not treat them as distinguishable parameters.

Design of Flashlamp Driving Circuits

J. P. MARKIEWICZ AND J. L. EMMETT

Abstract—The problem of design of single mesh circuits for driving xenon flashlamps has been considered in detail. The normalized nonlinear differential equation $I' \pm \alpha |I|^{1/2} + \int_0^\tau I\, d\tau = 1$ for this system has been solved by digital computer and the solutions are presented. Since the equation is linear in time, though nonlinear in current, it is possible to provide explicit design equations. With them, for a given lamp type, energy input, pulse duration, and pulse shape factor, the inductance, capacitance, and operating voltage are easily determined. A procedure for estimating circuit losses is also presented.

L INEAR and helical xenon flashlamps have become the standard pump sources for pulsed solid-state lasers, and have also found a wide variety of other uses. These lamps are usually operated from single or multiple mesh LC networks. Since very little engineering data on the various types of flashlamps has been available, the driving networks have, in many cases, been rather haphazardly designed. In the case of a single mesh circuit, the capacitance is usually chosen with regard only to the energy storage at a convenient voltage; the inductance is chosen to prevent explosion of the flashlamps. A simple design procedure is presented here which allows optimization of single mesh flashlamp driving circuits.

The problem of circuit design would, of course, be trivial if the flashtube were a linear resistor. This, however, is not the case. It has been shown[1,2] that the voltage-current characteristic of the flashlamp for the high current region can, under certain circumstances, be represented as

$$V = \pm K_0 |i|^{1/2}. \qquad (1)$$

The sign is chosen to be the same as the sign of i. The regions of validity of (1) and other deviations from this model are discussed later.

We will first consider how K_0 scales with the dimensions of the discharge volume. (The units of K_0 are ohms-amps$^{1/2}$.) Assume two discharge columns of equal length with diameters d and d'. The voltage drops across each of the two columns with current *density* J are equal.

$$V = K_0(\pi/4\ d^2 J)^{1/2} = K_0'(\pi/4\ d'^2 J)^{1/2},$$

[1] I. S. Marshak, *Sov. Phys. Usp.* (*English Trans.*), vol. 5, no. 3, pp. 478–514, 1962, and papers referenced therein.

[2] J. H. Goncz, *J. Appl. Phys.*, vol. 30, p. 742, 1965.

whence

$$K_0' = \frac{d}{d'} K_0$$

or

$$K_0 = k\frac{l}{d}, \simeq \frac{4}{3}\frac{\ell}{d} \qquad (2)$$

where l is length of discharge column. It should be emphasized that K_0 is inversely proportional to d, not to d^2. The constant k is then only dependent on such parameters as gas type, gas pressure, etc. K_0 or k is essentially the only parameter needed to describe the high current electrical characteristics of a given flashlamp. This is a number that could easily be supplied by the manufacturers of the flashlamps. K_0 is simply found by flashing the lamp at some reasonable loading, while measuring the voltage and current at a convenient time during the pulse.

We will now consider the flashlamp discharge circuit shown in Fig. 1. The nonlinear differential equation for this circuit is

$$L\frac{di}{dt} \pm K_0 |i|^{1/2} + \frac{1}{C}\int_0^t i\, dt = V_0. \qquad (3)$$
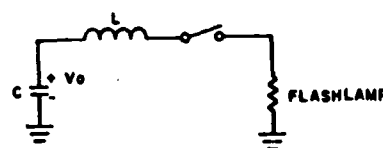
Fig. 1. Single mesh flashlamp discharge circuit.

It should be noted that only losses in the flashlamp are presently being considered, as the driving circuit is assumed lossless. If we make the following substitutions and normalizations:

$$Z_0 = \sqrt{\frac{L}{C}}, \quad i = I\frac{V_0}{Z_0}, \quad \tau = \frac{t}{T},$$

$$T = \sqrt{LC} \qquad (4)$$

$$\alpha = \frac{K_0}{(V_0 Z_0)^{1/2}}, \qquad (5)$$

Equation (3) becomes

$$\frac{dI}{d\tau} \pm \alpha |I|^{1/2} + \int_0^\tau I\, d\tau = 1. \qquad (6)$$

Note that the damping parameter α is dependent on V_0, the initial capacitor voltage. This is, of course, consistent with the experience that a discharge circuit, critically damped at one voltage, begins to ring as the voltage is increased.

Solutions of (6) for various values of α have been obtained using a digital computer. These curves for $\alpha = 0.2$ to $\alpha = 3.3$ are shown in Figs. 2–4. Differences between these solutions and those for the linear LCR circuit are readily apparent. For a given Z_0, V_0, and peak current, the solution of the nonlinear equation is more heavily damped than that of the linear case. The ideal under-damped linear LCR circuit has an infinite number of zero crossings in its current waveform, whereas the non-linear circuit has a finite number. As can be seen from these curves, $\alpha \approx 0.75$ corresponds to the critically damped case. Knowing the shapes of the curves for various values of α, it is now possible to design the proper discharge circuit.

The energy initially stored in the capacitor is

$$E_0 = \tfrac{1}{2}CV_0^2. \tag{7}$$

This relation is used to eliminate V_0 from (5) to give

$$C^3 = \frac{2E_0\alpha^4T^2}{K_0^4}. \tag{8}$$

We now have a set of three equations (4), (7), and (8) which, upon the specification of the flashlamp parameter K_0, the desired energy input E_0, the pulse shape α, and the time scale T, give explicit values of C, L, and V_0.

When more information becomes available on the optical characteristics of these devices, it is expected that the optical power output will correlate with the power input rather than with the current or energy. The power input is just

$$P = vi = K_0 |i|^{3/2}. \tag{9}$$

The normalized power is

$$P_N = \frac{P}{V_0^2/Z_0} = \alpha |I|^{3/2}. \tag{10}$$

Curves of P_N for various values of α from 0.2 to 3.3 are given in Figs. 5–7. The energy dissipated in the lamps is just $E = \int_0^t P \, dt$, while normalized energy is

$$E_N = 2\alpha \int_0^\tau |I|^{3/2} \, d\tau. \tag{11}$$

Curves showing E_N for various values of α from 0.2 to 3.3 are given in Figs. 8–10. These demonstrate the effect of flashlamp operation in circuits that are other than critically damped.

Until now the effect of circuit loss has not been considered. A constant resistive loss r in the circuit will produce a term ri in (3) which will modify (6) to be

$$\frac{dI_s}{d\tau} \pm \left[\alpha + |I_s|^{1/2}\frac{r}{Z_0}\right]|I_s|^{1/2} + \int_0^\tau I_s \, d\tau = 1, \tag{12}$$

Fig. 2. Normalized current for $\alpha = 0.2$ to 0.8.

Fig. 3. Normalized current for $\alpha = 0.8$ to 2.0.
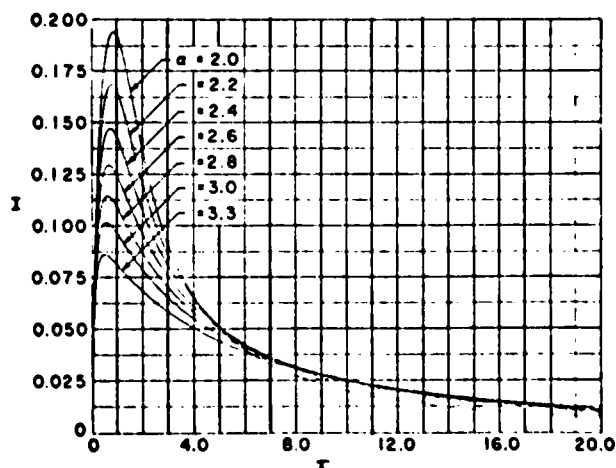
Fig. 4. Normalized current for $\alpha = 2.0$ to 3.3.

Fig. 5. Normalized power for $\alpha = 0.2$ to 0.8.

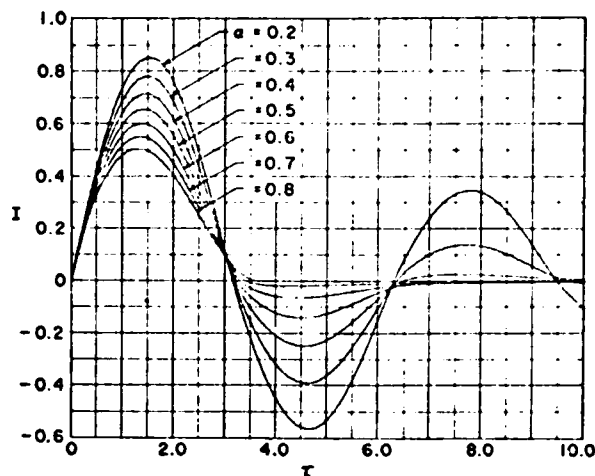

Fig. 8. Normalized energy for $\alpha = 0.2$ to 0.8.

Fig. 6. Normalized power for $\alpha = 0.8$ to 2.0.
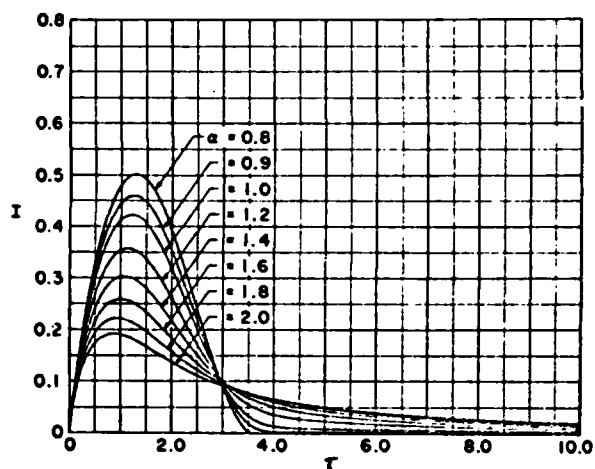

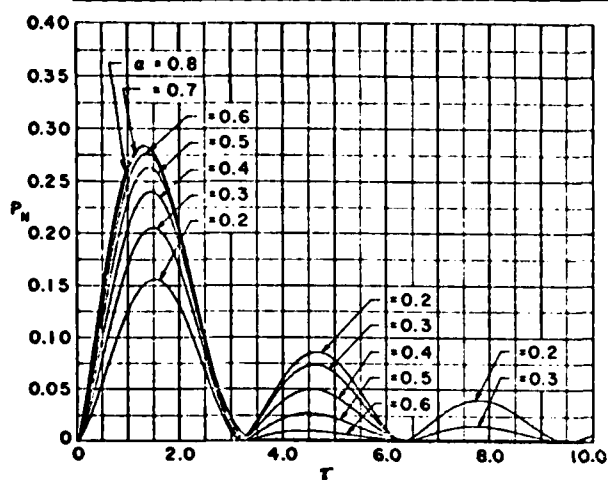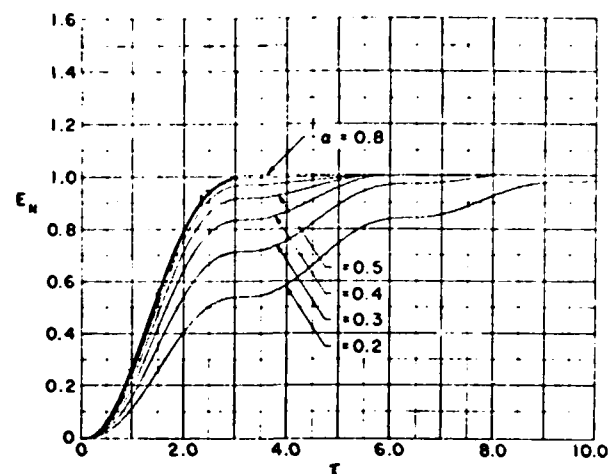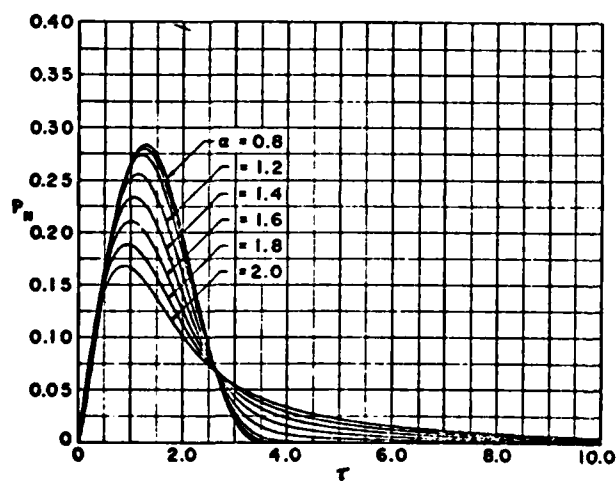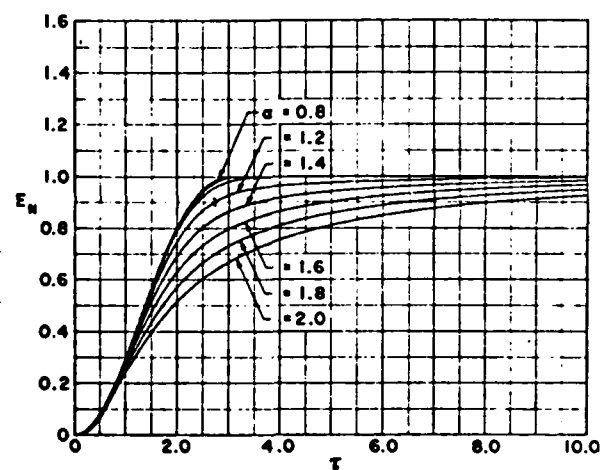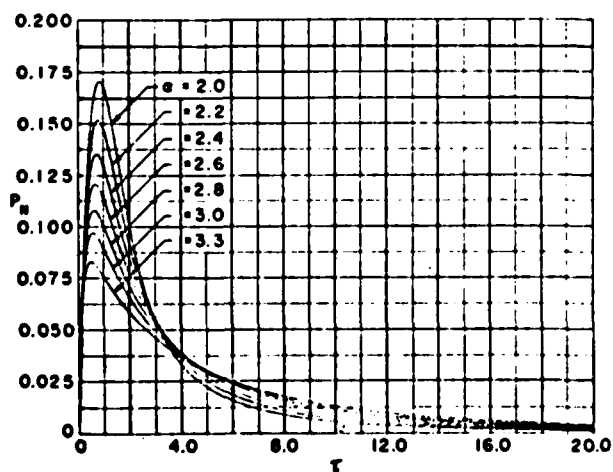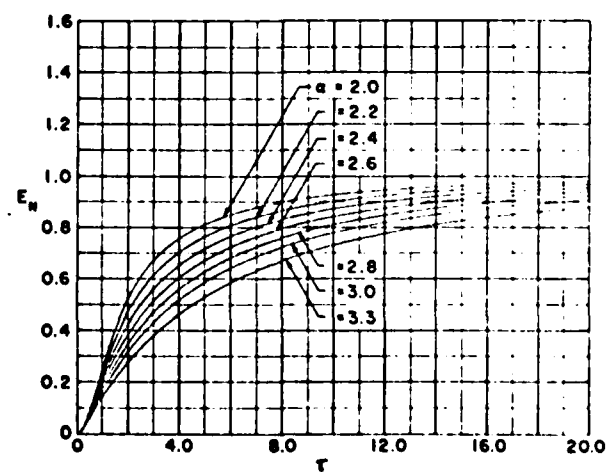Fig. 9. Normalized energy for $\alpha = 0.8$ to 2.0.

Fig. 7. Normalized power for $\alpha = 2.0$ to 3.3.

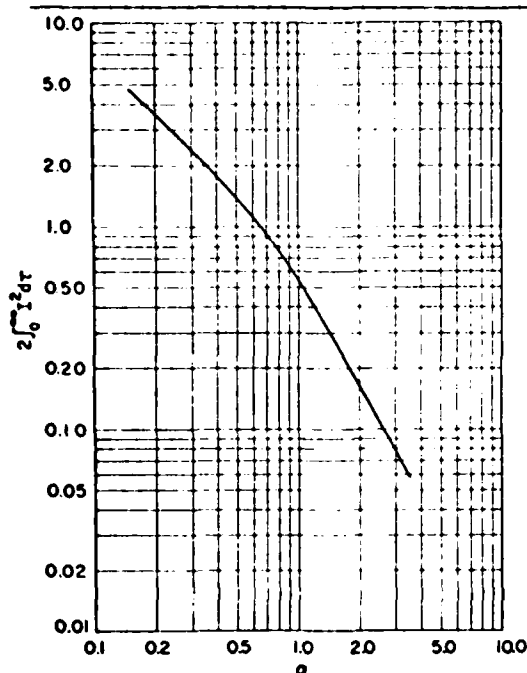Fig. 10. Normalized energy for $\alpha = 2.0$ to 3.3.

Fig. 11. The integral $2 \int_0^\infty I^2 \, d\tau$ as a function of α for estimating linear loss.

with the same sign convention for $|I_a|^{1/2}$ as before. The energy dissipated by this linear resistive loss is $E_r = r \int_0^\infty i_a^2 \, dt$. This energy normalized to E_0 is

$$E_{rN} = \frac{E_r}{E_0} = \frac{2r}{Z_0} \int_0^\infty I_a^2 \, d\tau. \qquad (13)$$

The integral $2 \int_0^\infty I^2 \, d\tau$, where the solutions of (6) have been used for I_a, is plotted as a function of α in Fig. 11. With this data an estimate may be made of the energy lost in the driving circuit when the losses are relatively small. The accuracy of this estimate improves when $(r/Z_0)I_{max}^{1/2}$ becomes small compared to α. The effect of r on the previously determined pulse shape can be easily seen as follows. If the term $(r/Z_0)I_{max}^{1/2}$ is small compared to α, a solution to (12) can be represented as a solution to (6), where α increases slightly as the current increases from $I = 0$ to $I = I_{max}$. This increase in any well-designed circuit is small, as can be shown by a simple numerical example. Suppose 3000 joules are to be discharged into a 1-cm diameter, 15-cm long xenon flashlamp. It is desired to have a critically damped pulse of 600 μs total duration. We then have: $E_0 = 3000$ joules, $T = 200$ μs, $\alpha = 0.75$, $K_0 \sim 25$ ohms-amps$^{1/2}$. Considering a lossless circuit, (4) and (8) provide $C = 580$ μF, $L = 69$ μH, $Z_0 = 0.345$ ohm. From (13) and Fig. 11 we note that a 0.01-ohm circuit loss will dissipate approximately 10 percent of the total energy. I_{max} from Fig. 2 for $\alpha = 0.75$ is approximately 0.53. Hence, $(r/Z_0)I_{max}^{1/2} \approx 0.09$. This represents a relatively small correction to α even at the peak current. It is, therefore, obvious that in any well-designed circuit the pulse shape will deviate little from the case where the flashlamp is

the only lossy element. It is for this reason that (12) was solved in the one parameter approximation of (6) rather than to have made a two-parameter solution requiring both α and r/Z_0.

Deviations from (1): the V-I characteristic of the xenon flashlamp which was represented in (1) neglects the two major lamp phenomena—hysteresis in the V-I characteristic, and the period during arc formation.

For any pulse length, there is always a small amount of hysteresis in the V-I characteristic, although it is not a problem for pulse durations from 150 μs to 4 ms. It does, however, become noticeable for long pulses (>5 ms), as the arc tends to remove material from electrodes and walls, thus producing different arc characteristics. Hysteresis thus encountered during long pulses produces 10 to 20 percent deviation from (1), though this is not usually sufficient to necessitate circuit redesign.

Hysteresis is a problem for short pulses during which a major portion of the pulse time is spent in the transition of the discharge from a small filament or streamer to an arc that fills the entire discharge volume available. For small lamps (diameter of discharge Column $d = 1$-5 mm) this time is of the order of 5 to 30 μs. For larger lamps (d of 10 to 20 mm) this might be as long as 50 to 125 μs. For total pulse widths comparable to these numbers, the above analysis serves only as a good starting point for design.

During the period of arc formation, either or both of the arc inductance $L_a(t)$ and its time derivative $L_a'(t)$ become important. (We assume $L_a(t) = L_a$ at $t = 0$ and $L_a(t) = 0$ when arc has reached the walls of tube.) If (3) is rewritten to show its dependence on these terms, we have

$$L \frac{di}{dt} + \frac{d(L_a(t)i)}{dt} \pm K_0 |i|^{1/2} + \frac{1}{C} \int_0^t i \, dt = V_0,$$

which can be expanded as

$$[L + L_a(t)] \frac{di}{dt} \pm \left[K_0 + |i|^{1/2} \frac{dL_a(t)}{dt} \right] |i|^{1/2}$$
$$+ \frac{1}{C} \int_0^t i \, dt = V_0. \qquad (14)$$

In short pulse systems, where the total discharge circuit inductance is kept as small as possible, the inductance of the arc is important, and is usually included as the value of the full-sized arc. However, initially it is larger due to the extremely small filament size. During the growth of the arc $dL_a(t)/dt$ is a negative number. At high current, therefore, the term $|i|^{1/2} dL_a(t)/dt$ can be quite significant. Indeed, it is quite usual in high power microsecond pulse systems to observe a negative voltage drop across the lamp during the first portion of the pulse. (A positive voltage drop being the IR drop with respect to current direction.) The measure of damping of (3) is $\alpha = K_0/(V_0 Z_0)^{1/2}$. We note that for (13) during arc formation $Z > Z_0$ and also K can be $<K_0$. Both of these

effects tend to produce a pulse that is more underdamped than would be expected. The foregoing is, of course, a rather naïve indication of short pulse behavior, as among other problems, it is not necessarily expected that the arc will follow (1) until it is confined by the discharge chamber. Experimental results do, however, indicate that the initial portion of a short pulse, corresponding to arc growth, has an effective α less than would be calculated for the static model.

A design procedure for flashlamp circuits has been presented here, which allows optimum matching of a flashlamp to a single mesh LC circuit. It is useful for pulse durations from 30 μs to >10 ms for small lamps and 100 μs to >10 ms for large lamps. Because the lamp current equation is linear in time, even though it is nonlinear in current, it is possible to give explicit design equations. With them, for a given lamp type, energy input, pulse duration and shape, the capacitance, inductance and operating voltage are easily determined. This procedure has been used to provide circuit designs for many types of xenon flashlamps in this laboratory and has been found accurate and useful.

Appendix B-4

RESISTIVE LOSS FACTOR IN
FLASHLAMP DRIVE CIRCUITS

1. The experimental resistive loss value was obtained by summing, in 5-μsec increments (from oscilloscope photographs of lamp voltage and current with time), the instantaneous energy dissipated in the flashlamp compared to the total stored flashlamp energy, 0.5 CV_0^2. The theoretical value for the resistive loss factor was 17.7% for a 240-mΩ series loss resistance; whereas, the experimental value was estimated at 5.5% (for a shape factor 0.70). The author attributed the major difference in these loss factors to the fact that the actual flashlamp resistance during the current pulse duration was appreciably larger than Z_0. This discussion establishes an experimental equivalent to Z_0 to improve the estimate of the resistive loss factor and shows, in this case, that the difference in theory and experiment lies strictly in the average flashlamp impedance figure.

2. To establish an average flashlamp resistance value for the total pump pulse duration, the energy input to the flashlamp in discrete time intervals (or increments) is required. This was done in Appendix B-3 for the shape factor 0.70. The average flashlamp resistance is defined by the equation

$$\bar{R} = \sum_i R_i E_i / \sum_i E_i \tag{1}$$

where i is the number of time increments used in the summation. The data of Appendixes B-2 and B-3 are used to provide R_i and E_i in the 5-μsec time increments used. Table B.4-1 provides the data for the summation. Then directly, the average flashlamp resistance becomes

$$\bar{R} = \sum_i R_i E_i /_i \Sigma E_i = 17.74(\Omega - J)/8.89(J) = 1.996\Omega \tag{2}$$

A 240-mΩ resistance would represent a loss, using $\bar{R}$, of (0.240)/ (1.996 + 0.240) $\cong$ 10.7%. The theory, using Z_0 = 1.333, predicts a loss of 17.7%. If the average flashlamp impedance of practice is compared to the Z_0 of theory, then the resistive loss factor estimates agree very well, for then (10.7%)(1.996/1.333) = 16.1%, which yields a loss factor difference of about 10%. Considering the width of the time increments used, the agreement is very good. Hence, the difference between theory and practice for estimating resistive loss is due strictly to the difference in the average flashlamp resistance $\bar{R}$ relative to the theoretical impedance Z_0. The actual resistive loss factor is then smaller than the theoretical value by the ratio $Z_0/\bar{R}$.

TABLE B.4-1. Plotting Data for $\overline{R}$.

t, μsec	R,Ω	E_i,J	$E_i R_i$,Ω-J
5.0	13.3	.154	2.05
10.0	4.4	.292	1.275
15.0	2.56	.445	1.14
20.0	1.76	.611	1.075
25.0	1.55	.775	1.20
30.0	1.53	.885	1.354
35.0	1.47	.925	1.36
40.0	1.47	.925	1.36
45.0	1.48	.860	1.274
50.0	1.47	.740	1.09
55.0	1.64	.655	1.175
60.0	1.75	.525	0.918
65.0	1.87	.385	0.72
70.0	2.0	.290	0.58
75.0	2.19	.195	0.427
80.0	2.94	.105	0.31
85.0	3.32	.07	0.232
90.0	4.86	.03	0.147
95.0	8.15	.007	0.056
			17.74

Appendix B.5

DELAYED FLASHLAMP TRIGGERING CONCEPT

1. International Lamp Corporation, Inc. (ILC), manufacturer of laser flashlamps, has conducted tests on delayed triggering of flashlamps which essentially involve discharging the main energy storage capacitor through the flashlamp only after the arc has formed more fully than if immediate capacitor discharge after flashlamp triggering were used. Basically, they measured fluorescence output improvements of 10-40%, depending upon the LC character of the discharge circuit and the gas used. By integrating the laser output and operating at one pulse per second, it was hoped that the delayed triggering concept for the flashlamp might be tested (in actual lasing tests rather than just fluorescence tests) without extensively exceeding the dissipation capability of the KN-4B krypton used in this circuitry.

2. The first tests with this delayed triggering technique showed an energy output degradation of about 40% or so just by placing the krypton in the discharge loop with negligible delay. Experimentally, it was found that the degradation in output energy was caused by three factors: (a) the $I_m t$ product for the flashlamp discharge, (b) the krypton arc drop, and (c) ohmic heating in the base leads. These factors degraded the output on the basis of the loss in available pump energy by 10.5, 19.5, and 6.5%, respectively. The measured arc drop at 200-amp peak current was 70 volts; EG&G data state that more typically 90 volts can be expected. The author's value was used in the above calculations. The ohmic heating was based on the EG&G figure of base lead resistance of 52 mΩ/in. Hence, the degradation in output energy by using the krypton could be corrected by including these losses by measuring arc drop voltage, peak current, flashlamp current pulse width, etc., but it was decided to forego these tests again. The availability of a positive charging supply makes SCRs usable and data can then be taken much more efficiencly.

3. The Wilmore power supply, employed in the prior testing, used a negative capacitor charging voltage. This complicated the delayed-triggering circuitry due to polarity problems of voltage switching. Hence, a high-current capability KN-4B krypton was initially used. The in-house lasers built had a positive charging system and so their breadboard electronics became available for these tests.

4. The author did not perform any further delayed-triggering tests, but advised a co-worker to do so. His results showed that little improvement in laser efficiency was possible using the delayed triggering concept.

NOTES:

1. ILC, Inc. has done considerable testing of fluorescent output efficiency for the delayed-triggering concept. Their data indicate strongly that if the LC is near optimum for normal (no delay) current discharge with respect to flashlamp triggering, little gain is made in efficiency using a delayed triggering approach.

2. The slight improvement observed using a delayed current pulse (and using $L = 30$ μH) is attributed to the fact that, for krypton-filled flashlamps, the optimum LC is larger than typically used experimentally. The difference in fluorescence output between optimum LC and experimentally used LC was about 10%.

3. *Delayed flashlamp triggering* is perhaps a misnomer. The flashlamp is triggered in the usual way, but the current pulse is delayed (perhaps 100 μsec or more) with respect to that triggering.

4. There are other system design considerations for the use of the delayed trigger (or "simmer mode") flashlamp operation. The improvements include (a) increased flashlamp life, (b) reduced EMI/RFI radiation, and (c) reduced coolant degradation. The major disadvantage of this mode of flashlamp operation is the added control and regulation electronics.

Appendix C
PUMP CAVITY DESIGN

Appendix C-1

THERMAL LENSING VERSUS THERMAL DISTORTION
IN THE LASER ROD

1. The PD manufacturer described theoretical calculations, which predict
the laser resonator raw-beam divergence, using geometric optics and the
classical resonator theory. The use of geometric optics is justified on
the basis that the resonator raw-beam divergence is appreciably larger
than the diffraction limited value; the classical resonator theory
assumes a homogeneous resonator. Several inconsistencies, however,
appeared to cloud the issue including:

    a. The theory shows no dependence on pulse-repetition rate, coupling
geometry, or energy input level unlike experimental results.

    b. Chromium sensitization of Nd:YAG appreciably degrades the resona-
tor output raw-beam divergence, whereas lutetium doping of Nd:YAG improves
it significantly in some cases.

The author felt there was a need to verify or disclaim the presence of
end-face thermal lensing. It is also apparent that thermal distortion
(optical path length variations) rather than thermal lensing (which
implies a simple curvature of an incident plane waveform) would not obey
the classical resonator theory and, at least qualitatively, satisfy the
inconsistencies presented above. This portion of Appendix C describes
the calculations of the thermal lensing equation and the results of the
experiments performed to test it. The test results indicate that further
experimental tests and analytical calculations would be beneficial to
understanding the pump cavity performance as it relates to the raw-beam
divergence.

2. Figure C.1-1 is the experimental arrangement for measuring the thermal
lensing effect. A collimated He-Ne laser is expanded in diameter to match
the laser rod diameter after passing through a 50-50 beamsplitter. If the
rod end face is flat, the beam diameter at distance t from the laser rod
end face is d_r. As the flashlamp is fired and if thermal lensing is present,
the beam spot diameter increases to diameter d_c due to a radius of curva-
ture R of the rod end face. This radius of curvature R can be related to
physical parameters of the experiment. Calculations on page 78 provide a
derivation of this thermal lensing equation and show that the radius of
curvature is given by
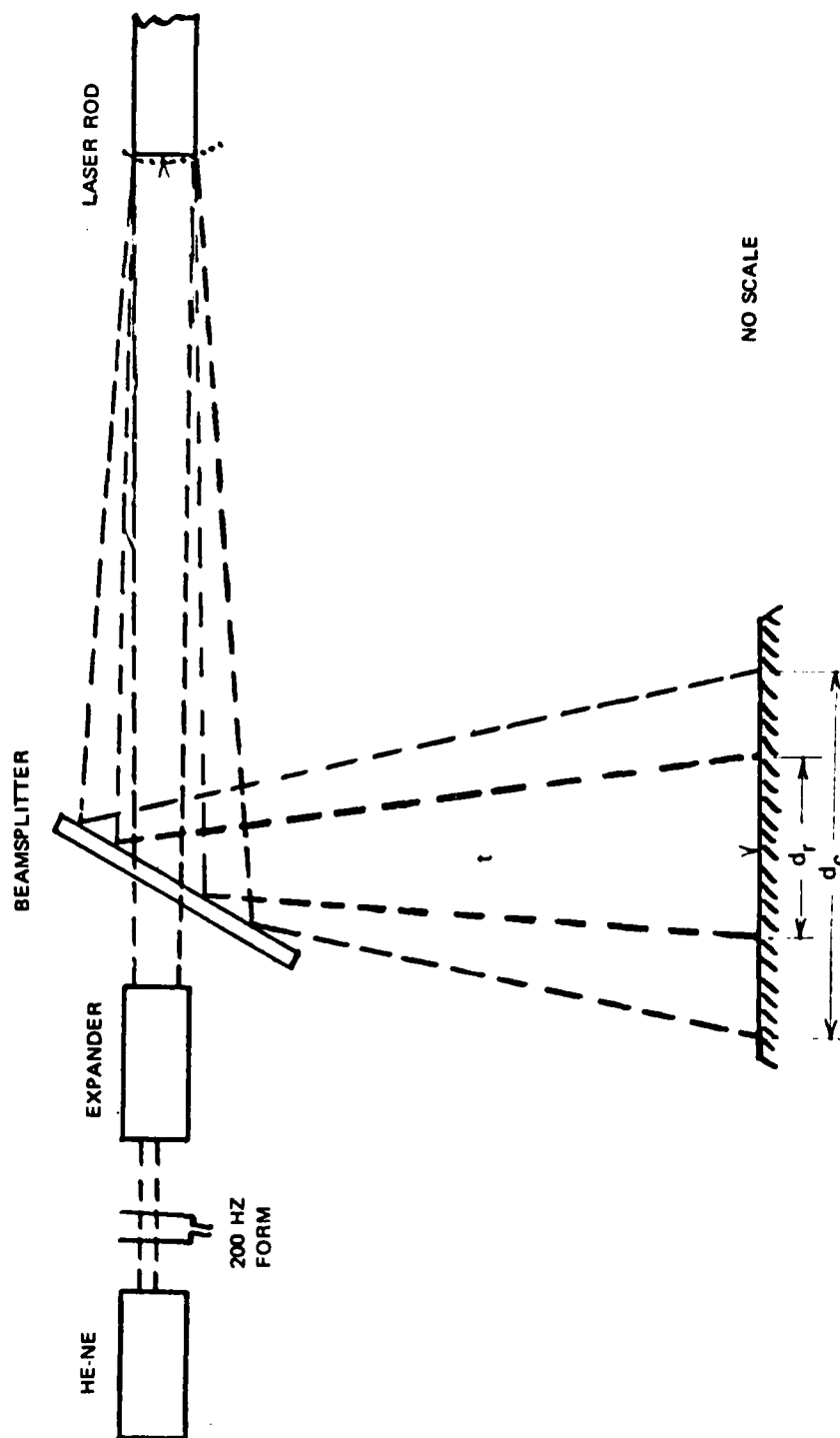
$$R = 2t[(d_c/d_r) - 1] \qquad\qquad (1)$$

FIG. C.1-1. Thermal Lensing Experiment Geometry.

The spot size diameter is not quite round and is a multiple image due to the thick beamsplitter. Also the estimate of spot diameter is difficult due to the flashlamp pulsing and relatively poor image quality. So a technique using a photodiode that views a 200-Hz modulated signal (which can be lock-in amplified) was used. This then would allow quantitative measurements of the thermal lensing effect as well.

3. By placing a photodiode of active diameter d_0 in the spot diameter (d_r and d_c), it would witness two intensities (for the flat and curved rod end face case) and create two different voltages at the lock-in amplifier as

$$V_\infty = k \, (d_0/d_r)^2$$

$$V_F = k \, (d_0/d_c)^2$$

where k is a constant of proportionality. Then directly, $V_\infty/V_F = (d_c/d_r)^2$. So then the radius of curvature R can be related to the photodiode output as

$$R = 2t/[(V_\infty/V_F)^{\frac{1}{2}} - 1] \tag{2}$$

This formula then provides a quantitative measurement for R in terms of a length t (here about 10 meters) and a voltage ratio from a lock-in amplifier. Page 80 begins the derivation of a general expression which relates thermal lensing contribution to the raw-beam divergence.

4. No thermal lensing was observed qualitatively or measured quantitatively in the tests made. The apparent spot size did not change at any time. However, by aligning the laser rod so that a reflection was present from both faces, it was apparent qualitatively that the contribution from the back face of the laser rod was changing with time and was equivalent to an optical path length distortion rather than a thermal lensing effect. (This was made more evident by shutting the cooling system off completely, firing the flashlamp for a few seconds, and then turning the cooling system back on.) Of course, the optical path length changes as the rod is heated due to dn/dT (among other things); i.e., the refractive index changes as the laser rod temperature increases. But, if the heating is uniform, no distortion in optical path should take place. The rate at which the laser rod was cooled back toward the ambient temperature was apparent from counting the interference fringes produced by reflection from the two faces of the laser rod (see Appendix A.8).

5. The complex, multimode structure within the laser resonator coupled with the optical path length inhomogeneity makes theoretical calculations of raw-beam divergence unreliable. However, on the basis of information in the open literature and some intuition, it can be said that:

78

a. Optical path length differences caused by inhomogeneities due to pumping or coolant flow or the radial rod temperature gradient cause more complex modes to oscillate, and hence an increase in raw-beam divergence should be expected.

b. Optical quality of the laser rod in passive tests using the Twyman-Green interferometer is quite different from the resonator quality during active operation.

c. The optical path distortion contribution to raw-beam divergence is more significant for use with flat mirrors than with curved mirrors.

d. Measurements at 1 pps and 10 pps indicate a beam divergence difference of about 30%, and the contribution of optical distortion to raw-beam divergence is appreciable.

e. The heat generation within the laser rod is mostly due to the radiationless transitions which occur in a very short time after the flashlamp creates that excited atom or ion. As a result, no significant heat redistribution occurs within the laser rod prior to Q-switching, and the pumping uniformity establishes the heat distribution generated per pulse by the flashlamp at low repetition rates.

f. The wavefront distortion produced by the flashlamp pulse itself is negligible compared to the long-term thermal effects of the pump cavity environs at high repetition rates.

g. All components in the pump cavity and its design in general need to be studied further to understand the effects of this distortion.

The contribution of the coolant (its flow pattern and physical properties), the thermal energy that the rod must reradiate for Xe versus Kr, the coupling shape, the pump uniformity within the rod, and so on, are all of interest in this interpretation.

6. Neglecting the contribution due to stress and pump nonuniformity to fringe count, a formula can be quickly derived to relate a thermal gradient in the laser rod to a fringe count across the cross sectional area of the rod. The more fringes there are over the rod face or cross section of the resonator, the more complex the mode structure which can oscillate. The higher order modes of the oscillator are made to contribute more to the resultant raw-beam divergence. This formula, derived beginning on page 84, is

$$\Delta T_R = \lambda (N_e - N_c)/2s [n\alpha + (dn/dT)] \tag{3}$$

and substituting values:

$$dn/dT = 7.3 \ (10)^{-6}/°C$$

$$\alpha = 6.9 \ (10)^{-6}/°C$$

$$n = 1.83$$

$$s = 76.2 \ mm$$

$$\lambda = 6.24 \ (10)^{-4} \ mm$$

yields

$$\Delta T_R = \Delta N/5 \ (°C)$$

Hence a temperature difference of 1°C within the laser rod, from center to edge, causes an optical path length difference of 5 wavelengths at 6328Å (or about 3 wavelengths at 1.06μ, neglecting anomalous dispersion).

NOTE:

These calculations by Eq. 3 are shown to be in error due to the fact that the laser rod is under negative stress (compression) and so is not capable of freely changing its length from center-relative-to-edge due to a radial thermal gradient (see Appendixes C.5 and E.4).

Derivation of Thermal Lensing Equation

From the lens equation with a flat-rod end face, it follows that

$$\frac{1}{S_\infty} + \frac{1}{S_\infty{'}} = \frac{2}{V_\infty} = 0 \tag{1-1}$$

and for the curved end face case, due to flashlamp pumping, it becomes

$$\frac{1}{S_c} + \frac{1}{S_c{'}} = \frac{2}{R} \tag{1-2}$$

but

$$S_c \equiv S_\infty$$

and

$$S_c{'} = \frac{RS_\infty}{2S_\infty - R} \tag{1-3}$$

Assume that the beam spreads at the laser rod, upon reflection, are θ_∞ and θ_c for the two cases. Then for small θ,

$$\theta_\infty = hr/S_\infty$$

$$\theta_c = hr/S_{c'} \tag{1-4}$$

and so

$$\frac{\theta_\infty}{\theta_c} = \frac{S_{c'}}{S_\infty}$$

and by proportionality,

$$(S_{\infty'} + t)\theta_\infty = d_r$$

$$(S_{c'} + t)\theta_c = d_c \tag{1-5}$$

and taking the ratio

$$\left(\frac{S_\infty + t}{S_{c'} + t}\right)\frac{S_{c'}}{S_\infty} = \frac{d_r}{d_c} \tag{1-6}$$

The laser beam (6328Å) is very well collimated so that $S_\infty \gg R, t$ which yields that

$$S_{c'} = \frac{R}{2} \tag{1-7}$$

and so

$$\left(\frac{1 + \frac{t}{S_\infty}}{S_{c'} + t}\right) S_{c'} = \frac{d_r}{d_c} = \frac{S_{c'}}{S_{c'} + t} \tag{1-8}$$

then

$$\frac{d_r}{d_c} = \frac{R/2}{(R/2) + t}$$

and

$$\left[\left(\frac{R}{2} \right) + t \right] d_r = \frac{Rd_c}{2}$$

$$R \left(d_c - d_r \right) = 2td_r$$

and finally

$$R = 2t \Big/ \left[\left(\frac{dc}{dr} \right) - 1 \right] \tag{1-9}$$

which relates the radius of curvature of the laser rod end face to measurable parameters and dimensions.

Lensing Contribution to Raw-Beam Divergence

The results of a study by the PD manufacturers claim that

$$\theta_{raw} = \theta_1 + \frac{K_2}{\left(F_{eq} \right)^{\frac{1}{2}}} \tag{2-1}$$

where K_2 and θ_1 are functions of resonator design and λ, and where

$$F_{eq} = \frac{1}{\frac{1}{2F_1} + \frac{1}{2F_2} + \sum_{i=1}^{N} \frac{1}{F_i}} \tag{2-2}$$

Then let

$$\sum_{i=1}^{N} \frac{1}{F_i} = \frac{2}{R_1} + \frac{2}{R_2} = \frac{2}{R} \tag{2-3}$$

where R_1 and R_2 are the radii of curvatures of the two end faces. If the curvatures are equal, then

$$R_1 = R_2 = 2R$$

Interest is in the change in θ_{raw} as a result of a change in R, assuming this theory is correct. So then

$$\frac{d\theta_{raw}}{dR} = \frac{d\theta_{raw}}{dF_{eq}} = \frac{dF_{eq}}{dR}$$

$$= \frac{K_2}{2} \frac{1}{\left(F_{eq}\right)^{3/2}} \frac{1}{\left(\frac{1}{F} + \frac{2}{R}\right)^2} \frac{2}{R^2}$$

$$= K_2 \frac{1}{R^2\left(\frac{1}{F} + \frac{2}{R}\right)^{1/2}} = \frac{0.065}{R^2\left(\frac{1}{F} + \frac{2}{R}\right)^{1/2}} \qquad (2\text{-}4)$$

using $K_2 = D/\sqrt{L} \approx 0.25/\sqrt{15} = 0.065$.

For convenience, let

$$R_1 = R_2 = 2R$$

then

$$2dR_2 = dR$$

and

$$d\theta_{raw} = \frac{0.065 \ dR/2}{\left(\frac{R}{2}\right)^2\left(\frac{1}{F} + \frac{4}{R}\right)^{1/2}} = \frac{0.130 \ dR}{R^2\left(\frac{1}{F} + \frac{4}{R}\right)^{1/2}} \qquad (2\text{-}5)$$

where

$$R = 2t \Bigg/ \left[\left(\frac{V_\infty}{V_F}\right)^{1/2} - 1\right] \qquad (2\text{-}6)$$

as decided earlier. If one plots the lock-in amplifier voltage as the ordinate and time as the abscissa on an XY recorder, one expects for real thermal lensing the following dependence:
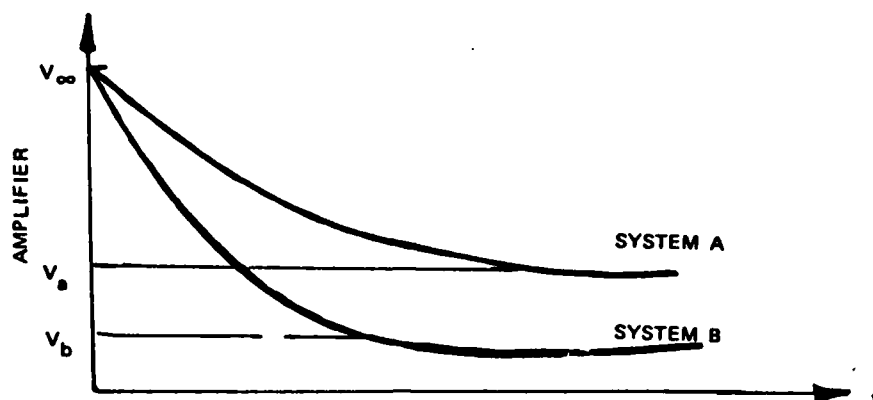
Two different systems A and B could yield different lensing magnitudes; e.g., if Kr and Xe flashlamps are used. So the two values of R become

$$R_a = 2t \left/ \left[\left(\frac{V_\infty}{V_a} \right)^{\frac{1}{2}} - 1 \right] \right.$$

$$R_b = 2t \left/ \left[\left(\frac{V_\infty}{V_b} \right)^{\frac{1}{2}} - 1 \right] \right. \qquad (2\text{-}7)$$

and using $\dfrac{R_a + R_b}{2} = R$, it follows that the resultant change in raw-beam divergence is

$$d\theta_{raw} = \frac{0.130 \left(R_a - R_b \right)}{\left(\dfrac{R_a + R_b}{2} \right)^2 \left(\dfrac{1}{F} + \dfrac{F}{R_a + R_b} \right)^{\frac{1}{2}}} \qquad (2\text{-}8)$$

so a change in beam divergence can be related to the pump cavity components selected. Actually, one still needs R_a, R_b in terms of voltages in this equation. So proceeding,

$$R_a - R_b = \frac{2t}{\left(\dfrac{V_\infty}{V_a} \right)^{\frac{1}{2}} - 1} - \frac{2t}{\left(\dfrac{V_\infty}{V_b} \right)^{\frac{1}{2}} - 1}$$

84

$$= 2t \left\{ \frac{\left(\frac{V_\infty}{V_b}\right)^{\frac{1}{2}} - 1 - \left(\frac{V_\infty}{V_{a\prime}}\right)^{\frac{1}{2}} + 1}{\left[\left(\frac{V_\infty}{V_a}\right)^{\frac{1}{2}} - 1\right]\left[\left(\frac{V_\infty}{V_b}\right)^{\frac{1}{2}} - 1\right]} \right\}$$

$$= \frac{2t}{\left(V_\infty\right)^{\frac{1}{2}}} \left\{ \frac{\left(\frac{1}{V_b}\right)^{\frac{1}{2}} - \left(\frac{1}{V_a}\right)^{\frac{1}{2}}}{\left[\left(\frac{1}{V_a}\right)^{\frac{1}{2}} - \left(\frac{1}{V_\infty}\right)^{\frac{1}{2}}\right]\left[\left(\frac{1}{V_b}\right)^{\frac{1}{2}} - \left(\frac{1}{V_\infty}\right)^{\frac{1}{2}}\right]} \right\} \qquad (2\text{-}9)$$

and also

$$R_a + R_b = 2t \left[\frac{1}{\left(\frac{V_\infty}{V_a}\right)^{\frac{1}{2}} - 1} + \frac{1}{\left(\frac{V_\infty}{V_b}\right)^{\frac{1}{2}} - 1} \right]$$

$$= \left\{ \frac{\left(\frac{V_\infty}{V_b}\right)^{\frac{1}{2}} + \left(\frac{V_\infty}{V_a}\right)^{\frac{1}{2}} - 2}{\left[\left(\frac{V_\infty}{V_a}\right)^{\frac{1}{2}} - 1\right]\left[\left(\frac{V_\infty}{V_b}\right)^{\frac{1}{2}} - 1\right]} \right\}$$

and finally,

$$R_a + R_b = \frac{2t}{\left(V_\infty\right)^{\frac{1}{2}}} \left\{ \frac{\left(\frac{1}{V_b}\right)^{\frac{1}{2}} + \left(\frac{1}{V_a}\right)^{\frac{1}{2}} - \left(\frac{2}{V_\infty}\right)^{\frac{1}{2}}}{\left[\left(\frac{1}{V_a}\right)^{\frac{1}{2}} - \left(\frac{1}{V_\infty}\right)^{\frac{1}{2}}\right]\left[\left(\frac{1}{V_b}\right)^{\frac{1}{2}} - \left(\frac{1}{V_\infty}\right)^{\frac{1}{2}}\right]} \right\} \qquad (2\text{-}10)$$
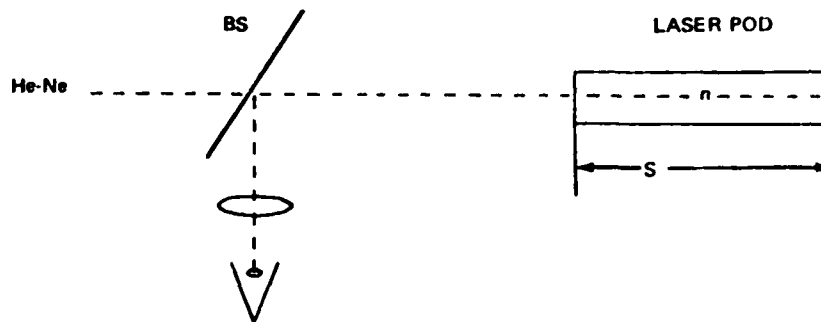
which indicates that one must calculate $(V_i)^{-\frac{1}{2}}$ to get the dependence on the radii of curvature. Then Eq. 2-9 and 2-10 can be used in Eq. 2-8 to get the contribution to beam divergence directly. The value of F is established by the end mirror curvature of the resonator reflectors.

Fringe Counting and Thermal Gradient

The optical path length difference between a projection from the front and back surface of the laser rod is

$$P = 2nS \tag{3-1}$$

and so with temperature

$$\frac{\Delta P}{\Delta T} = 2n \frac{dS}{dT} + 2S \frac{dn}{dT}$$

$$= 2S \left[n\alpha + \left(\frac{dn}{dT}\right) \right] \tag{3-2}$$

where the linear expansion coefficient is such that $K = \frac{1}{S} \frac{dS}{dT}$.

Therefore, we can say

$$\Delta T = \frac{\Delta P}{2S \left[n\alpha + (dn/dT) \right]} \tag{3-3}$$

Since the interest is in the fringe count at the center relative to that at the edge of the rod, then

$$\Delta T_R = \Delta T_e - \Delta T_c \tag{3-4}$$

$$\Delta T_R = \frac{N_c \lambda}{2S \left[n\alpha + \left(\frac{dn}{dT}\right) \right]} - \frac{N_c \lambda}{2S \left[n\alpha + \left(\frac{dn}{dT}\right) \right]} \tag{3-5}$$

86

and finally

$$\Delta T_R = \frac{(N_e - N_c)\lambda}{2S \left[n'\iota + \left(\frac{dn}{dT} \right) \right]}$$

(3-6)

The distortion of an incident plane wave is then available in terms of wavelengths of the probe beam (here 6328Å) wavelength.

NOTES:

1. The actual cause of the increased beam divergence was later established as due to a radial thermal gradient as described in Appendixes C-5 and E-4. This test did serve to show that negligible thermal lensing of the laser rod end faces occurs.

2. This appendix made evident the need for a new equation describing the raw-beam divergence from the T-beam-type resonator. It is derived semiempirically in Appendix E-4.

3. The equations derived for the lensing contribution of the rod end faces to raw-beam divergence are applicable to high power CW laser systems.

Appendix C-2

INTERFEROMETRIC STUDIES

1. The present pump cavity design study was initiated by the author after the presence of thermal distortion was shown by analysis and experiment. While the investigation of this thermal distortion is underway, a concurrent and related evaluation of resonator output characteristics is also being performed. These pump cavity studies have included output-beam uniformity studies and raw-beam divergence measurements, with the variables being pump cavity shape, flashlamp type, end-reflector type, and resonator alignment accuracy. A criterion to determine the misalignment axes of the resonator was established by an examination of burn patterns on exposed Polaroid film. The effect of thermal distortion on raw-beam divergence with increased pulse-repetition rate using FC-104 coolant was established. Test results using a water coolant and an alternate coolant entrance port are also to be provided. Recommendations are also made on possible pump cavity modifications to correct its present thermal deficiencies.

2. The interferometric test apparatus is shown in Fig. C.2-1. Reflection of the single-mode helium-neon laser light from both surfaces of the laser rod produces interference fringes, where interference fringes were counted to determine the equilibrium operating temperature of the laser rod. Since the laser rod is not optically perfect, its specification to the manufacturer allows (perhaps) one fringe per linear inch when tested in a Twyman-Green interferometer. This allowable fringe count may be due to variations in the refractive index of the laser rod, or variations in length, or both, and the individual contributions are not distinguishable with the use of a single interferometer. These fringes represent a difference in optical path length of one wavelength between them (in two passes through the laser rod). If the laser rod, due to flashlamp pumping, is heated nonuniformly, the interference-fringe count over the laser rod diameter increases. If the *better* side of the laser rod happens to be oriented to that side of the laser rod which is of longer optical path length (again due to index of refraction gradients, or length differences, or both), the interference-fringe count will be larger than if the laser rod were rotated 180 deg. Therefore, the interference-fringe count observed due to thermal distortion may vary depending upon the laser rod orientation within the pump cavity as will be shown directly. Yet the net increase in thermal distortion remains unchanged as far as the effects on increased raw-beam divergence are concerned. All of the pump cavity design studies have been performed with a single laser rod. The raw-beam divergence at 1 pps relative to that at 10 pps depends upon the increase in the index of refraction gradient relative to that present when received from the manufacturer.
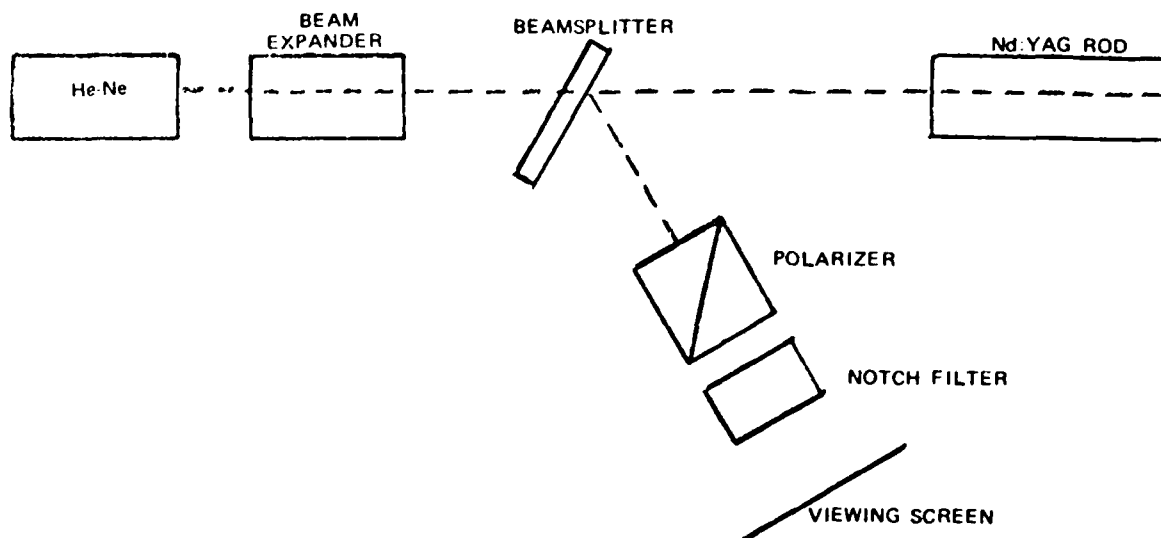
BEAM
EXPANDER

BEAMSPLITTER

Nd:YAG ROD

He-Ne

POLARIZER

NOTCH FILTER

VIEWING SCREEN

FIG. C.2-1.   Interferometric Test Apparatus.

Since, in the Twymann-Green interferometer, a length difference and an
index of refraction difference are optically equivalent, the absolute
magnitude of the index of refraction gradient is not predictable. Hence,
the data presented and the results derived using interference-fringe-
count data should be considered statistical in nature in that other rods,
if tested, may likely yield somewhat different results.

3.   Before describing the interference fringe behavior at both 1 and
10 pps, the concept of thermal focusing should be mentioned. A length
difference caused by thermal gradients essentially misaligns the resona-
tor. This is evident (for instance) by operating a resonator (which has
thermal distortion) at a 1-pps rate after it has been tuned and opti-
mized for operation at the 10-pps rate. Suppose now that two parallel
optical paths through the laser rod, separated by a distance $\underline{a}$, have an
optical path length difference, in one pass, of one wavelength. Then it
can be shown by Huygen's principle that this optical path length differ-
ence creates a focusing effect between these paths equivalent to a lens
of focal length f, where $f = a^2/2\lambda$. Hence, one could alternately view
thermal misalignment as a thermal focusing of sorts in one plane, and
then technically it can be said that thermal lensing occurs in the
laser rod. To get the equivalent of a lens effect with focal length f;
i.e., focusing in two normal planes due to thermal distortion in the
resonator, the optical path length of a path P would need (1) to be less
than that of a second path P' by one wavelength, (2) to be separated
from it radially by a distance $\underline{a}$, and (3) to be rotationally symmetric
about the path P'. This means that to the observer, circular inter-
ference patterns would need to be seen, these rings being separated by

89

distance a laterally and distance λ longitudinally. As an example, suppose a dark spot existed at the center of the laser rod and a dark interference ring is seen near its edge. Then this produces a lens effect with an equivalent focal length (at the probe wavelength) of about 8 meters and represents a true thermal lensing in the laser resonator. The net result in this case would be that the resonator raw-beam divergence would behave as if a flat end mirror were replaced with a curved end mirror. Circular interference fringes were not observed in the tests performed by the author but have been observed in both glass and ruby laser rods at very high input energies. The absence of circular interference fringes also indicates that the temperature distribution is not radially symmetric.

4. When the flashlamp is fired at 1 pps, the interference fringes are seen to *jump* instantaneously corresponding to the absorption of the flashlamp radiation by the laser rod. The interference fringes returned to their initial position before the next pulse occurred; i.e., the thermal relaxation process lasted less than 100 msec. The internal heating is caused by two mechanisms: (1) absorption by the host material, and (2) radiationless transitions within the dopant or impurity ion. The flashlamp pumping uniformity then determines how uniformly the absorbed energy is distributed within the laser rod. In turn, the pump uniformity determines the thermal distribution in the laser rod at the 1-pps rate since negligible thermal conduction occurs within the 100-μsec pump pulse duration. Hence, the optimum pump uniformity of the laser rod should provide the minimum raw-beam divergence at 1 pps for a given laser rod. Furthermore, the amount of energy absorbed by the laser rod is predictable on the basis of the magnitude of the interference fringe jump. The largest inherent inaccuracy in this calculation is the estimate of the amount of the interference fringe shift due to this absorption of flashlamp radiation. The percentage of energy absorbed ($\%E_{abs}$) by the laser rod is equal to the ratio of that actually absorbed in the laser rod as compared with that stored in the energy storage capacitor so that

$$\%E_{abs} = C_p \, \rho \, V \, \Delta T / 0.5 \, CV^2$$

$$= C_p \, \rho \, V / 0.5 \, CV^2 \, N\lambda/2\ell[n\alpha + (dn/dT)]$$

$$= C_p \, \rho \, V \, N \, \lambda/CV^2\ell[n\alpha + (dn/dT)] \tag{1}$$

where

C_p = specific heat of YAG (0.586 J/g-°C)

ρ = density of YAG (4.55 g/cm³)

V = volume of laser rod (2.42 cm³)

$0.5\ CV^2$ = energy input per pulse to the flashlamp (8.5 J)

N = interference fringe shift magnitude (1/4 of one fringe)

λ = the probe wavelength (6328Å)

ℓ = laser rod length (7.63 cm)

n = index of refraction of YAG (1.83)

α = linear expansion coefficient for YAG (6.9 x 10^{-6}°C^{-1})

dn/dT = thermal index coefficient for YAG (7.3 x 10^{-6}°C^{-1})

and substituting these figures into Formula 1 yields %E_{abs} = 4% and an increase in laser rod temperature of only 0.05°C per pulse. A recent Korad publication describes the thermal analysis of a CW pumped Nd:YAG laser rod. The author concludes that the fraction of electrical input power into the lamps (krypton-filled lamps in a double elliptical config- uration) which is absorbed by the laser is only 7.5%. He also states that E. Matovich of Autonetics has calculated that a 6-mm Nd:YAG laser rod absorbs only 4.5% of the total radiation of a blackbody radiator at a temperature of 3200°K. The result above is in reasonable agreement with these findings.

5. At 10 pps, the interference fringes travel in a well-defined direc- tion. It can be shown that, if the laser rod is heated, the interference fringes move in the direction corresponding to the shortest optical path length. Since α and dn/dT are both positive this also means that the interference fringes travel toward the coolest part (or side) of the laser rod. Because of the orientation of the laser rod in the pump cavity relative to the imposed thermal gradient and the heat conduction process itself, the interference fringe curvature may vary as well (as does the fringe count as described earlier). The fringe count data as a function of input energy are shown in Fig. C.2-2 (after subtracting what the author calls the residual fringe count or the *as-received* fringe count). Since the laser rod was reoriented in rotation between many of the individual test runs, the random nature of the residual fringe count orientation to that produced by the thermal gradient is readily evident. Of particular
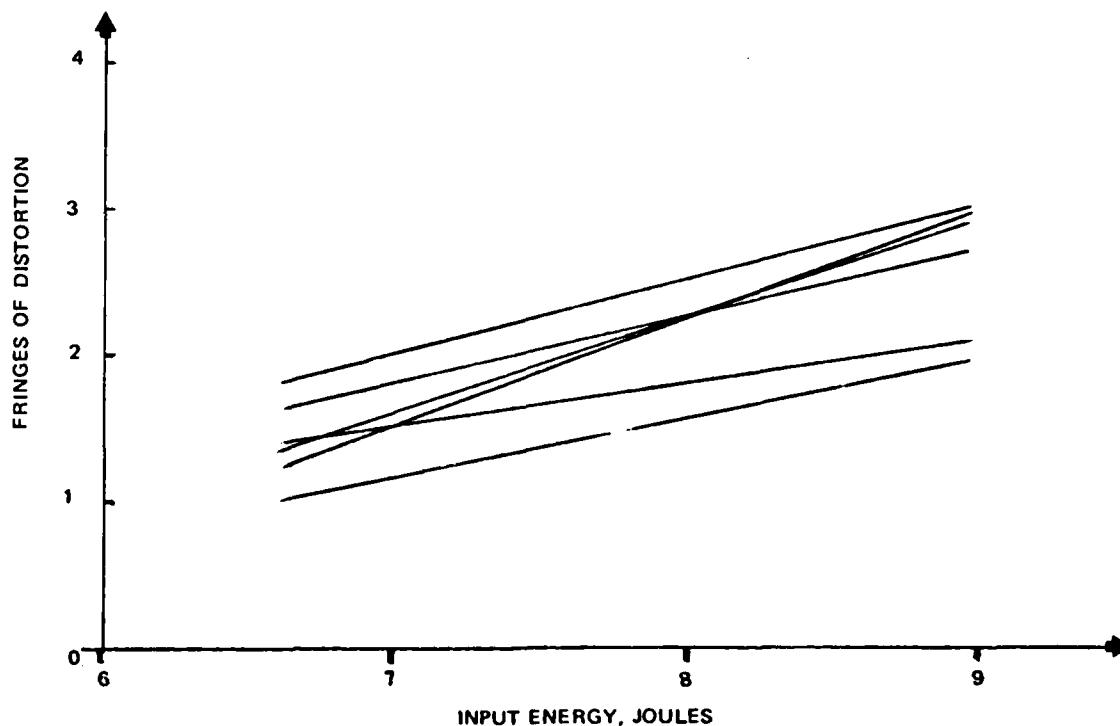
FIG. C.2-2. Fringe Count Versus Input Energy. Thermal distortion
fringe-count data summary as measured at 6328Å less the residual
fringe-count figure.

interest is the slope of this curve. If an interference fringe count
gradient with increased input energy is obtained, an interference fringe
count from a Twyman-Green interferometer should be related to a raw-beam
divergence increase as well. One precaution is first necessary, however.
The optical path length (P_{TG}) in a Twyman-Green interferometer is given
by $P_{TG} = 2(n-1)\ell$, where ℓ is the length of the laser rod, since the
optical path length through the laser rod and back is compared to a
separate air path length. (An increase in laser rod length due to
heating represents a decrease in the air space length in this inter-
ferometer, and hence the (n-1) dependence appears.) Recall that the
optical path length of the laser rod interferometer is just $P_R = 2n\ell$.
Now suppose each interferometer changes in length by $d\ell$ and n remains
constant. Then let $d\ell$ be one wavelength and n = 1.83 and then it follows
that $dP_R = 2dP_{TG}$. If the index of refraction rather than the length had
changed, the optical path length change in each interferometer would be
the same. Let the change in $d\ell$ be assumed since it represents the worse
case difference in the interference fringe count. In this case, one
fringe in a Twyman-Green interferometer is equivalent to two fringes

in the laser rod interferometer. The slope of the curve in Fig. C.2-2, related to a Twyman-Green interferometer fringe count, would then be 0.3 fringes per 2.5 J of input energy. The raw-beam divergence increase with an increase in input energy was (for this same laser rod) 0.22 mrad/J. Hence, for an increase in input energy per pulse to the flashlamp, a change of $\lambda/10$ in interference fringe count corresponds to an increase in raw-beam divergence of about 0.2 mrad. At a fixed input energy level, using the average fringe count data of Fig. C.2-2 and prior experimental results, the raw-beam divergence is expected to increase slightly less than 0.1 mrad/λ/10 change in thermal distortion magnitude. If this analogy could be carried to zero input energy, then an increase in residual fringe count by $\lambda/10$ would increase the raw-beam divergence expected by only about 0.075 mrad. The analogy also assumes that the contributions of length difference and index-of-refraction differences are in the same proportions as those present in the residual interference fringe count. If many laser rods were tested (as has been done with ruby laser rods), the wide variance in raw-beam divergence at low repetition rates would be evident. The author attributes this variance to differences in the relative magnitudes of dn and dℓ separately. Unfortunately the tests on ruby laser rods did not measure their relative magnitudes. The possibility of measuring each separately is possible using two interferometers—one of the laser rod and the other, the comparator, or Twyman-Green type. Note that if interference fringes are counted separately for each type, it can be said that

$$\Delta P_R = 2(n\Delta\ell + \ell\Delta n) = N\lambda \tag{2}$$

$$\Delta P_{TG} = 2[(n - 1)\Delta\ell + \ell\Delta n] = N'\lambda \tag{3}$$

and directly

$$\Delta\ell = (N - N')\lambda/2\ell \tag{4}$$

$$\Delta n = [nN' - (n - 1)N]\lambda/2\ell \tag{5}$$

This was not possible with the author's apparatus due to the instability of the Twyman-Green type of interferometer.

6. For most of the interferometric studies, the coolant entrance ports into the pump cavity were oriented perpendicular to the laser rod-flashlamp plane as shown in Fig. C.2-3. The coolant strikes the flashlamp envelope near the electrode (and traverses a short channel (of about 1 cm) before entering the electrode-less (and laser rod) portion of the pump cavity. The geometry for three pump cavity shapes and the end plate manifold is given in Fig. C.2-4. By examining the interference pattern obtained while firing the flashlamp at 10 pps (and by some raw-beam divergence measurements), it can be concluded that:

93
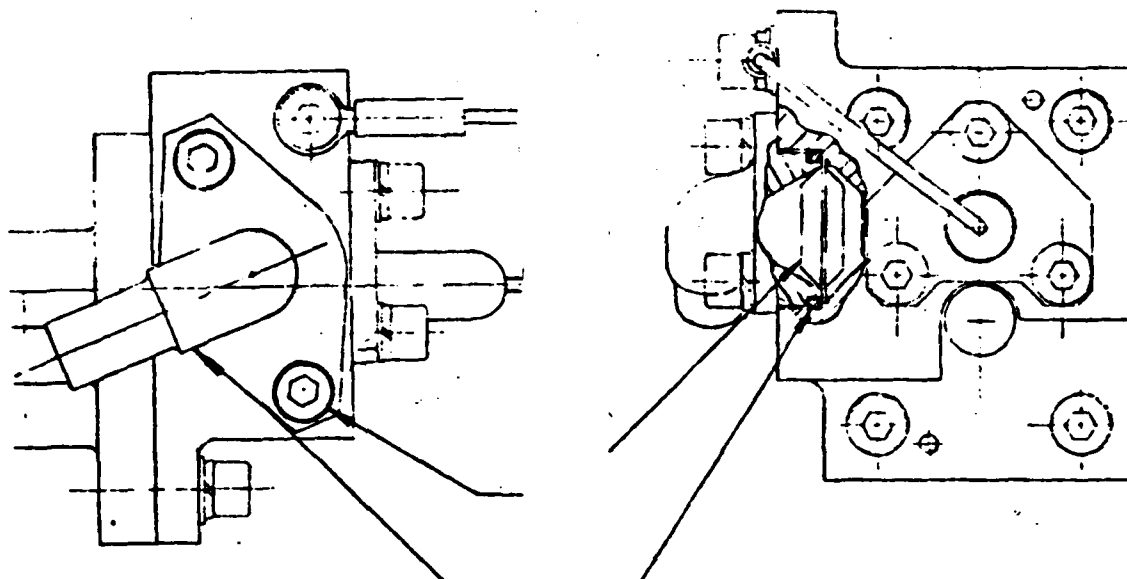
FIG. C.2-3. Coolant Entrance Port Geometry, Normal to Flashlamp-Rod Plane.

COOLANT FLOW DIRECTION
INTO ENTRANCE CHANNEL

0.75"

DIMENSIONS ARE
APPROXIMATE ONLY

ENTRANCE CHANNEL
CROSS SECTION COOLANT
FLOW IS OUTWARD

SUPERIMPOSED
COUPLING GEOMETRIES

LASER ROD

MANIFOLD

FLASHLAMP

CYLINDRICAL

"RACETRACK"

ELLIPTICAL
WITH INSERTS

FIG. C.2-4. Flashlamp-Laser Rod Coupling Geometries
(including end-plate manifold layouts).

a. The hottest portion of the laser rod is that indicated by the darkened region of the laser rod, as shown in Fig. C.2-4. This is due primarily to the inability of the coolant to provide adequate flow in this region.

b. Reversing the coolant flow from cathode to anode rather than from anode to cathode does not change the interference fringe pattern significantly, and the same raw-beam divergence results for either direction of flow. This indicates that the axial temperature gradient has a much smaller effect on thermal distortion than the thermal gradient normal to the coolant flow.

c. Coolant ports which enter the pump cavity parallel to the rod-flashlamp plane (Fig. C.2-5) do not significantly improve the raw-beam divergence from the resonator.
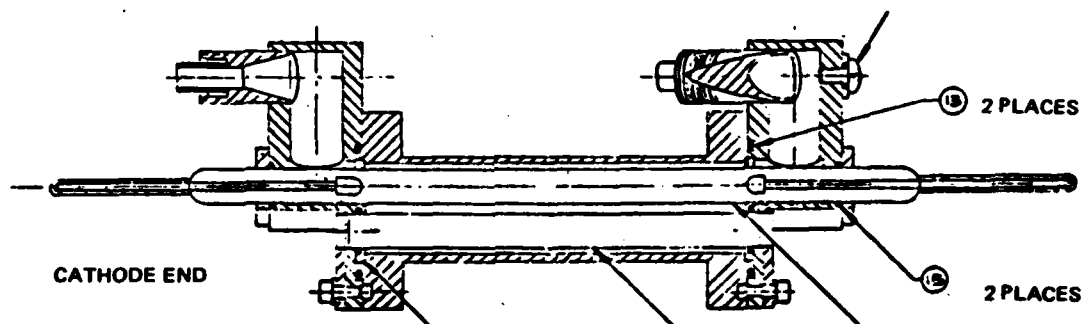
FIG. C.2-5. Coolant Entrance Port Geometry, Parallel to Flashlamp-Rod Plane.

d. At an input energy of 8.5 J, there is negligible thermal birefringence in the laser rod.
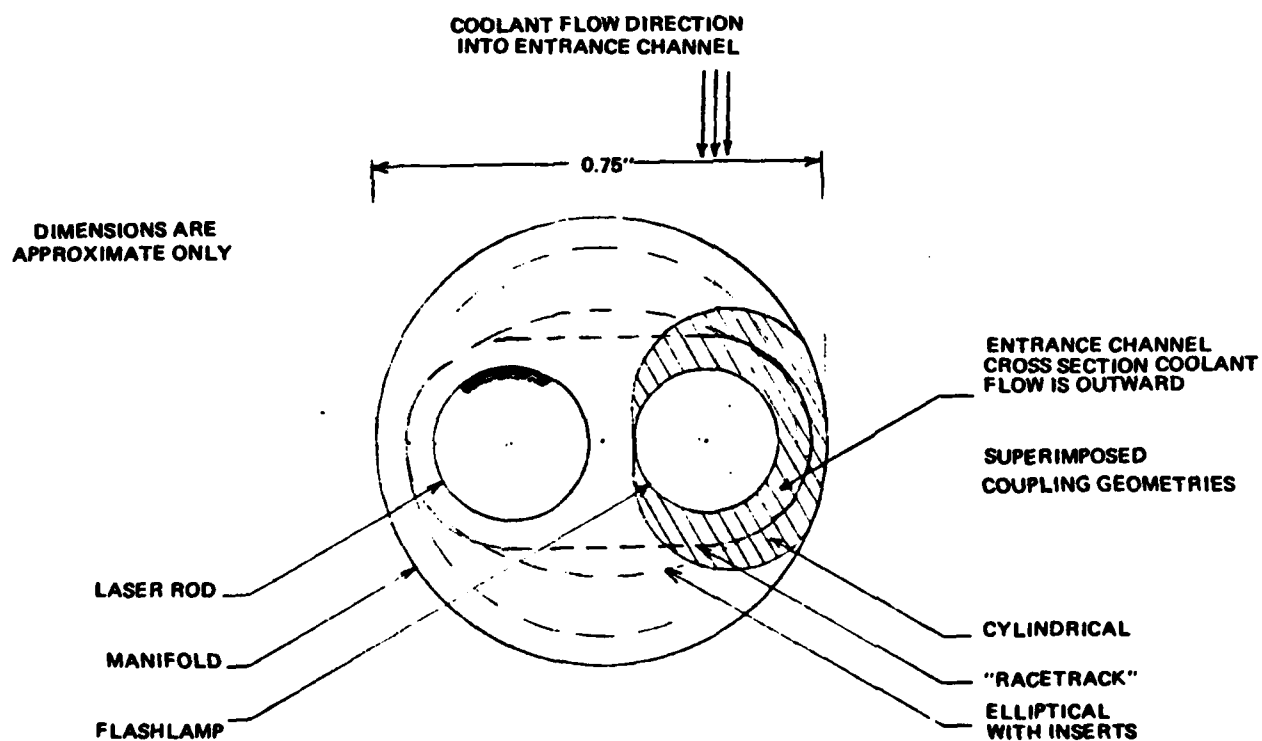
e. The flashlamp proximity to the laser rod does not appreciably affect the thermal distortion at the 10-pps rate in the present pump cavity design.

f. An optical wedge effect in the flashlamp-rod plane was evident, since the interference fringe travel direction was generally normal to that plane.

g. A diffuse reflecting surface on the pump cavity walls is not expected to improve the raw-beam divergence significantly at the 10-pps rate in the present pump cavity design.

h. With the use of doubly distilled water coolant, the resonator does not require significant realignment when the repetition rate is changed from 1 to 10 pps nor did the raw-beam divergence increase significantly by changing the repetition rate. Hence, the entrance port design is not critical with water or other high-thermal-conductivity coolant mixtures such as ethylene glycol/water.

i. The equilibrium operating temperature of the laser rod using water coolant is much less than that using FC-104 in the same cooling system (as expected).

j. The lasing threshold is lower for FC-104 than it is for water (3.4 versus 3.8 J), and their slope efficiencies are equal. The lower threshold for FC-104 is due to the increased absorption of water at laser rod-pump wavelengths.

k. The energy output stability using FC-104 coolant is degraded because of this thermal distortion in the laser rod. This was evident when the coolant was switched to water. Hence, an improved coolant flow in the pump cavity would improve the output stability of the resonator.

l. Using water coolant, the energy output achievable is present immediately unlike the case with FC-104 coolant where a thermal distortion is relied upon to effectively optimize the alignment of the resonator (see Appendix G-2).

m. FC-104 coolant is much easier to use than water coolant, especially from the fill standpoint.

n. Use of a deflection plate to redirect coolant flow toward the hotter portion of the laser rod would be difficult to incorporate, since the flashlamp occupies the central portion of the entrance channel (see Fig. C.2-4).

o. Use of a second entrance port may appreciably reduce the thermal gradient in the laser rod. Unfortunately, this is awkward to incorporate from the system design standpoint.

p. Placement of coolant ports near the flashlamp electrodes is practical to the extent that the flashlamp is over an inch longer than the laser rod. However, a new pump cavity design should be initiated which emphasizes cooling the laser rod rather than the flashlamp electrodes. Data are available to indicate that the flashlamps can safely operate at temperatures in excess of 175°C.

q. Coolant baffles within the pump cavity may reduce the thermal misalignment of the resonator, but are not expected to improve the raw-beam divergence figure significantly. (An improved pump cavity design is in progress.)

NOTES:

1. The fringe count data as related to raw-beam divergence are not exact, as the laser rod center is under compression and therefore cannot change shape freely.

2. The interferometric analysis provided here has been used to test the coolant flow characteristics of pump cavities using various coolants, pump cavity shapes, and coolant flow rates.

3. The cylindrical pump cavity shape was so small in diameter (and hence the rod and flashlamp were so near the walls) that coolant did not flow readily around the rod.

Appendix C-3

FERMAT'S PRINCIPLE APPLICATION TO A RAY TRAJECTORY IN A LASER ROD DUE TO AN INDEX OF REFRACTION GRADIENT

1. The steady-state operating temperature of a laser rod can be measured by an interferometric technique. Due to the pump cavity shape and non-uniform coolant flow, there may exist a thermal gradient from one side of the laser rod to the other. This effect creates a length difference and a refractive index gradient in the laser rod. This portion of Appendix C examines the effect on an index gradient on the path of an incident ray which is incident parallel to the laser rod axis. It is shown that the index gradient causes the equivalent of a resonator misalignment.

2. Fermat's principle states, physically, that light travels from one point to another along that path taking the least amount of time; i.e., along the minimum optical path length. Hence, by applying Fermat's principle to a ray traversing the laser rod of length 1, then the position that the ray strikes the laser rod in the other coordinate should be calculable. Fermat's principle states, mathematically, that if light travels from one point to another along a path, that optical path length is shorter than any other path length that can be drawn between these two points regardless of how close to the actual path a second path has been chosen. Fermat's principle is consistent with the basic equation of the calculus of variations—namely, Euler-Lagrange's equation—and is equivalent to it. This fact will be used to establish the ray trajectory in the laser rod.

3. Consider the index gradient Δn one-dimensional and normal to the laser rod axis. A ray incident parallel to the laser rod axis will have an optical path length $P = ns$, where n is the index of refraction and is a function only of the y coordinate (perpendicular to the laser rod axis); s is the arc length of the ray trajectory. But the arc length s is given mathematically by

$$s = \int_a^b \left[1 + (dy/dx)^2\right]^{\frac{1}{2}} dx \qquad (1)$$

and the optical path length becomes

$$P = \int_a^b \left[n_o + \Delta n(y/2R)\right]\left[1 + (dy/dx)^2\right]^{\frac{1}{2}} dx = \int_a^b F(y, dy/dx)\, dx \qquad (2)$$

98

where

$$n(y) = n_o + \Delta n(y/2R)$$

The optical path length must be a minimum by Fermat's principle. Fermat's principle agrees with the Euler-Lagrange equation which states that

$$\partial F/\partial y - d(\partial F/\partial y')/dx = 0 \tag{3}$$

and since $F(y, dy/dx)$ is not a function of x explicitly, then it can be simplified to

$$F - y'(\partial F/\partial y') = C, \text{ a constant} \tag{4}$$

where $y' = dy/dx$. Figure C.3-1 shows the ray-trajectory-problem geometry and the boundary conditions. The ray is everywhere normal to the wavefront propagating through the laser rod and is grossly exaggerated in deflection.
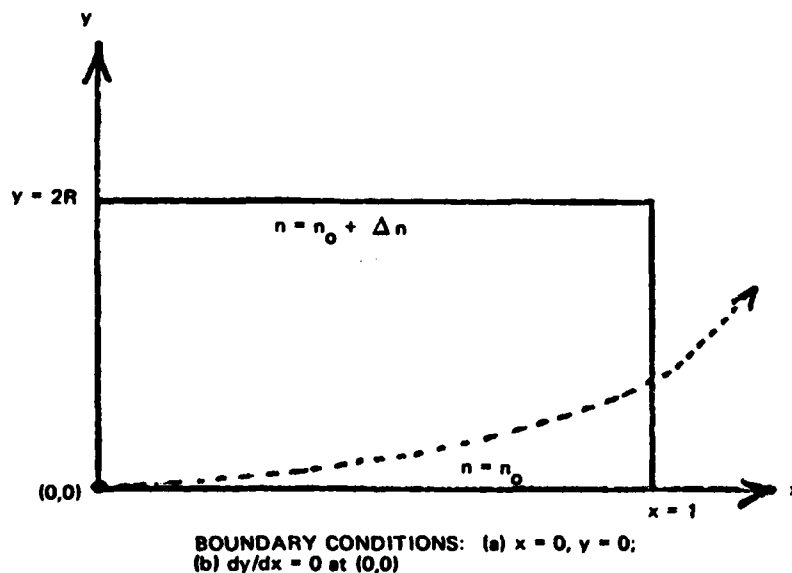

BOUNDARY CONDITIONS: (a) x = 0, y = 0; (b) dy/dx = 0 at (0,0)

FIG. C.3-1. Ray Trajectory Geometry.

4. Using Eq. 4, the steps in sequence follow:

$$n(y)\left(1 + y'^2\right)^{\frac{1}{2}} - y'n(y)\left(1 + y'^2\right)^{-\frac{1}{2}} y' = C \tag{5}$$

$$n(y)/C = \left(1 + y'^2\right)^{\frac{1}{2}} \tag{6}$$

$$n^2(y)/C^2 = 1 + (dy/dx)^2 \tag{7}$$

$$\int dx = \int C\, dy / \left[n^2(y) - C^2\right]^{\frac{1}{2}} \tag{8}$$

$$\text{Let } z = n(y) = n_0 + \Delta n\ (y/2R) \tag{9}$$

$$dz = (\Delta n/2R)\,dy = N_k\,dy \tag{10}$$

$$x = C/N_k \int dz / \left[z^2 - C^2\right]^{\frac{1}{2}} \tag{11}$$

$$x = C/N_k \log\left(z + \sqrt{z^2 - C^2}\right) + C' \tag{12}$$

where C and C' are both constants to be established by the boundary conditions shown in Fig. C.3-1. The boundary conditions at $x = y = 0$ implies $z = n_0$ and so

$$C' = -C/N_k \log\left(n_0 + \sqrt{n_0^2 - C^2}\right) \tag{13}$$

so that

$$x = C/N_k \left[\log\left(z + \sqrt{z^2 - C^2}\right) - \log\left(n_0 + \sqrt{n_0^2 - C^2}\right)\right] \tag{14}$$

The differential of

$$dx = C/N_k\,dz / \left(z^2 - C^2\right)^{\frac{1}{2}} \tag{15}$$

yields the requirement that $C = n_0$ by the boundary condition of $dy/dx = 0$ at $x = y = 0$. So then finally, the equation

$$x = n_0/N_k \left[\log\left(z + \sqrt{z^2 - n_0^2}\right) - \log n_0\right] \tag{16}$$

describes the (x,y) coordinates of the ray trajectory as it traverses the laser rod. To find the deviation of the ray and its location at $x = 1$—i.e., its y coordinate after traveling through the laser rod—it is required that

$$\ell N_k/n_0 + \log n_0 = \log\left(z + \sqrt{z^2 - n_0^2}\right) \tag{17}$$

100

which will provide, when solved for y, the deviation of the ray upon traversing the thermally distorted laser rod.

5. The value of N_k is given by

$$N_k = 0.915 \times 10^{-6} \, N/2R = 1.44 \times 10^{-6} \, N \tag{18}$$

where again, N is the number of fringes observed (at the probe wavelength) at the equilibrium operating laser rod temperature condition for the interferometer. As an example to show the magnitude of the beam deviation caused by the refractive index gradient (and to make the problem solvable with 10 significant figures using log tables and a portable HP computer), let the term

$$N_k \ell/n_o = 4.35 \times 10^{-5} \tag{19}$$

which would correspond to over five fringes of thermal distortion in the laser rod. Then these steps follow, using the log tables and a desk calculator:

$$0.0000435 + 0.2624510897 = \log\left(z + \sqrt{z^2 - n_o^2}\right) \tag{20}$$

$$2.2624946897 - 2.0000000 = \log\left(z + \sqrt{z^2 - n_o^2}\right) \tag{21}$$

$$\log(183.01842) - \log(100) = \log(1.8301842) \tag{22}$$

$$(1.8301842 - z)^2 = z^2 - n_o^2; \text{ assume } n_o = 1.83000000 \tag{23}$$

$$z = 1.830000009 \tag{24}$$

$$9 \times 10^{-9} = N_k y = 1.05 \times 10^{-5} y \tag{25}$$

$$y = 8.65 \times 10^{-4} \text{ cm} \tag{26}$$

Hence a ray starting parallel to the laser rod axis exits the other end of the laser rod, by including Snell's law of refraction at the surface, at an angle θ where

$$\theta = n_o y/\ell = (1.83)(8.65)10^{-4}/7.63 = 0.2 \text{ mrad} \cong 41 \text{ arcsec} \tag{27}$$

A larger fringe count was chosen here than is encountered in practice so that the results were calculable with 10-place log tables. The result, therefore, is that for every pass a photon (or ray) makes between the end mirrors of the resonator, its path is being continually curved in one direction until it leaves the resonator. This creates an effective resonator misalignment (as does a physical length difference) due to the thermal distortion in the laser rod. An alignment correction is then required to negate its effect. The net result is that when the laser is first turned on, it is slightly misaligned and so its output is initially less than optimum.

NOTES:

1. The thermal misalignment of the resonator due to a transverse gradient is calculated here. A radial gradient is shown to be superimposed upon this gradient, as described in Appendix E-4.

2. A transverse index of refraction gradient is usually accompanied by a length difference in optical path length. A physical length difference provides a thermal misalignment since the wavefront is deviated as if a thin optical wedge were installed in the resonator. In effect the resonator must be aligned to compensate for it.

3. Though not described here, the complex mode structure of the resonator changes when the resonator is misaligned. This causes a shift in energy distribution within the resonator as well as in the output beam. Non-Q-switched beam uniformity is described in Appendix F-1.

Appendix C-4

COOLANT FLOW RATE TESTS

1. This portion of Appendix C describes test procedures and test results which measure raw-beam divergence and axial thermal gradient in the pump cavity as a function of coolant flow rate and pulse repetition rate. The purpose of these tests is to establish those thermal conditions and design properties necessary in the pump cavity design to minimize its contribution to an increased raw-beam divergence and the thermal misalignment of the resonator. The raw-beam divergence value was measured at a fixed coolant flow rate of near 16 gal/hr and an 8-J/pulse input energy to an in-line, end dump, non-Q-switched laser resonator. These results showed that a resonator operating at a 10-Hz rate has a raw-beam divergence about 0.7 mrad larger than if it were operating at a 1-Hz rate.

2. To establish the dependence of raw-beam divergence on coolant flow rate, the rate was varied from 3 to over 20 gal/hr. (The PD-type coolant pump provides a coolant flow rate of about 16 gal/hr.) The net result at a 10-Hz repetition rate was that the raw-beam divergence changed only a few tenths of a milliradian over the coolant flow rate range. The thermal distortion of the laser rod in terms of fringe count changed very little over the flow rate range as well. Together these results implied that the axial thermal gradient in the pump cavity is not directly proportional to the coolant mass flow rate. To test these implications, copper-constantan thermocouple wires were placed in the coolant path near the inlet and outlet ports of the pump cavity. The measured axial thermal gradient as a function of the coolant flow rate is shown in Fig. C.4-1. In general, it shows that increasing the coolant flow rate by even 50% from its present value of 16 gal/hr would provide only about 25% improvement in the axial thermal gradient. The fact that the raw-beam divergence changed only a few tenths of a milliradian (less than 10% of the total raw-beam divergence) while the coolant flow rate was varied from 4 to 20 gal/hr (which varied the axial thermal gradient by nearly a factor of two) strongly suggests that the raw-beam divergence increase with repetition rate is dependent only upon the flashlamp radiation it absorbs per unit time (or per second) and not the axial thermal gradient.

3. The axial thermal gradient was then measured as a function of pulse repetition rate (and so indirectly the input power) at two fixed coolant flow rates. The results of this test are shown in Fig. C.4-2 for a coolant flow rate of 3 and 16 gal/hr. These tests show that the axial thermal gradient increases linearly with the pulse repetition rate (as does the raw-beam divergence described earlier). The dependence of the maximum axial thermal gradient on the input power should be linear as, in theory,

FIG. C.4-1. Axial Thermal Gradient as a
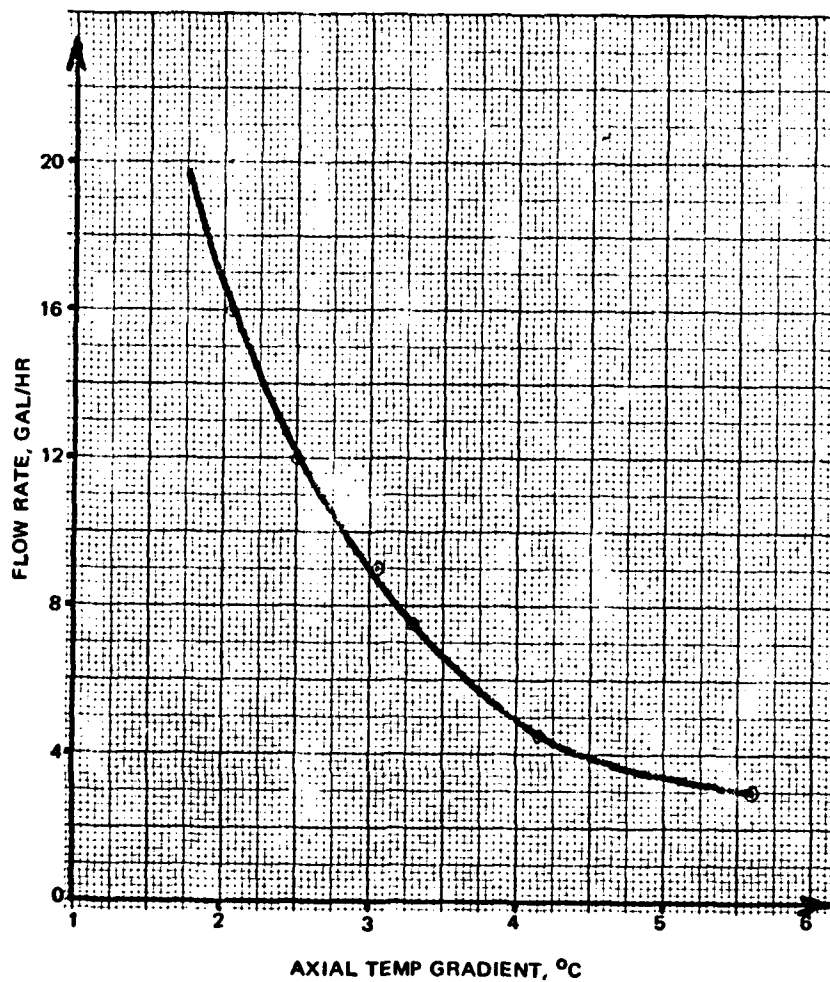Function of Coolant Flow Rate.

$$Q = 1.8 \ M_f \ C_p \ \Delta T_m \tag{1}$$

where

Q = input power to flashlamp, Btu/hr: 80 W = 272 Btu/hr

     = $E_{in} \ F$, the product of the input energy per pulse and repetition rate

M_f = mass flow rate of coolant, lb/hr

C_p = specific heat of coolant, Btu/lb-°F

ΔT_m = maximum possible axial thermal gradient, °C

104
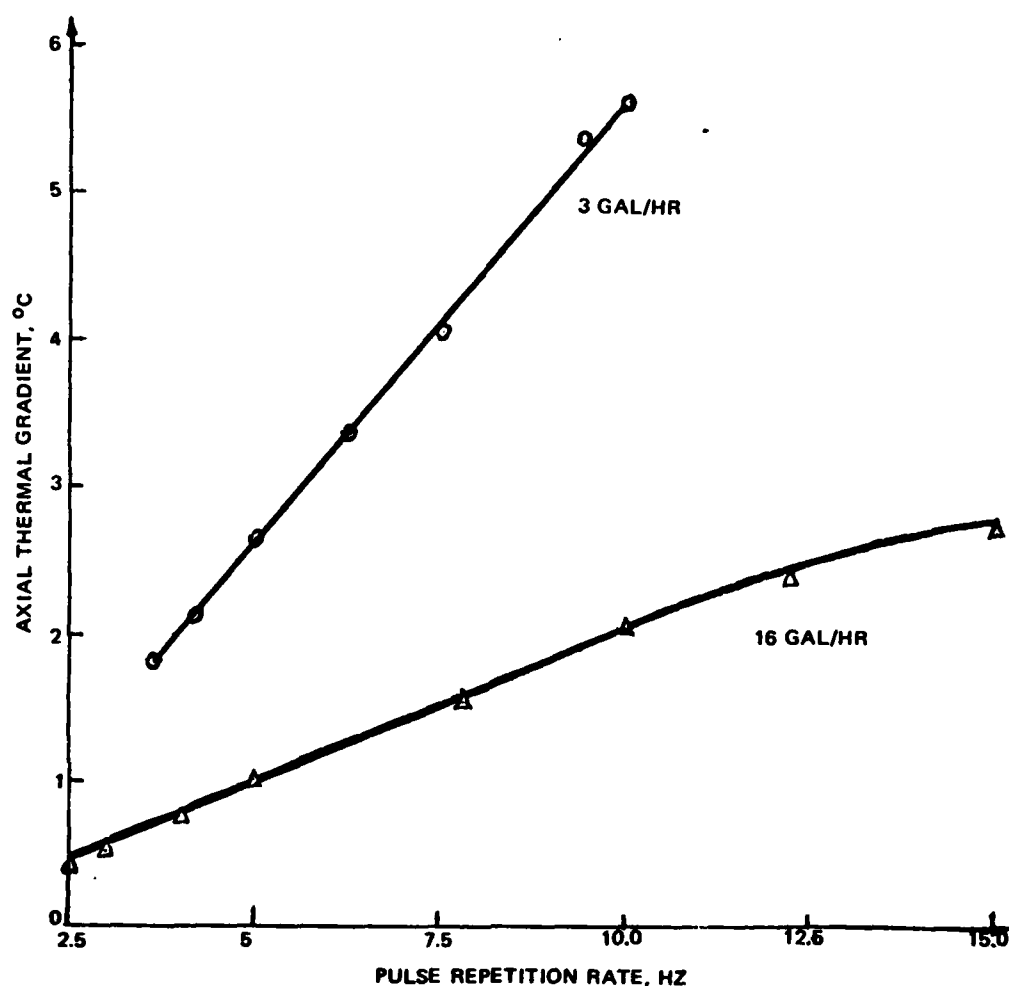
FIG. C.4-2. Axial Thermal Gradient as a Function of Repetition Rate.

This equation shows that the maximum axial thermal gradient is directly proportional to the heat load and the pulse repetition rate and is inversely proportional to the mass flow rate. The thermal transfer coefficient K is a multiplicative factor included to the right side of this equation when experimental axial thermal gradients are measured, since the coolant does not remove all the pump power supplied to the pump cavity. The factor K may be a function of the coolant flow rate through the pump cavity, especially under laminar coolant flow conditions. At a 16-gal/hr coolant flow rate and an 80-W heat load, the maximum axial thermal gradient possible is directly

$$\Delta T_m = (272)5/9(16)8.33(109/61)(0.25) = 2.53°C \tag{2}$$

But, as shown in both figures, the actual axial thermal gradient was about 2.05°C. So then K = 0.8, which means that about 20% of the heat load is dissipated elsewhere and is not being conveyed by the coolant.

4. The effect of modifying the coolant flow pattern in the pump cavity was then tested. At a flow rate of 16 gal/hr for a pulse repetition rate of 10 Hz, the axial thermal gradient and the raw-beam divergence were not improved by inserting a coolant baffle between the laser rod and flashlamp. The raw-beam divergence as a function of pulse repetition rate remained unchanged as well. The residual fringe count was unusually large, which implied that the baffle plate was producing a stress on the laser rod. But judging by the fringe motion during the flashlamp pumping, the hottest portion of the laser rod was that nearest the flashlamp where the coolant flow was restricted due to the baffle plate. The axial thermal gradient should be reduced solely on the basis of its effect on the thermal misalignment of the laser resonator, if for no other reason. The resonator is not optimally aligned when first turned on and, as a result, the output energy is degraded until the thermal distortion effectively aligns the resonator. Coolant baffle design may solve this thermal distortion problem even though it apparently provides little, if any, improvement in the axial thermal gradient or the raw-beam divergence from the resonator.

5. A samarium-doped glass insert was tested to establish whether or not off-axis 1.06μ absorption affects the raw-beam divergence figure. The raw-beam divergence as a function of repetition rate remained unchanged within the experimental error of the measurement (at the single flow rate of 16 gal/hr). For purposes of comparison with earlier data, the raw-beam divergence as a function of input energy was measured and was found to be 0.16 mrad/J change. The prior result obtained was 0.2 mrad/J.

6. These FC-104 coolant flow rate tests indicate the likelihood that little can be done to reduce the axial thermal gradient in the pump cavity. The fact that the raw-beam divergence increase is relatively unaffected by mass flow rate means that the optimum pump cavity design should be established mainly by the pump uniformity and coupling efficiency considerations.

7. Tests were then performed using EGw (ethylene glycol water) and water as the laser coolants. The test results can be summarized as follows:

    a. At a flow rate of 16 gal/hr and a 10-Hz pulse repetition rate, both coolants (EGw and water) showed an axial thermal gradient of 0.90 ±0.05°C (or, under similar conditions, only about half that gradient measured with FC-104 coolant).

    b. At a flow rate of 16 gal/hr and a 5-Hz pulse repetition rate, the axial thermal gradient was about 0.475°C using EGw; and as with the FC-104 coolant, the axial thermal gradient is proportional to the pulse repetition rate.

106

c. The raw-beam divergence dependence with pulse repetition rate for both coolants was near that using FC-104 coolant; namely, on the average, 0.066 r·ad/Hz. This means again that the axial thermal gradient, though affecting the alignment of the resonator, has little effect on the raw-beam divergence figure.

d. At a coolant flow rate of 5 gal/hr and a 10-Hz pulse repetition rate, the axial thermal gradient was 1.93°C, although the raw-beam divergence changed only slightly as with the FC-104 tests.

e. Use of a higher ultraviolet cutoff flashlamp envelope (Heliosil versus Germasil) showed no improvement in raw-beam divergence value. It becomes increasingly evident that only the absorbed flashlamp radiation (and perhaps its distribution) in the laser rod creates the raw-beam divergence dependence on input power level.

8. A new pump cavity design will now proceed with design emphasis on uniform, high-efficiency pumping of the laser rod. Provisions for the optional use of a baffle plate are being planned. This baffle plate may serve several purposes including improved coolant flow pattern, 1.06μ absorption and/or reduce the absorption of useless flashlamp radiation by the laser rod. YAG, the host material, absorbs essentially all flashlamp radiation below about 3000Å (with some variations due to impurity doping levels) which creates avoidable internal heating. Presently under study are new coolants and coolant additives (chromogens) which absorb and, in some cases, reradiate absorbed flashlamp radiation at more useful wavelengths to the laser rod. Supporting studies on the predicted radial thermal gradient for water and FC-104 coolants, the effects of color center formation due to the UV absorption by the YAG, and a reinterpretation of thermal distortion are planned or are in progress at this time.

NOTES:

1. The interferometric observations made used the test apparatus shown in Appendix C-2.

2. The quartz baffle plate used for the flow pattern improvement tests was placed axially between the flashlamp and the laser rod within the pump cavity. It was configured with projections and holes to direct coolant flow along the laser rod predominantly.

3. The samarium insert was configured as an 0.5-mm-thickness cylindrical sleeve which fit into the cylindrical pump cavity. Its primary purpose in use is to reduce the off-axis 1.06μ transmission and prevent lateral depumping of the laser rod. The fluorocarbon, FC-104, is essentially transparent at 1.06μ, unlike an ethylene glycol/water mixture.

4. The use of a higher ultraviolet cutoff envelope for the flashlamp did not improve the beam divergence figure noticeably mainly because of cavity wall reflectance and poor quantum efficiency in the pump bands around 3500 Å. (See Appendix C-6.)

Appendix C-5

RADIAL THERMAL GRADIENT IN THE LASER ROD

1. The purpose of this portion of Appendix C is to show calculations made to determine the radial thermal gradient in the laser rod for a simplified laser rod cooling geometry. Data are also provided on the surface heat-transfer coefficient for the laser rod, the predicted axial thermal gradient and its agreement with experimental results, and the transverse coolant temperature gradient. The thermal properties of a particular continuously pumped continuous wave (CW) Nd:YAG laser pump cavity are described in APPLIED OPTICS, Vol. 9 (1970), p. 1429, and show that:

 a. The radial thermal gradient between the laser rod center and its edge is given by

$$\Delta T_r = P_{abs}/4\pi K_r L$$

where

 P_{abs} = power absorbed in laser rod

 K_r = thermal conductivity of the rod

 L = length of rod

Note the equation is independent of coolant properties, so the same radial thermal gradient is expected for water and FC-104.

 b. The axial thermal gradient for uniform coolant flow is given by the equation

$$\Delta T_c = P_{in}/m_f C_p$$

where

 P_{in} = input power to the flashlamp

 m_f = coolant mass flow rate

 C_p = specific heat of coolant used

c. The difference between the average laser rod temperature and the average coolant temperature is given by

$$\Delta T_g = P_{abs}/hA \quad .$$

where h is the laser rod surface heat-transfer coefficient and A is the surface area of the laser rod. The parameter h is a complex function of the cooling geometry and will be calculated here for both FC-104 and water coolant.

The calculation for the radial thermal gradient will serve to show, together with past experimental results, the contribution of pump cavity thermal properties to the resonator raw-beam divergence.

2. On page 111, tabulations are given for the needed physical properties of the laser rod, the coolant, and the cooling geometry chosen to make the thermal gradient calculations. They also show the formulas used in the calculations which follow. In summary, it can be said that:

a. Since $m_f C_p$ for FC-104 and water differ by about a factor of two, the axial thermal gradient should also differ by this amount. The axial thermal gradients were measured for FC-104 and water and were 2.05°C and 0.90°C, respectively, for an 8-J pump level at a 10-Hz rate.

b. The cooling annulus geometry was chosen so that the mass flow rate was roughly equivalent to that of our present cooling system. The low Reynolds number for both FC-104 and water makes it evident that the coolant flow is extremely laminar and the use of a baffle in the pump cavity can do little to increase the Reynolds number (to make the coolant flow more turbulent). Baffles may, however, improve the uniformity of the coolant flow.

c. Since the surface heat-transfer coefficient for water is about 3.5 times larger than it is for FC-104, the transverse thermal gradient in the coolant is about this factor larger for FC-104 as compared to water. This contributes to the thermal distortion problem encountered with the use of FC-104 coolant.

d. The radial temperature gradient in the laser rod is independent of the coolant used and is approximately 0.45°C for an 8-J input at a 10-Hz rate. Hence, if the thermal distortion and the passive residual distortion of the laser rod are neglected, the center of the laser has a path length of two-thirds of a wavelength longer than the edge of the laser rod. The temperature distribution from center to edge is parabolic.

3. Remaining tasks are to calculate the predicted effect on raw-beam divergence due to this optical path length difference in the presence

of thermal distortion and to compare this figure with related experimental results obtained in the past. An interpretation of a thermal focusing effect in the presence of thermal distortion is shown in Appendix E-4 to be consistent with the past raw-beam divergence data using various end-mirror curvatures, input energy levels, and pulse repetition rates.

PUMP-CAVITY PROPERTIES

Laser Rod:

K_r (thermal conductivity) = 26.5 $(10)^{-3}$ cal/sec-cm-°C

Coolants:

	Water	FC-104
K_c (thermal conductivity in cal/sec-cm-°C)	$1.36(10)^{-3}$	$2.18(10)^{-4}$
μ (viscosity in g/cm-sec)	10^{-2}	$2.65(10)^{-2}$
C_p (specific heat in cal/g-°C)	1.0	0.26
γ (volumetric expansion coefficient in °C^{-1})	$0.64(10)^{-4}$	N/A
ρ (density in g/cm^3)	1.0	1.725

Pump Geometry:

Assume P_{abs} = 6% of input power in cal/sec.

Require that the flow rate be 15 cm^3/sec and that the coolant be exchanged every second around the laser rod (as is roughly the case now). Then the coolant volume around the laser rod must be 15 cm^3. Form an annulus around the laser rod as shown below

and require that

$$V_F = 0.786(D_2^2 - D_R^2)L = 15$$

which yields that D_2 = 17.1 mm. Note that m_f(water) = 15 g/sec and m_f(FC-104) = 28 g/sec.

Thermal Properties Calculations:

1. G (mass flow rate per unit area of flow) $= 4 m_f/\pi(D_2^2 - D_R^2)$

$$= 0.508 \; m_f$$

G (water) $= 7.62$ g/sec-cm^2

G (FC-104) $= 14.2$ g/sec-cm^2

Note that $m_f C_p = 15$ (water) and 7 (FC-104).

2. N_{Re} (Reynolds number) $= (D_2 - D_R)G/\mu$

N_{Re} (water) $= 819$

N_{Re} (FC-104)$= 576$

For laminar flow, the Reynolds number should lie between 900 and 2,000.

3. N_{Pr} (Prandtl number) $= C_p \mu/K_c$

N_{Pr} (water) $= 7.35$

N_{Pr} (FC-104) $= 31.6$

4. N_{Gr} (Grashof number) $= (D_2 - D_R)^3 \rho^2 g\gamma(\Delta T_c)/\mu^2$ where g is the gravity constant. It has a minor effect on the parameter h as shown below and is not needed in the calculation for h which follows.

5. h (surface heat-transfer coefficient for laminar flow):

$$h = 1.02 \; K_c N_{Re}^{.45} N_{Pr}^{.50} N_{Gr}^{.05} \left[\left(D_2 - D_R\right)/L\right]^4 (D_2/D_R)^{.8} (D_2 - D_R)^{-1}$$

$= 0.072$ cal/cm^2 – sec – °C for water

$= 0.0205$ cal/cm^2 – sec – °C for FC-104

6. The radial thermal gradient $\Delta T_r = P_{abs}/4\pi KL = 0.45$°C regardless of the coolant type used.

7. The optical path length through the laser rod is different from the edge to the center and is given by the equation

$$\Delta P = \left| n\alpha + (\Delta n/\Delta T)\right| \ell \Delta T(°C) = 0.65 \; \lambda$$

where $n = 1.83$ (the refractive index of the laser rod), $\alpha = 6.9(10)^{-6}$°C^{-1} (the linear expansion coefficient of the rod), ℓ is the laser rod length, and $\Delta n/\Delta T = 7.3(10)^{-6}$°C^{-1} (the refractive index rate of change with the laser rod temperature).

NOTES:

1. The radial thermal gradient will be shown to be the cause of the increased raw-beam divergence with input pump power. The transverse thermal gradient due to the nonuniform coolant flow in the pump cavity, though present, is neglected here (see Appendix E-4).

2. The calculations (page 112, paragraph 7), are not exact as shown in Appendix E-4

Appendix C-6

EFFECTS OF ULTRAVIOLET ABSORPTION

1. It can be shown that the radial thermal gradient, which occurs simultaneously with thermal distortion due to nonuniform cooling, produces a thermal focusing effect which increases the resonator raw-beam divergence with input pump power (or pulse repetition rate). This internal heating that the laser rod must dissipate is due to two sources: (1) YAG host absorption in the ultraviolet (UV), and (2) dopant impurity absorption in the visible and near infrared region. The dopant impurity absorption, namely by the Nd^{+3} ion, is of course necessary to get the population inversion in the laser rod. The UV absorption of YAG increases rapidly below 2900Å (absorbance greater than 0.1 cm^{-1}) and is thought due, in some part, to undesirable impurities accepted by the melt during the Czochralski growth process. These impurities are also thought to produce color centers which cause the laser rod to absorb more strongly in the UV and low visible wavelengths after the laser rod has encountered prolonged exposure to UV flashlamp radiation. (An in-house laser rod which has been used extensively during the past two years has developed this absorption characteristic.) Although the neodymium ion absorption is necessary, localized heating is produced in the laser rod due to nonradiative transitions resulting from this absorption. Results of tests which establish the contribution of UV absorption to the resonator raw-beam divergence figure are provided here.

2. An organic liquid, dimethyl phthalate (DMP), was used as the laser coolant to absorb essentially all the flashlamp radiation below 3100Å. It should be remembered that the flashlamp radiates roughly as a 7000°K blackbody (at a 12-J input level) and so about 10% of its output lies below 3100Å wavelength. DMP does not interact with silver, aluminum, or Viton O-rings but does interact slightly with polyethylene tubing. Hence DMP is an excellent laser coolant to use to determine the effect of UV absorption on the raw-beam divergence. This coolant has a higher index of refraction, thermal conductivity, boiling point, viscosity, and heat of vaporization than FC-104 coolant. (DMP is also being used as a solvent for dyes which selectively absorb and reradiate flashlamp radiation. These dyes are being tested to determine whether or not improved pumping efficiency can be achieved by using dyes which reradiate in the absorption bands of the neodymium ion. Test results using this technique for improved pumping efficiency will be the subject of a later memorandum.)

3. Figure C.6-1 shows the raw-beam divergence data for the two pulse repetition rates of 1 and 10 Hz. The data indicate that the raw-beam divergence increases at the rate of 0.056 mrad/Hz; namely, within 25% of the value using FC-104 (0.075 mrad/Hz) or EGw (0.066 mrad/Hz) coolants.
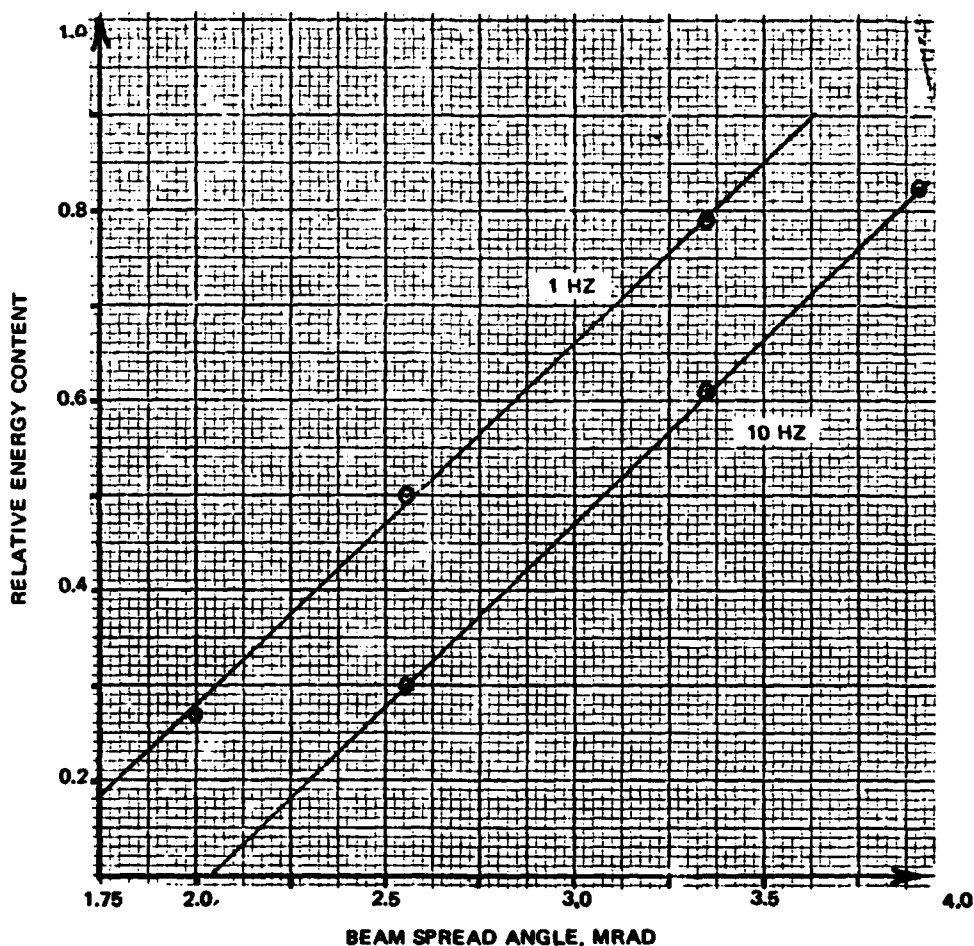
FIG. C.6-1. Raw-Beam Divergence Test Data.

These data then show that the UV absorption by the YAG host material is not contributing significantly to the raw-beam divergence increase with input pump power. Three related absorption characteristics may be helping this effect: (1) the flashlamp envelope absorbs all radiation below 2450Å, (2) the YAG absorption coefficient becomes very large in the UV so that much of this radiation is being absorbed close to the surface of the laser rod, and (3) silver reflectance decreases rapidly below 3500Å. Hence, from the raw-beam divergence standpoint, little can be gained in using higher UV cutoff flashlamp envelopes; e.g., Nonex. These data also imply that little can be done in the pump cavity design to reduce the raw-beam divergence increase with input pump power (or pulse repetition rate) since it appears that the internal heating effect is due mainly to nonradiative transitions produced by dopant impurity absorption.

NOTES:

1. The effects of UV absorption and its indication of laser coolant degradation are described in Appendix G-1.

2. These results show that little UV radiation is absorbed by the laser rod. However, on the basis of increased coolant life and operating efficiency, higher wavelength cutoff flashlamps are of interest.

3. The DMP coolant had particular dyes which absorbed the low visible flashlamp pump radiation and reradiated at higher wavelengths. The operating efficiency was enhanced by 25% for a short time, after which the DMP was polymerizing and so changing physical properties-- in part, absorption characteristics.

4. The UV absorption by the coolant is desirable from the heat-transfer standpoint and because it reduces the silver coating absorption of UV radiation as well.

5. Other organic solvents are to be tested with dyes.

Appendix C-7

PUMP CAVITY INSERT PERFORMANCE COMPARISON

1. The need for a pump cavity insert has evolved from the requirement for insulating the pump cavity due to parallel triggering of the flash-lamp. The glass epoxy pump cavity insulates the high-voltage flashlamp trigger pulse (typically 10-kV peak amplitude) from the T-beam resonator. Over the past several weeks, the author has tested several combinations of insert material (quartz and samarium glass) coated with evaporated metal films (gold and silver) as well as a diffusing paint (Eastman white reflectance paint). The performance of these pump cavity inserts was compared (each time data were taken) to the conventional electro-plated, silvered cylindrical pump cavity made by the PD contractor.

2. Figure C.7-1 shows the relative energy output versus input pump level for the pump cavity inserts tested. All data were taken with FC-104 cool-ant, a 70% end-dump mirror, a 100% 10-meter radius of curvat re end mirror, and a krypton-filled flashlamp fired at 10 pps. Output energy was mea-sured over the input energy range of 6.5 to 10 J, although the individual data points are not shown. From the results given in Fig. C.7-1 and supporting experimental data, it is evident that:

    a. The silvered quartz (second surface) insert is nearly 20% more efficient than the conventional electroplated pump cavity. (Admittedly, the latter pump cavity has been used extensively and polished many times.) Further testing of the silvered glass insert (quartz or samarium) has indicated that the evaporated, vacuum-deposited silver does not adhere well, especially after exposure to the thermal effects produced by the flashlamp. Even though a protective coating is applied over the silver (evaporated aluminum, then a sealant cement), the heating produced by the close proximity of the flashlamp causes the silver to lift from the insert. As a result the pump-cavity performance degrades quite rapidly. Unless a more adherent coating technique is found, it seems probable that this approach to a pump-cavity design (to ensure long-term perfor-mance) is unacceptable.

    b. Both an uncoated-quartz and a samarium insert were tested in the cylindrical pump cavity. Neither insert degraded the efficiency signif-icantly. However, the output efficiency was reduced by about 10% when the samarium glass insert was silvered. The quality of the surface of the samarium glass was not good; hence the silver coating was also infer-ior to that possible on the quartz insert. The coating quality was also evident by viewing the inner surface of the insert and comparing it to that of the silvered-quartz insert.
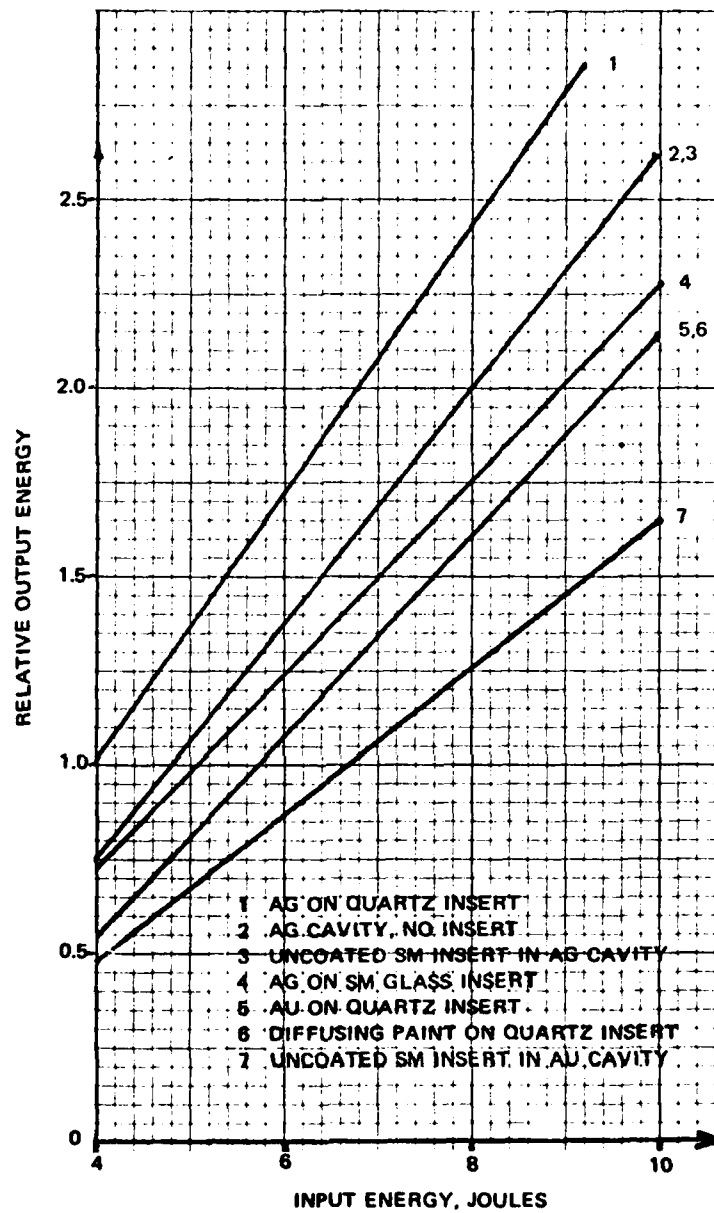
FIG. C.7-1. Pump Cavity Inserts.

c. The efficiency of an evaporated gold surface is the same as that for Eastman white reflectance paint on a quartz insert. When tested several days later, the latter pump cavity was about 12% less efficient due to surface degradation by the coolant. The output beam was very uniform with the diffusing paint insert but no quantitative measurements were made. If power-density damage problems are increased on the modulator due to the smaller coupling geometry (it presently seems probable), then the diffusing pump cavity approach may warrant further study and consideration. Quantitative measurements on output beam uniformity are being planned by the author.

d. For comparison purposes, an uncoated, samarium glass insert was put into an electroplated gold cavity (from the PD contractor). The krypton flashlamp has much of its useful output in the near infrared, and the gold coating reflects rather poorly there when compared to the silver coating.

3. Though not shown in the data, an electroplated (silvered) insert has an efficiency as good as the silvered quartz insert as evidenced by tests on the T-beam resonator. Since the vacuum-deposited silver does not perform well over an extended period of time, the electroplated insert seems the most attractive alternative at this time. From the pumping uniformity standpoint, this insert is worse than the conventional cylindrical pump cavity due to its smaller size. Hence further study on improved pump cavity reflectors is needed and should be stressed.

NOTES:

1. The inserts were in the form of 0.5-mm thick, cylindrical annuli which fit snugly into the glass epoxy head and around the laser rod and flashlamp.

2. The vacuum-deposited silver coating and other coatings on glass inserts were deposited on the outer surface. These inserts were tested to see whether a second surface insert could be used where the coating was not contacting the coolant used.

3. The vacuum-deposited coatings lift off the quartz insert due to differences in thermal expansion coefficient and because of its high absorption coefficient of flashlamp UV radiation.

4. The Eastman white reflectance paint, #6080, was painted directly on the insert outer surface. It has nearly perfect diffuse reflecting properties with a generally higher reflectance than that of magnesium oxide.

5. By protecting the diffusely reflecting paint from contact with the coolant, the paint maintains its original reflectance very well and does not rapidly degrade due to UV radiation alone.

6. The surface on the samarium insert was not particularly good quality due to the thickness of the glass, and was difficult to polish as a result.

7. The electroplated cylindrical insert is presently in use in the in-house lasers.

8. Increased emphasis is planned on improving the surface quality of the pump cavity reflector.

Appendix D

Q-SWITCHING OF LITHIUM NIOBATE MODULATOR

Appendix D-1

BREADBOARD Q-SWITCH CIRCUITRY

1. Considerable emphasis was needed to develop a reliable and flexible modulator drive circuit. The circuit shown in Fig. D.1-1 was finally adopted. The grounded cathode and the use of a sonic bias on a separate electrode were felt to be improvements over the present PD approach. Although not shown on the schematic, multiple-set series resistors were used in the high-voltage portion; otherwise, breakdown occurred causing excessive current flow from the modulator high-voltage supply. Tests using this circuitry (on a particular resonator) yielded the following results:

    a. The original TVR concept of switching the modulator voltage less than the quarter-wave voltage produces the multiple pulsing; i.e., any negative sonic bias causes multiple-pulsing of the laser output.

    b. Use of an optimum sonic bias and modulator bias voltage increases the output energy by approximately 10% over the case where no sonic bias and a modulator voltage slightly larger than the holdoff voltage is used.

    c. The optimum modulator voltage was the quarter-wave voltage (4,100 V) with a sonic bias of +800 V. (Note: It should be established whether or not the PD output can be increased in a similar manner.)

    d. The holdoff voltage (modulator high-voltage required to prevent prelasing) is approximately 3,300 V. Hence, the use of a modulator voltage near 3,300 V suggests no sonic bias is required for optimum output for that modulator bias high-voltage level.

    e. The holdoff voltage is, of course, dependent upon the extinction ratio of the modulator. The extinction ratio of the damaged lithium niobate modulator used was measured (between parallel polarizers in the component test station to be described in a separate memorandum) as 37:1. This then implies that a modulator extinction ratio of about 10:1 is adequate to prevent prelasing.

    f. The fall time of the modulator high voltage was very fast. However, the voltage oscillated for nearly the pulse build-up time (about 100 nsec). The damped oscillatory behavior of the modulator voltage after Q-switching is consistent with the theory if a stray inductance of 0.5 μH is introduced.
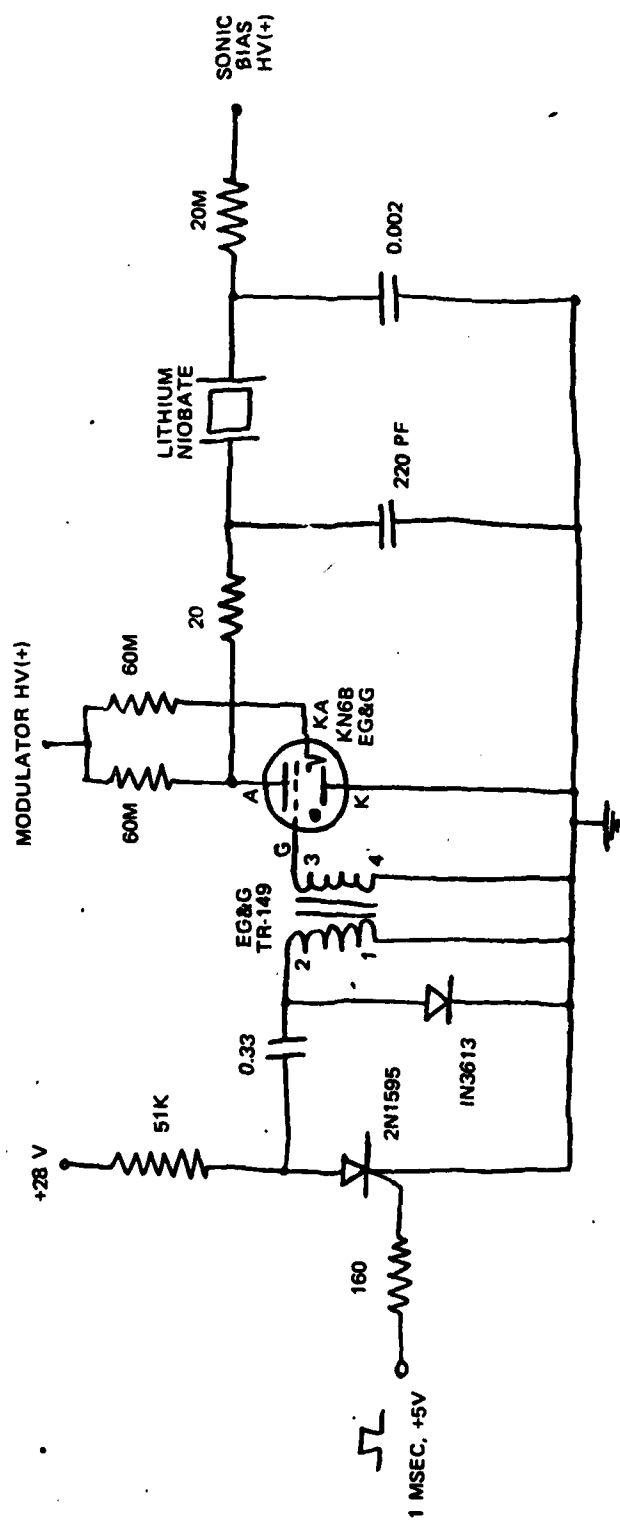
FIG. D.1-1. Modulator Drive Circuit.

NOTES:

1. The test results described were of a preliminary nature and applicable to a particular case rather than in general.

2. The terminology "sonic bias" is simply a bias of the same polarity as that of the holdoff voltage but applied to the opposite electrode. The net result is that when the holdoff voltage is removed (at instant of Q-switching), the bias across the modulator becomes that of the *sonic bias*. The word *sonic* evolved from the piezoelectric properties of the lithium niobate modulator.

3. The Q-switching circuitry allows the use of independent voltage adjustment of holdoff voltage and sonic bias voltage. This capability is important for those tests which attempt to optimize the Q-switching performance.

4. By the circuitry of Fig. D.1-1, it is apparent that the holdoff voltage is the difference between the modulator bias voltage and the sonic bias voltage.

Appendix D-2

Q-SWITCHING RATE REQUIREMENTS

1. It is published in the open literature that for optimum efficiency, the Q of the resonator must be decreased to its maximum value within a time less than the laser pulse build-up time. Recent data (PROC IEEE, Vol. 57 (1971), p. 1126) indicate that even longer modulator voltage-pulse fall times are acceptable.

2. Tests were conducted to measure laser output as a function of modulator voltage fall time with respect to laser pulse build-up time (for the case considered, about 110 nsec). The results are shown in Fig. D.2-1. The subject is discussed further in Appendix D-3.
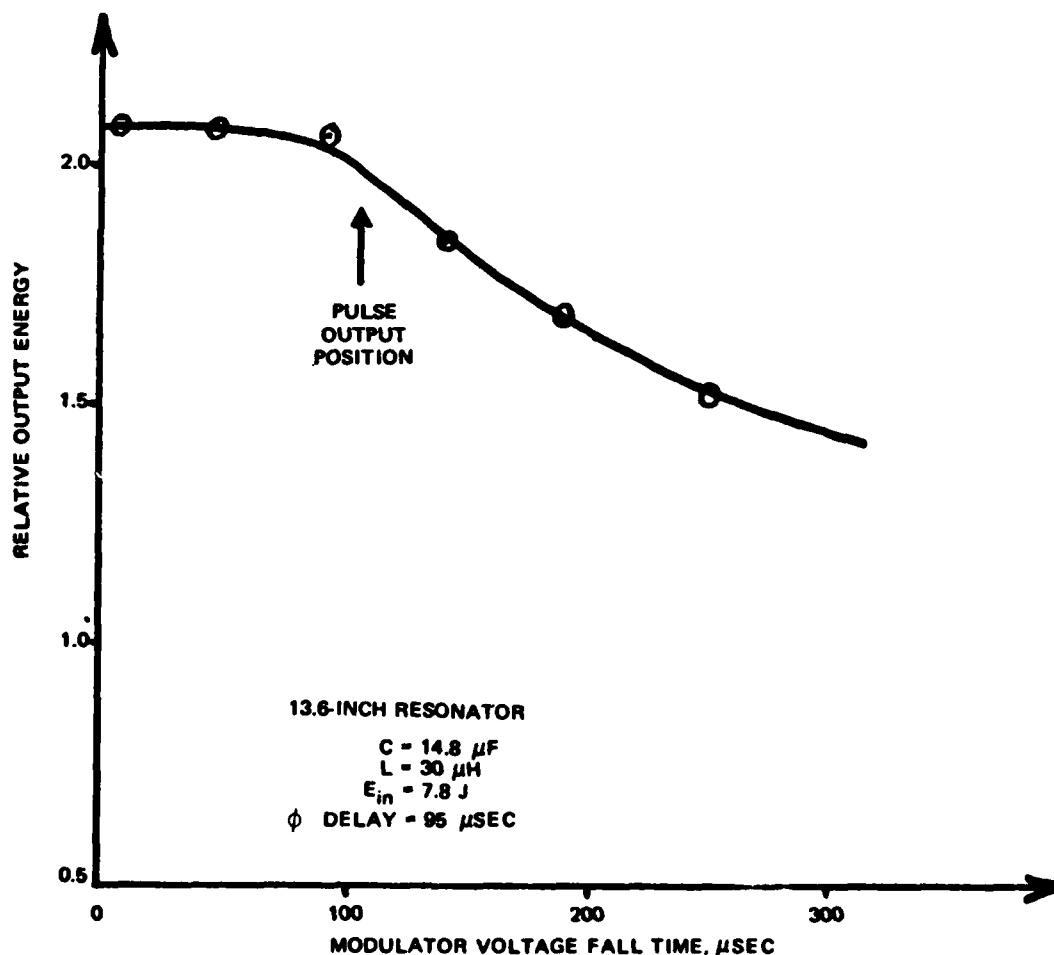

FIG. D.2-1. Energy Output Versus Modulator Voltage Fall Time.

3. The 20-ohm resistor in the circuit diagram shown in Fig. D.1-1, Appendix D-1, was changed to vary the modulator voltage fall time.

NOTES:

1. The in-house lasers use an SCR-transformer combination to drive the modulator. For a modulator with a quarter-wave voltage near 1,500 V (25-mm-length modulator), the transformer output pulse amplitude is generally near 2,200 V for optimum Q-switch performance.

2. The Q-switch electronics used for the tests described here were those discussed in Appendix D-1.

3. It has been found necessary to optimize Q-switching performance for each assembled T-beam by varying the modulator trigger-pulse delay (with respect to the flashlamp trigger pulse) and modulator voltage pulse amplitude during active testing.

Appendix D-3

Q-SWITCHING IN THE T-BEAM

1. Previously, it was stated that the resonator output energy could be increased by using a modulator voltage near the quarter-wave voltage (about 4,100 V) and a +800-V sonic bias. It was also found that the optimum sonic-bias voltage increased as the modulator voltage increased. Conceptually, this behavior is explainable if the transmission of the modulator does not obey the $\sin^2(\pi V/2V_0)$ dependence. This has been shown to be the case experimentally. The reprint presented in this portion of Appendix D (pp. 133-134) describes experimental tests conducted to essentially bias-out the switch loss at t_{D2} (110 nsec on the T-beam). Since the switch loss (without a sonic bias) is a function of cell quality, pulse build-up time, pump energy, and perhaps even the electrode quality, the design approach will be to vary the sonic bias (with the quarter-wave voltage at the modulator) for the optimum Q-switched output from the resonator.

2. A time-dependent strain birefringence in the modulator causes a reduction in lasing efficiency unless a sonic bias is applied to null this effect. The sonic bias, in effect, drives the voltage across the modulator at Q-switching in such a way that the losses in the resonator at the time the pulse exits the resonator are minimal. This generally complicates the electronics requirements for driving the modulator and constitutes an additional variable for efficient Q-switching operation. This strain birefringence effect also increases the likelihood of double-pulsing and multiple-pulsing. (Double-pulsing is here defined as the emission of two or more pulses within a 100-nsec time interval, one pulse of which is the primary output pulse; multiple- (or after-) pulsing is defined as any output pulse regardless of amplitude or pulse width occurring more than 100 nsec after the primary output pulse). The Q-switching properties of the T-beam resonator were tested using the modulator drive circuit given in Appendix D-1. The variables considered in this investigation are shown in Fig. D.3-1 and are identified below:

a. V_{pc}: A modulator DC voltage prior to the modulator trigger pulse. The actual voltage across the modulator prior to $t(\phi_{pct})$ is $V_{pc} - V_{SB}$ since positive polarity voltages are applied to both modulator electrodes. At the time $t(\phi_{pct})$, the V_{pc} voltage is reduced to zero in a time interval of t_F.

b. V_{SB}: The sonic bias voltage used to compensate the strain-birefringent property of the modulator; the voltage across the modulator when V_{pc} goes to zero at $t(\phi_{pct})$.
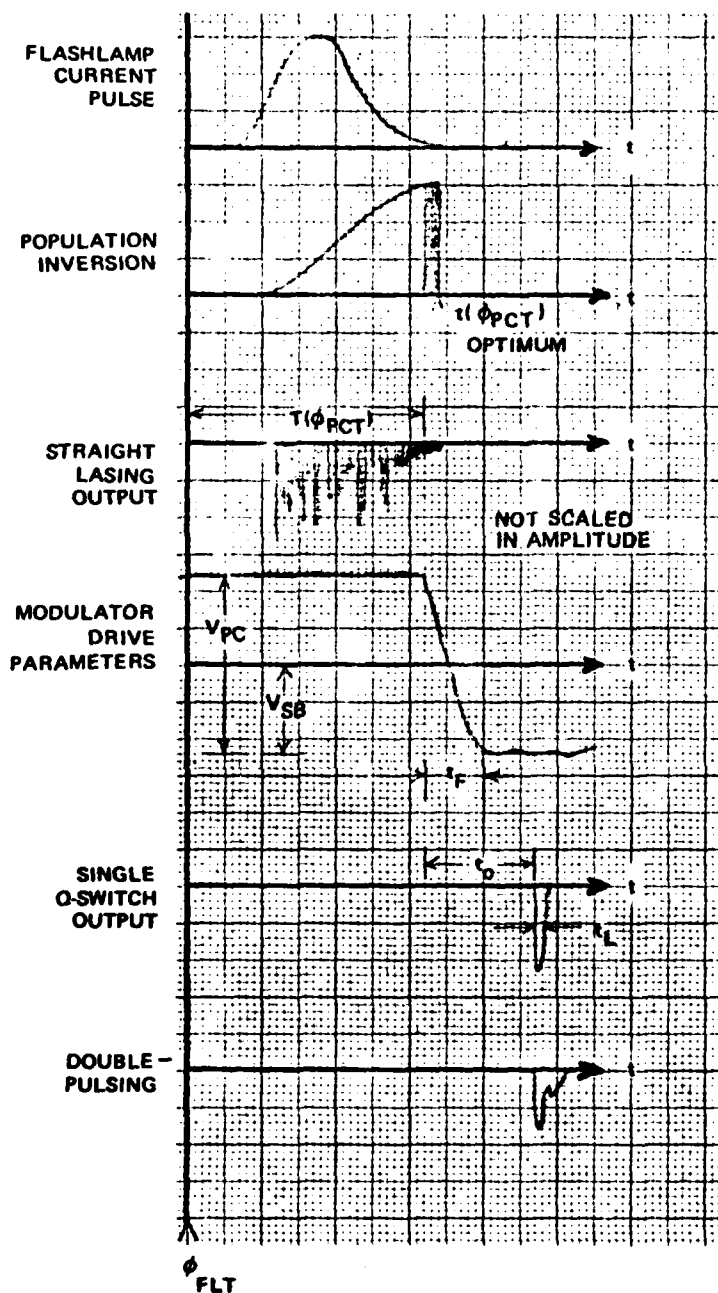
FIG. D.3-1.   Q-Switch Rate Parameters.

c. t_F: The fall time of the V_{pc} voltage. It was varied from 10 to 250 nsec by making a resistor change in the modulator drive circuitry.

d. t_D: The build-up time of the laser pulse--about 120 nsec.

e. t_L: The primary laser output pulse width at half-maximum signal amplitude.

f. $t(\phi_{pct})$:   The time delay from the flashlamp trigger pulse to the modulator trigger pulse, typically about 125 µsec.

Figure D.3-1 also shows the flashlamp current pulse (the light output intensity from the flashlamp is proportional to this current and lags it slightly), the population inversion in the laser rod (equivalent to stored energy), the time dependence of straight lasing if it were to occur, the modulator trigger pulse location with respect to this population inversion, and the optimum time of $t(\phi_{pct})$. The optimum $t(\phi_{pct})$ corresponds to the instant of maximum population inversion. If $t(\phi_{pct})$ is made appreciably shorter than the optimum delay, sufficient stored energy may remain available in the laser rod to cause secondary pulses. If $t(\phi_{pct})$ is made appreciably longer than the optimum value, the stored energy is less (due to its lifetime as an excited-state population); and the net possible output energy again is less. The time scale is roughly proportional up to time $t(\phi_{pct})$ and is about 5 µsec/div; after time $t(\phi_{pct})$, the scale is about 10 nsec/div. The ratio of the amplitude of the straight lasing signal to the Q-switched signal is about 10 mV:2V or about 200:1.

3.   It is reported in the open literature that as the Q-switch rate decreases (as t_F increases experimentally), the Q-switch output pulse width increases and finally for t_F, appreciably greater than t_D, afterpulsing occurs. It is also known that the Q-switch efficiency is high (non-Q-switched to Q-switched energy is nearly the same) as long as the Q of the resonator changes to its maximum value before the laser pulse build-up time, t_D, has elapsed. The particulars of the Q-switch loss function (i.e., how the Q is changed to its maximum level) are not of importance; but only low loss in the time interval t_D to $t_D + t_L$ is important. This is due to the fact that little energy is lost from the inverted population (stored energy) until after time t_D has passed. In terms of the variables described in the previous paragraph, the following experimental results were observed:

    a.   Early tests on the T-beam using the PADS electronics breadboard showed t_F = 200 nsec and t_L = 40 nsec. A faster trigger transformer was then tested having a t_F = 90 nsec which provided a 20-nsec output pulse width.

b. As t_F increases, the optimum amplitude of V_{SB} increases as well. This is consistent with the fact that the Q change that provides the lowest loss (highest Q) at time t_D will provide the most output energy.

c. For a fixed V_{SB} in the 500- to 800-V range, there is an allowable voltage range for V_{pc}. If V_{pc} becomes too small ($V_{pc} - V_{SB}$ much less than the quarter-wave voltage of the modulator), the laser goes to straight lasing due to inadequate holdoff. If the difference becomes too large, double-pulsing and/or after-pulsing occurs, depending upon the delay time $t(\phi_{pct})$. This allowed voltage interval for V_{pc} for fixed V_{SB} increases as $t(\phi_{pct})$ increases, as V_{SB} increases and as t_F decreases. Generally V_{pc} can be within 100 V of the condition that $V_{pc} - V_{SB} = 1,500$ V, the modulator quarter-wave voltage.

d. As V_{pc} is increased over the allowed voltage range, the output pulse width gets narrower, typically changing by a factor of two over the allowed voltage range. Beyond the upper allowable voltage limit of V_{pc}, a double-pulse of 40-nsec width is produced.

e. At $t(\phi_{pct})$, around 110 μsec and t_F much less than t_D, a V_{SB} less than 400 V will not prevent after-pulsing. If t_F and t_D are roughly equal, after-pulsing will always occur for all values of V_{pc} and V_{SB}.

f. The $V_{pc} - V_{SB}$ difference required to prevent straight lasing is near 1,400 V. This voltage in the PADS is anticipated to be about 1,450 V. If straight lasing occurs, this voltage difference must be increased.

g. The most reliable means of eliminating after-pulsing is to increase the time of $t(\phi_{pct})$.

h. When first turned on, the T-beam resonator starts out with straight lasing with a Q-switched pulse of reduced amplitude and incr ased width, typically, about 40 nsec. As the output energy increases due to the thermal alignment in the pump cavity, the pulse width reduces to near 20 nsec and straight lasing ceases. (This condition is also true in the LWL unit.)

i. If $t(\phi_{pct})$ is increased beyond about 135 μsec, only a single Q-switched pulse and straight lasing can occur regardless of the voltages V_{pc} and V_{SB}. The inverted population is not increasing after this time delay, and stored energy is not available for secondary pulses.

j. The most reliable means of removing double-pulsing is to reduce V_{pc} slightly (assuming that straight lasing is not occurring).

k. The after-pulsing may occur many microseconds after the primary pulse. This after-pulsing has a typical amplitude of 25:1 relative to the main pulse and may be as large as 200 nsec wide. An example of straight lasing and Q-switching with after-pulsing is shown in Fig. D.3-2.

Also included in that figure is a representative Q-switched output superimposed on the modulator voltage fall time t_F.
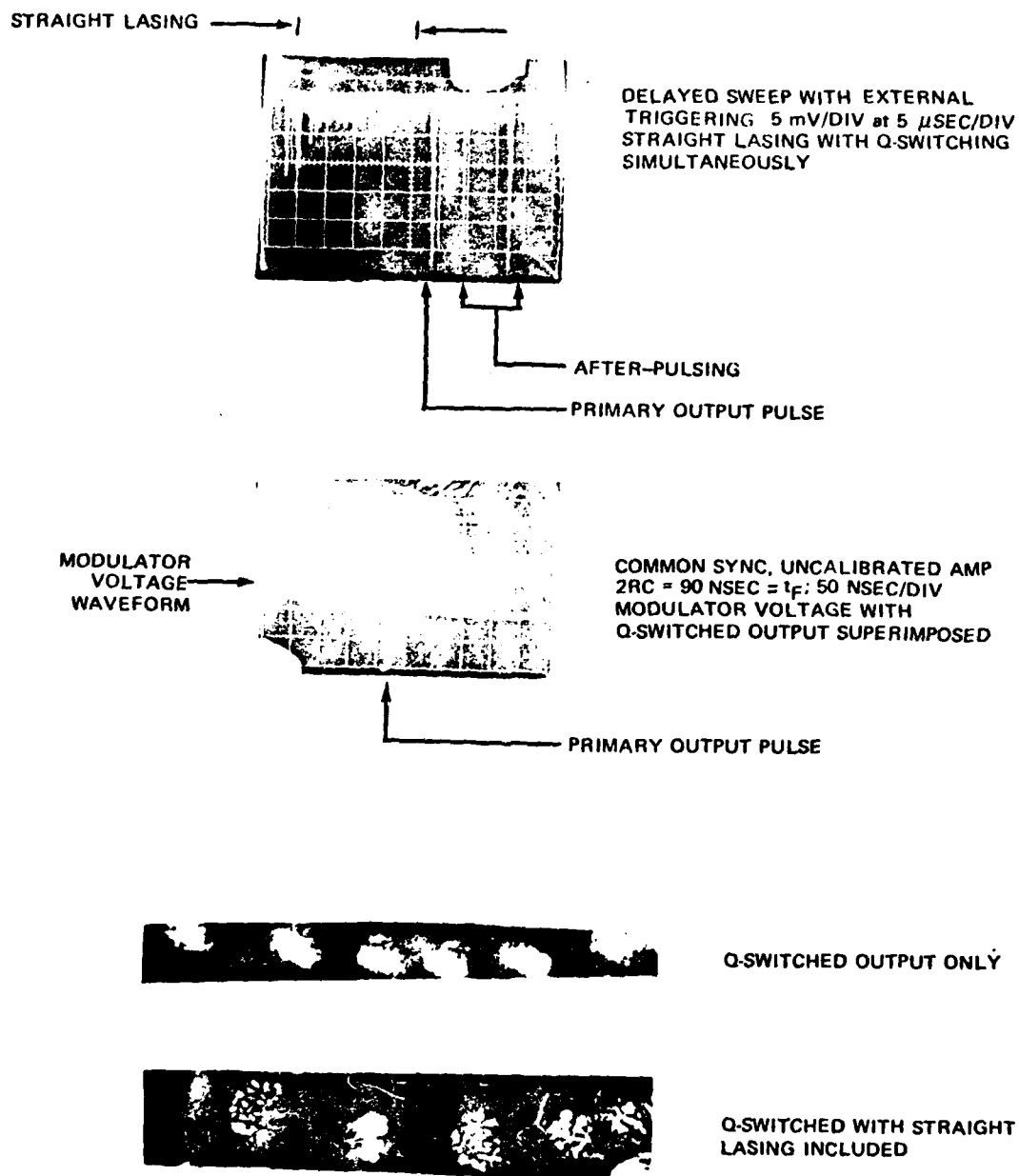
STRAIGHT LASING ———→|

DELAYED SWEEP WITH EXTERNAL
TRIGGERING 5 mV/DIV at 5 μSEC/DIV
STRAIGHT LASING WITH Q-SWITCHING
SIMULTANEOUSLY

AFTER–PULSING

PRIMARY OUTPUT PULSE

MODULATOR
VOLTAGE ———→
WAVEFORM

COMMON SYNC, UNCALIBRATED AMP
2RC = 90 NSEC = t_F; 50 NSEC/DIV
MODULATOR VOLTAGE WITH
Q-SWITCHED OUTPUT SUPERIMPOSED

PRIMARY OUTPUT PULSE

Q-SWITCHED OUTPUT ONLY

Q-SWITCHED WITH STRAIGHT
LASING INCLUDED

FIG. D.3-2. Q-Switching Behavior.

131

1. The Q-switched burn pattern provides an excellent means for determining whether straight lasing is occurring (together with the Q-switched pulse). The upper burn pattern in Fig. D.3-2 occurs when straight lasing does not occur. By a very slight reduction in V_{pc} to allow straight lasing, the lower burn pattern can be made to occur.

Details of the individual tests are available from the author. It should be noted that the PADS modulator drive circuit uses an SCR-transformer, rather than krytrons. The latter, however, allows direct variation of t_F, t_D, V_{pc}, V_{SB} and allows prediction of the operating characteristics of the former type of drive circuit.

NOTES:

1. The modulator drive characteristics vary somewhat from cell to cell because the extinction rates vary as does the insertion loss. As a result, the holdoff voltage ($V_{pc} - V_{SB}$) is lower for the better modulators.

2. *Straight lasing* is prelasing in terms of Q-switched operation. It is also called *threshold lasing* or normal pulsed lasing.

3. It is possible that prelasing and after-pulsing can occur simultaneously. The former is usually corrected by increasing the holdoff voltage, the latter by increasing the modulator trigger time delay or varying the sonic bias level.

4. With some reduction in laser efficiency, a pulse width of more than 30 nsec can be provided as output. This is about twice the pulse width of the normal case.

5. These tests were performed with a slightly damaged lithium niobate modulator. Subsequent tests have shown that prelasing may be a major cause of damage on the lithium niobate Q-switch modulator. Prelasing, if it occurs, allows a pulse buildup from a "seed" pulse, rather than from noise in a small region of the laser rod. This small region of the laser rod will have higher gain and lower order mode structure than the primary Q-switched pulse. Inadequate holdoff is the primary cause of prelasing.

References

1. R. Benumof, Amer. J. Phys. 33, 151 (1965).
2. R. L. de Zafra, Amer. J. Phys. 28, 648 (1960).
3. A. Messiah, *Quantum Mechanics* (Wiley, N.Y., 1962), Vol. 3, p. 740.
4. H. G. Dehmelt, Phys. Rev. 105, 1487 (1957).
5. H. G. Dehmelt, J. Opt. Soc. Amer. 55, 335 (1965).

Transient Elastooptic Effects and Q-Switching Performance in Lithium Niobate and KD*P Pockels Cells

R. P. Hilberg and W. R. Hook

TRW Systems, Redondo Beach, California 90278.
Received 24 April 1970.

It has been discovered that an elastooptic relaxation effect in a lithium niobate pockels cell seriously affects the efficiency of a Q-switched laser at higher power levels by creating a time dependent loss. A series of experiments has been made which measure this loss. KD*P has also been found to exhibit this effect. The purpose of this letter is to describe these effects, and to present a technique for eliminating this loss in a Q-switched laser.

Figure 1(a) shows a picture of a conventional Q-switched laser cavity which is normally Q-switched by applying a dc voltage to the Pockels cell and then switching that voltage to zero when the excited population density has reached a maximum. It has been found that the output energy of such a device rolls off at energy levels above a certain point, as shown in Fig. 1(b), whereas theoretically the output energy should be much higher, as also shown in Fig. 1(b). This roll-off loss is particularly bad with a laser using a lithium niobate modulator but it also occurs with a KD*P modulator. In our laboratory we performed a series of measurements which traced this problem to a mechanical relaxation effect within the modulator, rather than the more obvious laser rod superradiance. The first evidence we obtained to support this theory was that the entire amount of energy lost, as represented by E_2 of Fig. 1(b), was discovered to be coming out the loss direction from the polarizer, as shown by the E_2 arrow in Fig. 1(a). Thus the loss was clearly a residual birefringence effect of some kind.

Figure 2(a) shows a waveform picture of the voltage conventionally applied to a Pockels cell, and Fig. 2(b) shows the loss vs time for an actual Pockels cell switch, where the loss is defined as the ratio of the power deflected out of the cavity [P_2 in Fig. 1(a)] to the power approaching the switch (P_1). This loss must be very low for good lasing efficiency. The loss is supposed to be high during the excited population buildup interval and then it is supposed to drop rapidly to zero. Instead, as shown in Fig. 2(b), it was found that the loss drops to about 25% and then decays to zero in approximately 400 nsec. At low input energy levels there is a long time delay (large T_D) between the switching time and the time the output pulse actually appears, as shown in Fig. 2(c), and thus there is negligible loss in efficiency. However, at higher input energy levels the time delay T_D becomes shorter and thus the laser suffers a considerable output loss due to the switch loss, as shown in Fig. 2(d). This accounts for the roll-off in output efficiency in the Q-switched laser at higher input energy levels.
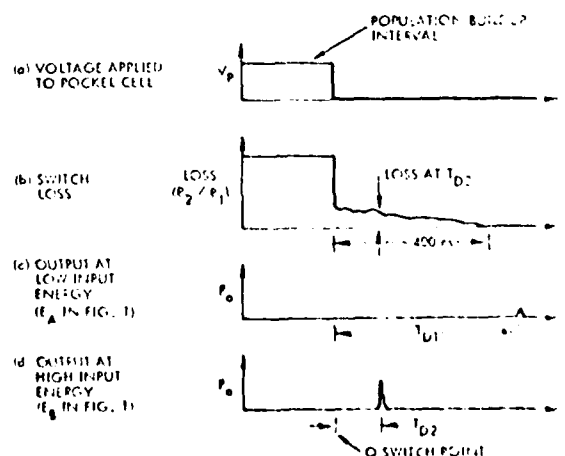
It is believed that the piezoelectric action of the applied voltage V_P compresses the crystal and when that voltage is removed the crystal remains compressed for some definite interval of time. This compression generates a retardation of the optical wave by means of a strain-birefringence effect, thus creating a loss in the

cavity which gets less with time as the compression relaxes, as shown in Fig. 2(b). This effect is quite pronounced in lithium niobate but can also be easily measured and observed in KD*P. This loss may be termed an elastooptic loss since it results from a mechanical compression of the crystal in the absence of an external applied voltage.

Data for the switch loss curve of Fig. 2(b) were obtained in the following way. The lithium niobate modulator was set between uncrossed polarizers, and a TRW 71A 30-μsec pulsed argon gas laser was used as the signal source. The transmitted signal was detected using an ITT FW114A S-20 photodiode. The voltage applied to the niobate modulator was switched from the ½-wave retardation voltage to zero in about 10 nsec using an E.G. & G. KN 22 krytron. The actual transmission curves so obtained are shown in Figs. 3(a) and 3(b) for 100 nsec/cm and 1 μsec/cm time scales, respectively. It was found that the effect could be more easily observed and measured if the retardation voltage was

(a) Q-SWITCHED LASER CAVITY; LOSS = P_2/P_1

(b) Q-SWITCHED LASER PERFORMANCE
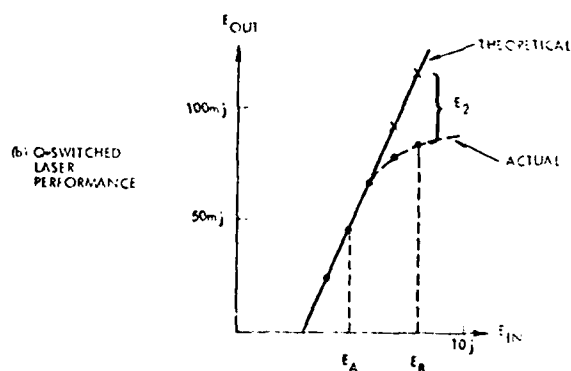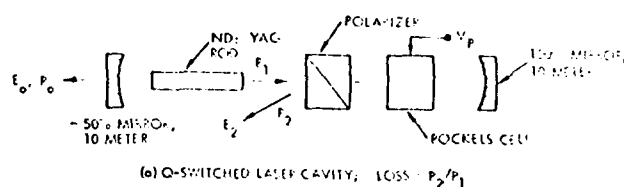
Fig. 1. Conventional Q-switched laser and its performance. The cavity is 46 cm long, and employs a 6.4 mm × 76 mm attron Nd:YAG rod.

(a) VOLTAGE APPLIED TO POCKEL CELL

(b) SWITCH LOSS

(c) OUTPUT AT LOW INPUT ENERGY (E_A IN FIG. 1)

(d) OUTPUT AT HIGH INPUT ENERGY (E_B IN FIG. 1)

Fig. 2. Basic waveforms. The output pulse width is 20 nsec at $E_{in} = E_B$.

(a) LITHIUM NIOBATE, 100 ns/cm; SWITCHING TO ZERO VOLTS

(b) LITHIUM NIOBATE 1 μsec/cm; SWITCHING TO ZERO VOLTS

(c) LITHIUM NIOBATE, 100 ns/cm; SWITCHING TO THE 1/4 WAVE VOLTAGE

(d) LITHIUM NIOBATE, 1 μsec/cm; SWITCHING TO THE 1/4 WAVE VOLTAGE

(e) KD*P, 100 ns/cm; SWITCHING TO THE 1/4 WAVE VOLTAGE

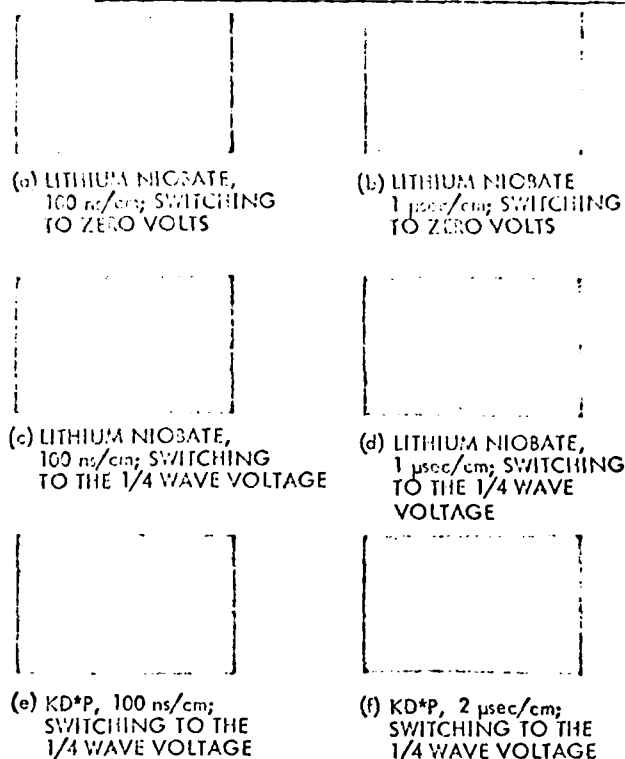(f) KD*P, 2 μsec/cm; SWITCHING TO THE 1/4 WAVE VOLTAGE

Fig. 3. Measured transmission waveshapes. The lithium niobate modulator has a 9 mm × 9 mm cross section, 10-mm length, with transverse field modulation. The KD*P modulator is a 2.5-cm cube with longitudinal modulation applied with ring electrodes.
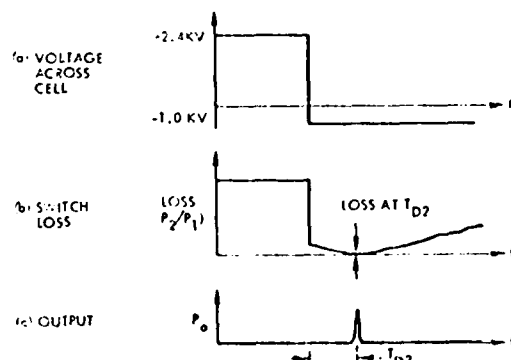

Fig. 4. Waveforms obtained with biasing. The output pulse width is 20 nsec.

switched to an intermediate value instead of to zero. Figures 3(c) and 3(d) show results when switching from the ¼-wave voltage to approximately half that voltage, giving a steady-state transmission of ~50%. Notice that the crystal undergoes what is certainly an acoustic oscillation with a period of about 3 μ-sec. The characteristics of this ringing may be of general interest to those contemplating the use of Pockels cell switching, although it is only the initial relaxation that concerns the Q-switch designer. A similar set of pictures was obtained with a KD*P modulator, as shown in Figs. 3(e) and 3(f). Here the initial compression creates a retardation having the opposite effect to that for the niobate.

The above results were substantially independent of the voltage-switching (fall) time over a range of 5–100 nsec.

For Q-switching applications the loss can be eliminated by applying an electrical bias to the cell to null the mechanically generated retardation. This bias voltage can be most easily applied to the normally grounded electrode of the modulator. For lithium niobate a positive voltage is required, whereas for KD*P a negative voltage is used. The net voltage across the Pockels cell has the wave shape shown in Fig. 4(a) for niobate. With the use of this technique the theoretical output efficiency shown in Fig. 1(b) has been achieved, as indicated by the crosses; in these tests, the bias was changed for each input energy level in order that the switch loss was always a minimum for that laser buildup time delay (T_D) corresponding to each input energy (E_{in}), as shown in Figs. 4(b) and 4(c). The efficiency of a Nd YAG Q-switched laser is relatively insensitive to small changes in this bias level.

Performance Characteristics of a Small TGS Detector Operated in the Pyroelectric Mode

F. Schwarz and R. R. Poole

Barnes Engineering Company, Stamford, Connecticut 06904.
Received 13 May 1970.

A number of room temperature operated, small area pyroelectric infrared detectors were recently fabricated and evaluated with results considered to be quite remarkable for thermal de-
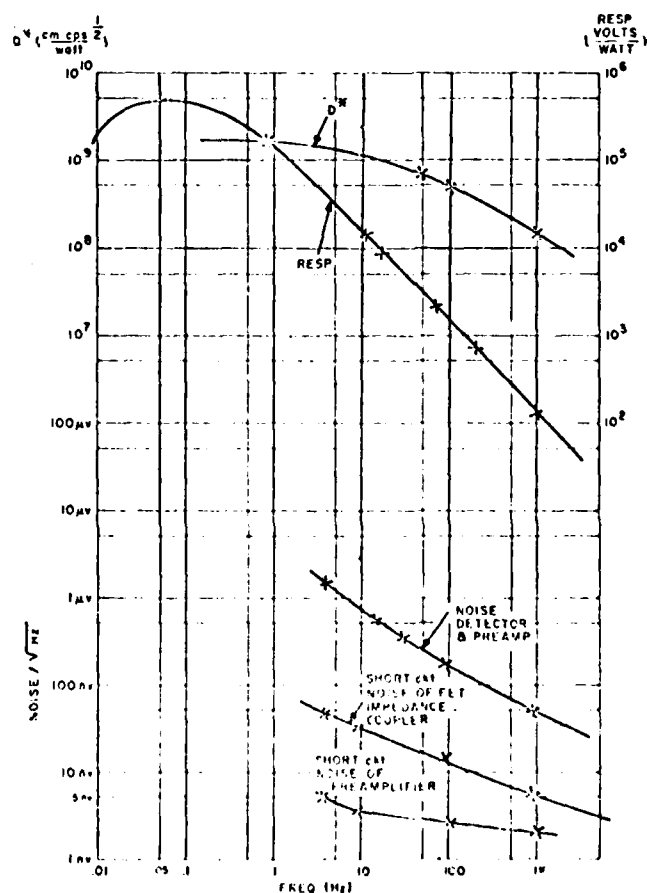

Fig. 1. Performance curves, 0.4 mm × 0.7 mm, pyroelectric detector.

134

Appendix F

RESONATOR OUTPUT PROPERTIES

Appendix E-1

MULTIPLE-BEAM OUTPUT FROM T-BEAM

1.   Secondary output beams from the resonator could contain sufficient energy which may cause false signal returns in field usage. Hence, it is important to measure the energy content of the secondary output beams that are present, establish their source and cause and, if possible, remove them as resonator output. The purpose of this portion of Appendix E is to interpret these secondary output beams in the T-beam resonator and provide guidelines to prevent their reoccurrence.

2.   When the PADS resonator was in preparation, the author observed five secondary output beam spots. The energy content in these secondary beams was 0.26, 0.76, 0.75, 0.62, and 0.93% of the primary resonator output. The present quarter-wave plate has a high insertion loss (due to surface reflectance). It became evident during tests that three of the secondary output beams were due to the quarter-wave plate and had a total energy content of 2.31% of the primary output beam. By misaligning the surface reflection from the quarter-wave plate relative to the resonator axis, these three secondary beams were eliminated.

3.   A fourth secondary beam (of 0.26% energy content) was found due to the calcite prism surface reflectance. Since this secondary beam does not exit the resonator by means of the dump mirror, it will not be seen as output energy unlike the other secondary beams observed.

4.   The fifth secondary beam was due to vignetting of the resonator axis by the dump mirror. As a result, the dump mirror was moved outward slightly for clearance, and so the final secondary beam was eliminated as resonator output. The fact that no secondary beam was evident from the end fold or dump mirror suggests high reflectance for all of these optical components.

5.   Since the quality of the LWL and present PADS quarter-wave plate are similar, it seems highly probable that the secondary beam observed from the LWL resonator can be removed by canting the quarter-wave plate slightly relative to the resonator axis.

Appendix E-2

T-BEAM OUTPUT ENERGY WITH TEMPERATURE

1. The T-beam resonator has been thermally tested from 0 to 120°F. The tests were arranged so that performance degradation over the temperature range could be attributed to the pump cavity or the T-beam itself. Output energy and pulse-to-pulse amplitude stability were the output variables measured. The purpose of this memorandum is to describe the tests and their results.

2. The T-beam was mounted in a temperature-controlled oven. The cooling system (using FC-104 coolant) and the flashlamp drive circuitry were outside the oven. The non-Q-switched resonator was operated at 10-Hz rate with an input energy of 8 J/pulse. A single mounting bolt was used to hold the T-beam which was placed so that its output went through a conveniently available aperture in the oven wall to an EG&G radiometer. The use of a single-mounting point ensures that no thermal stresses were induced into the T-beam because of the mounting structure itself. Copper-constantan thermocouple wires and a thermocouple chart recorder were used to record temperature and temperature changes at critical points. Thermocouple wires were placed in the coolant lines to record the temperature gradient in the laser head.

3. The results of the temperature tests can be summarized as follows:

    a. Regardless of the operating temperature used, the temperature gradient in the pump cavity is approximately 3.5°F.

    b. At increased temperatures up to 120°F, the energy output degradation is less than 5% and the pulse-to-pulse amplitude stability variation is only 5.5% as compared to 4% at room temperature. The T-beam resonator was tuned for optimum efficiency at room temperature.

    c. At temperatures below room temperature down to 0°F, the output energy and pulse-to-pulse amplitude stability degradation is approximately 4% per 15°F temperature change.

    d. The laser rod coolant-seal leaked at low temperatures but the starting temperature is not known. As a result, as little at 50% of the output energy degradation noted above may be due to thermal misalignment of the T-beam itself. (This is explained by the fact that, upon returning to ambient temperature from 0°F, the output energy increased only 10% because of coolant contamination of an end face of the laser rod.)

    e. The pulse-to-pulse amplitude stability variation with temperature is more a characteristic of the pump cavity design and the coolant used

137

than of the T-beam structural performance. For example, at elevated temperatures, FC-104 is one-tenth as efficient as EGw as a coolant for heat removal from the pump cavity. The net result is that the temperature gradient would be appreciably lower in the pump cavity if EGw coolant were used. Unfortunately, time did not permit tests using alternate coolants or coupling geometries.

f. Design effort is needed to correct the coolant leak problem (which was present with the PD at low temperatures as well).

4. In summary then, the T-beam by itself has excellent thermal stability. The thermal stability of an integrated T-beam resonator is, of course, strongly dependent on the thermal behavior of the electro-optical and mechanical interface as well. Output energy degradation and pulse-to-pulse amplitude stability degradation with temperature in excess of those established above must be attributed to these interface thermal characteristics.

NOTES:

1. The T-beam was mounted by a single bolt to an insulator. The T-beam ends were free to move and the mounting point was near the T-beam center.

2. The coolant leak problem is associated with the laser rod O-ring seal which is presently designed so that it supplies the coolant seal at two surfaces rather than only one as is customary.

3. The T-beam resonator used one flat end mirror and one 10-meter (radius of curvature) end mirror. On the basis of the output degradation with temperature and the mirror misalignment sensitivity of Appendix A-5, it is apparent that the resonator was misaligned approximately 10 arcsec at 0°F.

4. To ensure that the system temperature had stabilized at various operating temperatures, the cooling system was operated continuously and thermocouples monitored component, coolant, and oven temperatures continuously and plotted these temperatures on a thermocouple recorder printout.

Appendix E-3

RAW-BEAM DIVERGENCE MEASUREMENTS

1. Figures E.3-1 through E.3-4 show the raw-beam divergence data for both a 10-meter (radius of curvature) end mirror and a flat end mirror used in conjunction with a 70% reflecting, flat end (dump) mirror at both 10 pps and 1 pps with an 8.5-J input energy. In all, 16 component combinations were tested and are plotted in groups according to their similarity in raw-beam divergence. Table E.3-1 shows the difference in energy output (in relative units) at 10 pps for the various resonator component combinations at an input energy of 8.5 J. (One unit corresponds to an energy output of approximately 125 mJ.) The raw-beam divergence data taken at 1 pps were derived from oscilloscope voltage readings with the resonator tuned for 1 pps operation, so that its output energy per pulse was equal to that which was present at the 10-pps rate. Figure E.3-5 shows the raw-beam divergence dependence on input energy for the two combinations of resonator components given. This figure indicates that the raw-beam divergence generally increases with input energy at a rate of approximately 0.2 mrad/J independent of the flashlamp type used since the curve slopes are parallel and therefore equal. These data also allow a means of normalizing the raw-beam divergence data of Fig. E.3-1 through E.3-4 due to the differences in energy output (shown in Table E.3-1) by using the radiometer current readings shown plotted in Fig. E.3-5. For an equal energy output level then, Table E.3-1 shows also the anticipated raw-beam divergence at 10 pps for various resonator component combinations.

TABLE E.3-1. Relative Energy Output and Raw-Beam
Divergence at a Fixed Output for Various
Component Combinations

Flashlamp type	Resonator components			
	10-m/Cyl^a	10-m/EwI^b	Flat/Cyl^c	Flat/EwI^d
Relative data:				
Xenon	1.27	1.06	1.10	1.00
Krypton	1.55	1.29	1.44	1.25
Raw-beam divergence, mrad:				
Xenon	3.43	3.65	2.52	2.67
Krypton	3.35	3.60	2.30	2.60

a 10-m end mirror and cylindrical pump cavity shape.
b 10-m end mirror and elliptical pump cavity shape.
c Flat mirror and cylindrical pump cavity shape.
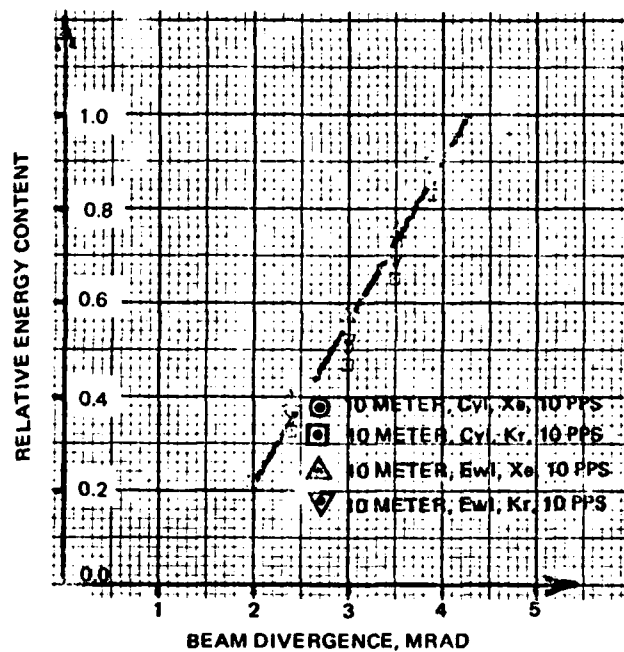d Flat mirror and elliptical pump cavity shape.

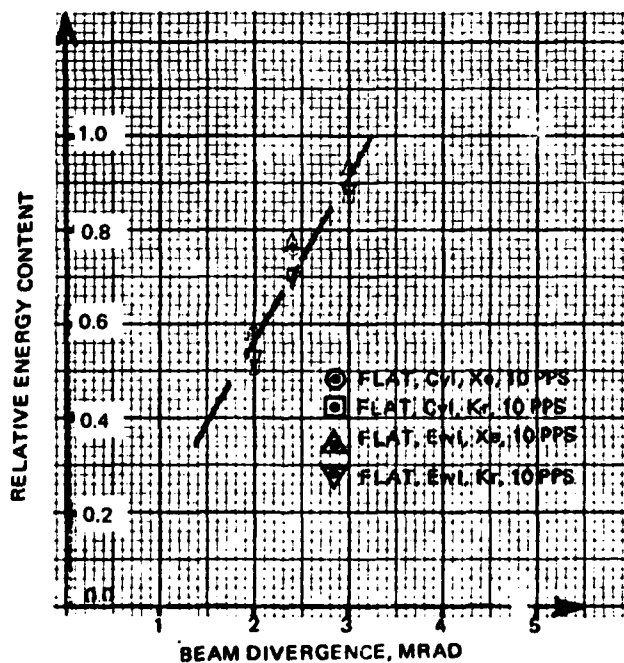FIG. E.3-1. Raw-Beam Divergence Data.

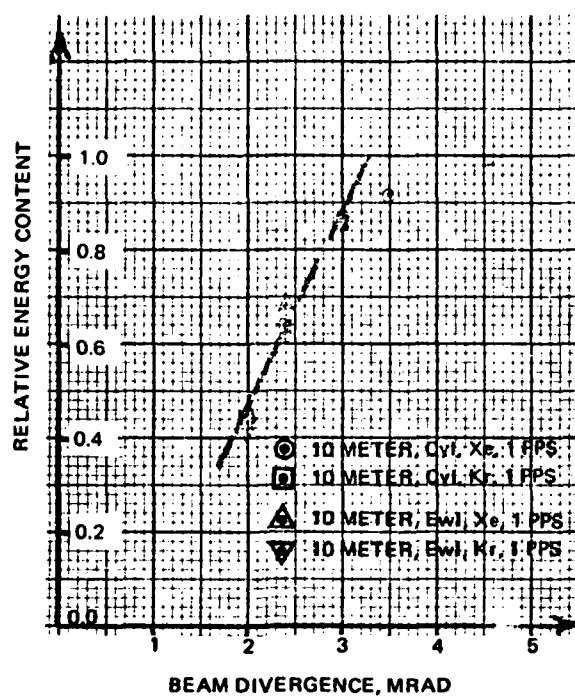FIG. E.3-2. Raw-Beam Divergence Data.

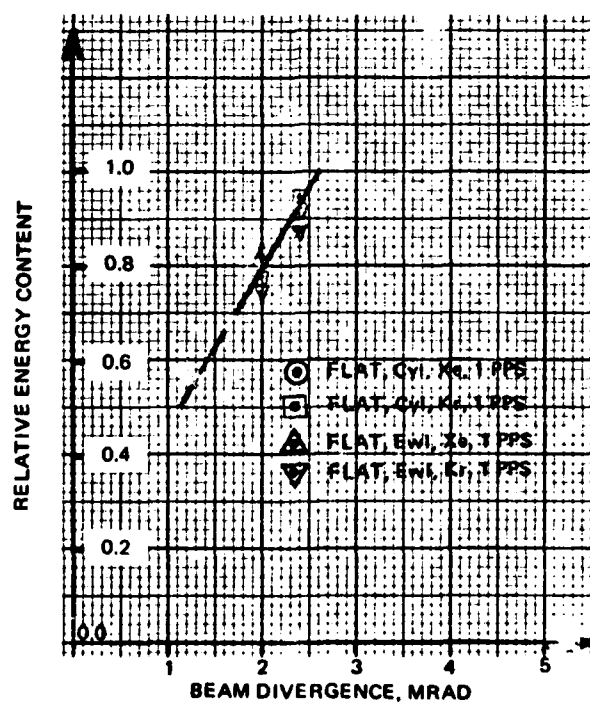FIG. E.3-3.   Raw-Beam Divergence Data.

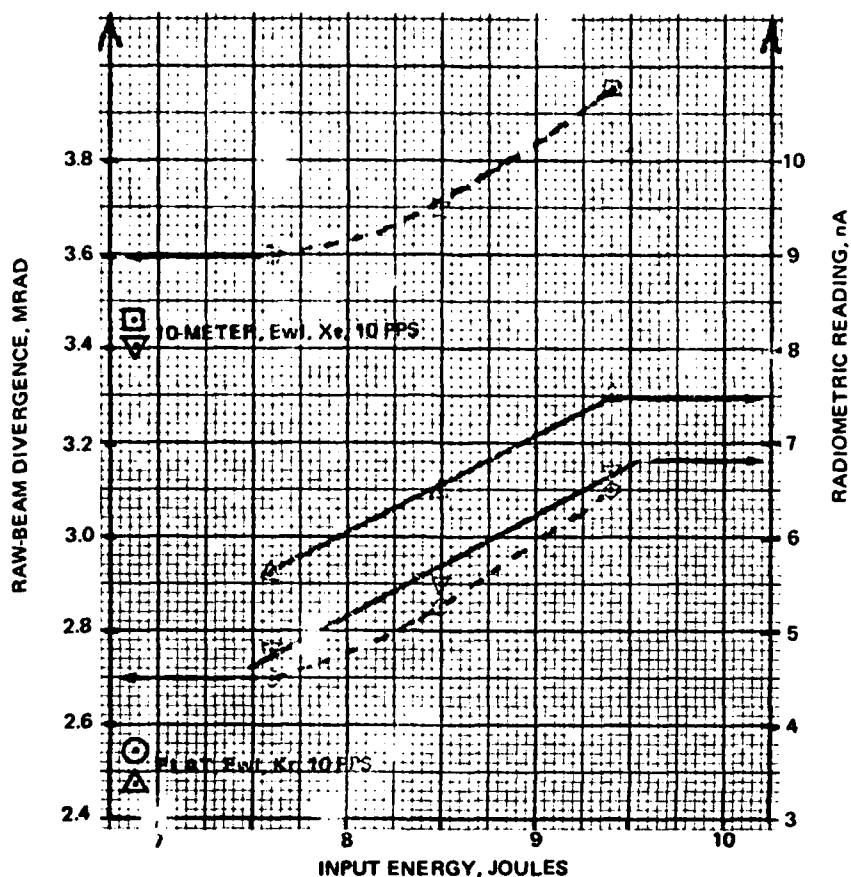FIG. E.3-4.   Raw-Beam Divergence Data.

FIG. E.3-5. Raw-Beam Divergence Dependence
With Input Energy at 10 PPS.

2. From the data of Table E.3-1 it can be concluded that

  a. For a fixed end-mirror curvature and pump cavity shape, krypton-
filled flashlamps provide approximately 25% more output energy than do
xenon-filled flashlamps.

  b. For a fixed end-mirror curvature and flashlamp type, a cylindri-
cal pump cavity shape is 10-20% more efficient than is an elliptical pump
cavity with inserts.

  c. For a fixed flashlamp type and pump cavity shape, a 10-meter
end mirror provides about 5-15% more output energy than does the use
of a second flat end mirror.

  d. A xenon flashlamp used in conjunction with flat end mirrors and
an elliptical pump cavity with inserts is expected to have about 50%
less output energy than would a krypton-filled flashlamp used in con-
junction with a 10-meter end mirror in a cylindrical pump cavity at an
8.5-J input energy level.

The krypton-filled flashlamp (KG4) had a fill pressure of 1,500 torr. Due to the difficulty in triggering flashlamps at this fill pressure, krypton flashlamps at a fill pressure of 1,000 torr have been procured and are anticipated to be slightly less efficient but more usable.

3. From the data of Fig. E.3-1 through E.3-4 and Table E.3-1 it can be concluded that

   a. Regardless of end-mirror curvature selection or pump cavity shape used, krypton-filled flashlamps provide only a slightly better raw-beam divergence than xenon-filled flashlamps.

   b. For a fixed end-mirror curvature and flashlamp type, the cylindrical pump cavity provides a slightly better raw-beam divergence than the elliptical pump cavity with inserts.

   c. The raw-beam divergence is relatively independent upon both the pump cavity shape and the flashlamp type used.

   d. For a given end-mirror curvature, the raw-beam divergence at 10 pps is approximately 30% higher than it is at 1 pps for an 8.5-J input energy level.

   e. At a fixed repetition rate, changing from a 10-meter (radius of curvature) end mirror to flat end mirrors decreases the raw-beam divergence by about 30%.

   f. The flat end mirror/raw-beam divergence figure at 10 pps is nearly the same as the 10-meter end-mirror/raw-beam divergence figure at 1 pps.

   g. Similarity in the uniform lasing and scan diameter for both cylindrical and elliptical pump cavities with inserts showed no repeatable difference in the output beam character, and hence no difference in output raw-beam divergence was expected. (See Appendix F-1.)

NOTES:

1. The raw-beam divergence data are for 85% energy content. Fixed apertures of varying sizes were used in the focal plane of a 48.5-inch focal length lens.

2. Scale-model diagrams of the cylindrical and the elliptical pump cavities with inserts are shown in the publication identified in Appendix F-2.

3. The same Nd:YAG laser rod was used for all these tests on raw-beam divergence. The laser was operated non-Q-switched for these tests.

Appendix E-4

SEMIEMPIRICAL EQUATION DESCRIBING THE RESONATOR RAW-BEAM DIVERGENCE

1. Beam divergence and output energy are the two most important output properties of a laser resonator. Hence the major emphasis in the laser lab effort has been toward optimizing lasing efficiency and increasing our understanding of resonator properties as they pertain to raw-beam divergence. Table E.4-1 very briefly summarizes the experimental results as they apply to resonator thermal effects and raw-beam divergence. The purpose of this portion of Appendix E is to show the derivation of a semiempirical equation consistent with these past experimental results and which correctly predicts the raw-beam divergence from a laser resonator due to changes in the resonator input properties including pump energy and pulse repetition rate. It also predicts the dependence of end reflector curvature, laser rod quality, and resonator length and diameter.

2. The optical path length P in any medium is given by the product of the index of refraction and the physical path length, namely,

$$P = n\ell \qquad \frac{dP}{dT} = \ell\frac{dn}{dT} + n\frac{d\ell}{dT} = \ell\frac{dn}{dT} + n\alpha\ell \qquad (1)$$

and directly, a difference in optical path length due to a difference in temperature along two paths is given by the equation

$$\Delta P = [n\alpha + (\Delta n/\Delta T)]\ell\Delta T \qquad (2)$$

where

$n = 1.82$ (index of refraction of the laser rod)

$\alpha = \ell^{-1}d\ell/dT = 6.9\,(10)^{-6}\,°C^{-1}$ (linear expansion coefficient of YAG)

$\Delta n/\Delta T = 7.3\,(10)^{-6}\,°C^{-1}$ (index of refraction change with temperature) *Cnst?*

$\ell = 7.62$ cm (length of the laser rod)

ΔT in °C (temperature difference between paths being compared)

Note that $n\alpha$ is about twice as large as $\Delta n/\Delta T$ so, under conditions where the laser rod length is free to change, the optical path length difference (say centered along the laser rod axis as compared to a parallel path near the laser rod edge) is about 60% due to a physical path-length difference and 40% due to an index of refraction difference. As a result, it is expected that if an optical path-length variation occurs due to flashlamp pumping, a thermal lensing effect on the laser rod end faces should be perceptible. Yet tests conducted earlier

TABLE E.4-1. Beam Divergence Results Summary and Reference.

Reference	Results and implications
Reg 4051-195-71 (Appendix C-1)	1. End-face curvature (lensing) of the laser rod is negligibly small due to flashlamp pumping of the laser rod. 2. TRW IOC 7242.4-517 is limited in describing the laser resonator raw-beam divergence figure.
Reg 4051-206-71 (Appendix F-1)	1. Non-Q-switched output beam uniformity varies only slightly with the end reflector type, resonator alignment quality, and pump cavity geometry. 2. The direction of resonator misalignment is predictable on the basis of the Polaroid burn pattern uniformity and shape.
Reg 4051-209-71 (Appendix E-3)	1. Raw-beam divergence generally increases with input energy at about 0.2 mrad/J 2. Flashlamp type has a negligible effect on the beam divergence figure. 3. The raw-beam divergence at 10 Hz is about 30% larger than at 1 Hz regardless of the end reflector curvature used. 4. Thermal distortion is misaligning the resonator by about 20 arcsec using the FC-104 coolant. 5. The coolant flow rate appears to have a relatively small effect on the raw-beam divergence figure.
Reg 4051-226-71 (Appendix C-2)	1. The laser rod absorbs about 5% of the stored capacitor energy. 2. Nonuniform coolant flow creates a transverse thermal gradient in the laser rod which produces a thermal distortion. 3. The axial thermal gradient does not appear to contribute significantly to the thermal distortion of the resonator laser rod. 4. Coolant entrance port design is not critical with a coolant such as EGw. 5. A new pump cavity design should be undertaken.

TABLE E.4-1. (Contd.)

Reference	Results and implications
Reg 4051-107-72 (Appendixes A-7 and C-4)	1. The raw-beam divergence at a particular input power is different for several rods due to differences in their optical quality. 2. Regardless of rod quality, the raw-beam divergence increases about 0.7 mrad when the pulse repetition rate goes from 1 Hz to 10 Hz using FC-104 coolant. 3. An increased coolant flow rate will not appreciably improve the raw-beam divergence figure with repetition rate nor will it readily correct the thermal misalignment problem associated with the use of FC-104 coolant.
Reg 4051-115-72 (Appendix C-4)	1. The raw-beam divergence is relatively independent of the coolant mass flow rate. 2. The thermal distortion in terms of a fringe count is relatively insensitive to coolant mass flow rate. 3. The absorbed flashlamp radiation, not the thermal properties around the laser rod, appears to be the major cause of the beam divergence increase with pump power.
Reg 4051-119-72 (Appendix C-4)	1. The raw-beam divergence increase with input power is relative. independent of the axial thermal gradient in the pump cavity. 2. The raw-beam divergence increases about 0.7 mrad in going from a 1-Hz to a 10-Hz pulse repetition rate using EGW or water coolant.
Reg 4051-122-72 (Appendix C-5)	1. The radial thermal gradient in the laser rod is about 0.5°C and is dependent only upon the input power and laser rod properties.
Reg 4051-126-72 (Appendix C-6)	1. Most of the radial thermal gradient is due to nonradiative transitions in the dopant impurity ion. *nonradiative transitions!*

showed that no noticeable laser rod end-face lensing occurred. Open literature (APPLIED OPTICS, Vol. 9 (1970), p. 2548) shows that the thermal gradients in the laser rod further than about the rod radius from its ends do not contribute to the elongation of the laser rod. This in effect means that the $n\alpha\ell\Delta T$ in Eq. 2 should be replaced approximately by $n\alpha r_0 \Delta T$, where r_0 is the rod radius. Measurements of rod end-face curvature showed this to be true for a high input power cw Nd:YAG laser. This behavior was attributed to the fact that the laser rod is under compression due to a radial thermal gradient. Figure 5 in APPLIED OPTICS, Vol. 9 (1970), p. 1429, shows that the rod center is indeed under compression (due to the negative sign of the stress coefficient).

3. As a result then, it should be written that the optical path length difference along two separate paths in a laser rod is given approximately by

$$\Delta P = \ell(\Delta n/\Delta T)\Delta T \qquad (3)$$

Appendix C-5 shows calculations of an optical path length difference (measured axially along the rod axis center as compared to along its edge due to a predicted radial thermal gradient) of 0.65λ at 1.06μ using Eq. 2 in this portion of Appendix E and shown here to be in error. Eq. 3 yields

$$\Delta P = 0.235\lambda \text{ at } 1.06\mu$$

i.e., about one-quarter of a wavelength. Appendix C-2 shows that there exists a transverse thermal gradient in the laser rod due to nonuniform cooling of the laser rod by the FC-104 coolant. Appendix C-2 shows that the thermal distortion fringe count with input energy has each fringe having a slight curvature. Suppose now that a radial thermal gradient corresponding to an optical pathlength difference of 0.25λ is superimposed on a transverse thermal gradient corresponding to an optical pathlength difference of 1.5λ. The effect (grossly exaggerated) is shown in Fig. E.4-1. The fringe diagram at the left is that which would appear if only a transverse thermal gradient were present in the laser rod. The fringe diagram at the right in Fig. E.4-1 is that expected due to a superposition of a small thermal gradient which is radial to a larger transverse thermal gradient. The net result of this superposition on the observed interference fringes is precisely that which is observed experimentally; namely, interference fringes with slight curvature to them. Hence, Eq. 3 is in agreement with the experimental results. The transverse thermal gradient, whether due to an index of refraction difference, or a length difference, or a combination of the two, produces only an effective misalignment of the resonator and has no focusing properties. It is necessary now to calculate the thermal focusing effect produced by this radial index of refraction variation.

λ /4 IN OPTICAL PATH

ROD END VIEW

HOT

INTERFERENCE FRINGE DIAGRAM

TRANSVERSE AND RADIAL THERMAL GRADIENTS SUPERIMPOSED

λ /2 IN OPTICAL PATH

δT

(COLI)

EFFECT OF TRANSVERSE GRADIENT

EFFECT OF RADIAL TEMP GRADIENT

ROD END VIEW

INTERFERENCE FRINGE DIAGRAM
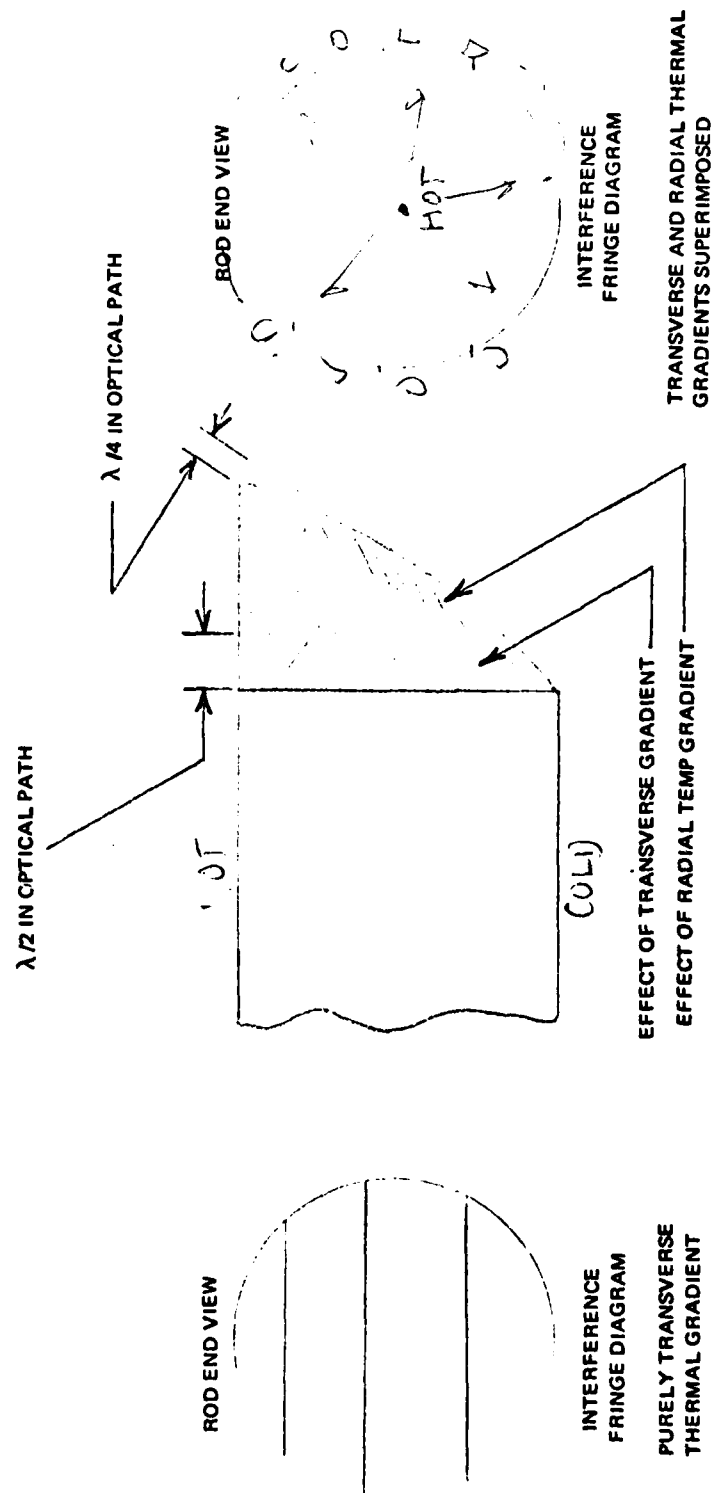
PURELY TRANSVERSE THERMAL GRADIENT

FIG. E.4-1. Fringe Diagrams Due to Thermal Gradients.

4. Extremely high pump powers were used in early ruby and Nd:glass laser systems. These lasers were necessarily operated at low repetition rates. In such cases, the thermal gradient in the laser rod is purely radial or very nearly so. The relatively poor thermal conductivity of these host materials also contributed greatly to this radial thermal gradient. As a result an optical theory was developed describing the focusing properties of a lenslike medium having a refractive index gradient which is parabolic (or as the radial thermal gradient would be). It was shown that, with some approximations, the focal length of such a lenslike medium can be written as

$$f = 2K/\ell h(\Delta n/\Delta T) \tag{4}$$

where

$K = 26.5 \ (10)^{-3}$ cal/cm-sec-°C (thermal conductivity of YAG)

$\ell = 7.62$ cm (length of the laser rod)

h in cal/sec-cm³ (power absorbed by the laser rod per unit volume)

f in centimeters (focal length of the lenslike medium (here), the rod)

The author showed in Appendix C-2 by applying Huygen's principle that if there is an optical path length difference of one wavelength (i.e., $\Delta P = \lambda$) for two paths separated by a distance a, the focusing effect produced by this path-length difference is equivalent to a lens of focal length

$$F = a^2/2\lambda \tag{5}$$

If Eq. 4 and 5 are both correct, then $f = F$ must be true, which is shown below. Recall from the earlier discussion that

$$\Delta P = \ell(\Delta n/\Delta T)\Delta T \tag{6}$$

and in Appendix C-5 the author showed that the laser rod radial thermal gradient is given by

$$\Delta T = \eta P_{in}/4\pi K\ell \tag{7}$$

By direct substitution into Eq. 5, where a is now the rod radius r_o, it follows that

$$F = r_o^2/2\Delta P = r_o^2 \ 2\ell(\Delta n/\Delta T) \ X \ 4\pi K\ell \ \eta P_{in}$$

$$= 2K/\ell(\Delta n/\Delta T)(\eta P_{in}/\pi r_o^2 \ell) \tag{8}$$

149

But ηP_{in} is the power absorbed by the laser rod and $\pi r_o^2 \ell$ is its volume, so then

$$h = \eta P_{in}/\pi r_o^2 \ell \qquad\qquad\qquad (9)$$

and $f = F$ exactly. Upon substitution of the variables, it follows directly that

$$F = 1785/P_{in} = 1785/E_{in}\tau \qquad\qquad (10)$$

where

P_{in} = input pump power, W

E_{in} = input energy/pulse, J

τ = pulse repetition rate, Hz

η = 5%, and F is in meters

An effective focal length of the laser rod is now available as a function of the input pump power or as the product of input energy per pulse and the pulse repetition rate in Hz.

5. It is published in the open literature that a resonator containing lenses with an equivalent focal length, F_{eq} has an output raw-beam divergence, ϕ, no larger than

$$\phi = D/\left(LF_{eq}\right)^{\frac{1}{2}} \qquad\qquad\qquad (11)$$

where

D = lasing diameter, and

L = resonator length

This equation applies when $F_{eq} \gg L$ holds true. Unfortunately this equation (which puts only an upper bound on the raw-beam divergence figure) does not describe the resonator beam divergence using flat-end reflectors ($F = \infty$), the dependence of the input power level, the pulse repetition rate, or the dependence of laser rod quality. It also assumes a homogenous and isotropic lasing medium which is not true due to the thermal effects produced by flashlamp pumping of the laser rod. It becomes obvious then that a new equation is needed incorporating all these raw-beam divergence dependent parameters. The major factors leading the author to the final form of such an equation were as summarized:

a. A raw-beam divergence term is needed to describe the inherent resonator properties when F^{-1} is essentially zero. It should be roughly proportional to the number of modes which can oscillate or the resonator Fresnel number. With a resonator having a curved or two curved end reflectors, this term is proportional to the raw-beam divergence value given by Eq. 11 and has a similar dependence on the resonator length and diameter.

b. A second raw-beam divergence term is needed describing the thermal focusing properties of the resonator which essentially deforms some of the resonator modes capable of oscillation.

c. A weighting factor is needed on this thermal focusing term due to nonuniform pumping, thermal distortion, and the possible mode structure due to the resonator geometry.

d. The equivalent focal length resulting from a combination of thermal focusing and optical focusing (due to end mirrors) is not validly summed as

$$F_{eq}^{-1} = \left(2F_{m1}\right)^{-1} + \left(2F_{m2}\right)^{-1} + \sum_{i}\left(F_i\right)^{-1} \tag{12}$$

because F_i--the intraresonator thermal focusing term--is a volume effect and not a surface effect, and being complex in nature is not summable as a simple lens effect. Also, since thermal stress and end-face curvature effects contribute to the thermal focusing effect, Eq. 10 for F_i is already an oversimplification. The first two terms at the right in Eq. 12, where 2F is the radius of curvature of an end reflector, should be incorporated in the term described in paragraph 5.a.

e. The raw-beam divergence figure should be a root-mean-square value rather than a sum.

The net result of these implications (and several others less evident) can be summarized in Eq. 13.

$$\theta_R = \left|(\Gamma)^2 + \beta(D/\sqrt{LF})^2\right|^{\frac{1}{2}} \tag{13}$$

$$\theta_R = \theta_o \left\{1 + \varepsilon\left[1 + \left(\Delta E_{in}/E_{in}\right)\right]F^{-1}\right\}^{\frac{1}{2}} \tag{14}$$

and for a resonator with L = 30 cm, D = 0.6 cm, the equation simplifies to what the author calls the Theta equation:

$$\theta_R = \theta_o \left\{1 + 11.5\left[1 + \left(\Delta E_{in}/E_{in}\right)\right]F^{-1}\right\}^{\frac{1}{2}} \tag{15}$$

where

$$F^{-1} = P_{in}/1785 = E_{in}\tau/1785$$

The factor θ_o is the experimental raw-beam divergence figure at the 1-Hz repetition rate (when F is very large and F^{-1} is essentially zero). For a resonator with a curved end mirror, θ_o varies directly as $D/\sqrt{LF_{eq}}$ as described earlier; whereas, for a resonator with flat end reflectors, θ_o is more dependent upon laser rod quality and the resonator Fresnel number. If θ_R is to be calculated as a function of pulse repetition rate (where the input energy per pulse does not change), then $\Delta E_{in} = 0$. If the resonator is operating at a fixed pulse repetition rate and the input energy per pulse increases from E_{in} to $(E_{in} + \Delta E_{in})$, then the term $[1 + (\Delta E_{in}/E_{in})]$ is no longer equal to unity. The value of F is then determined using the energy input level $(E_{in} + \Delta E_{in})$.

6. Table E.4-2 compares the Theta Equation results with the experimental results. The experimental data were taken mainly with laser rod #2; the Theta Equation shows the raw-beam divergence data for all three laser rods identified in Appendix .-7. Since the Theta Equation includes the dependence of resonator length and diameter on the raw-beam divergence value, such data could also be readily generated. The raw-beam divergence increase (relative to θ_o) due to increasing input energy as well as pulse repetition rate can also be calculated in unison. If two curved end reflectors are used (rather than just one), the equivalent focal length F_{eq} is given by Eq. 12 with $F_i = \infty$. The raw-beam divergence figure for a more complex combination of input energy (or power) and resonator physical properties change are all calculable using the Theta Equation. As stated earlier the parameter θ_o will vary directly as the lasing diameter and inversely as the square root of the product of the resonator length and end mirror radius of curvature. Since the Theta Equation is semiempirical and depends in part upon experimental data for its derivation, its validity over a more extended range of input and resonator variables will be tested whenever experimental data for such cases become available.

7. The most evident methods for improving the resonator raw-beam divergence are improving resonator efficiency (to increase F for a given output level) and, even more important, procuring laser rods with minimum θ_o. Since the efficiency improvement has a relatively low impact on the raw-beam divergence figure, emphasis should be placed on obtaining the best optical quality laser rods available.

TABLE E.4-2. Theta Equation Results Vs. Experimental Results.

Variables	Experimental*	Theta equation	
Beam divergence increase, mrad/Hz (with repetition rate at 8-J-input per pulse)	0.089 (FC-104)	0.089	Laser rod No. 1
	0.075 (FC-104)	0.067	No. 2
	0.066 (EGw)	0.078	No. 3
	0.0715 Av. value	0.067	No. 2
Beam divergence increase, mrad/J (with input energy at a 10-Hz repetition rate (fixed))	0.2	0.25	No. 1
	0.16	0.175	No. 2
		0.20	No. 3
	0.18 Av. value	0.175	No. 2

   * Most of the experimental results were obtained by using
laser rod No. 2.

NOTES:

1. The semiempirical equation was written to be consistent with the
    experimental results given in Appendixes A-7, C-1, C-2, C-4, C-5,
    C-6, and E-3.

2. The variation in θ_o is apparent from the laser rod comparison of
    Appendix A-7.

Appendix F

BEAM UNIFORMITY TESTS

Appendix F-1

NON-Q-SWITCHED BEAM UNIFORMITY TESTS

1. Tests were conducted to examine the resonator output beam uniformity for various resonator component changes including end mirror radius of curvature and the pump cavity shape. Tests were also made with the resonator detuned in both axes independently.

2. Figure F.1-1 shows the beam scan test apparatus. All data taken used an input energy of near 8.5 J, a xenon flashlamp (XG7), a common Nd:YAG laser rod, FC-104 coolant, a 70% flat-end mirror, and non-Q-switched operation at 10 pps. Only the pump cavity shape and the 100% end mirror were changed. The energy output from the resonator was typically 150 mJ. The scan aperture was 0.030 inch over an SGD-100 photodiode which was in a TO-5 can. The resonator output was centered in elevation on the TO-5 can using a varoscope for viewing. The scan rate was 0.78 inch per minute and was equivalent to 0.065 inch per division on the oscilloscope photographs (whose baseline rate was 5 sec/div). The scan photographs then provided a time-averaged beam uniformity profile. Sufficient time was allowed for the energy output to stabilize before the detector scan was initiated. Scanning was done toward the flashlamp side of the laser rod as shown, which was in the scan plane for all tests. Burn patterns were taken at the same time. The EG&G radiometer provided the means of monitoring the resonator relative output for tuning purposes.

3. "HORIZ" (Fig. F.1-1) shows the direction in which the resonator was misaligned for particular tests; the vertical misalignment was also made on this end reflector. A misalignment in the horizontal plane as shown should not cause significant lasing diameter reduction in the vertical plane. The energy in the horizontal plane should, however, be redistributed in the laser rod in the direction away from the flashlamp, since the mirror generally is redirecting energy (very slightly but very preferably) in that direction. In a similar fashion, a clockwise misalignment in the vertical plane (at the top of the end reflector) should redistribute the energy toward the bottom on the lasing diameter in the vertical plane but not cause significant lasing diameter change in the horizontal or scan plane. The burn patterns and scan photographs show support of this hypothesis. The burn patterns to be shown are inverted top-to-bottom so that the burn pattern and the scan photograph are both, from left to right, the result of what the photodiode encounters while being scanned toward the flashlamp side of the laser rod; i.e., the flashlamp lies at the right in both the burn patterns and the scan photographs.
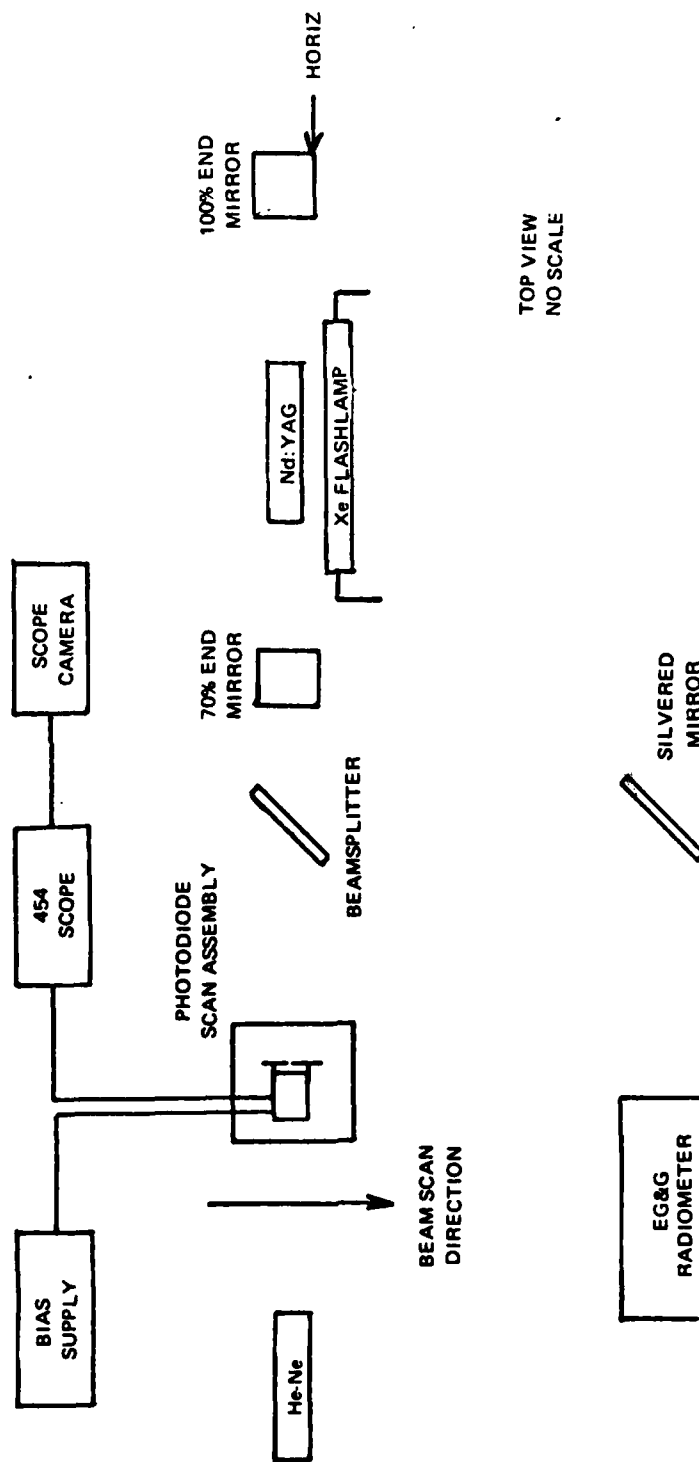
FIG. F.1-1. Beam Scan Test Apparatus.

4. Table F.1-1 is a summary of the experimental beam scan test results. The numbers at the left in the table correspond to a numbered scan photograph and its corresponding burn pattern and is used for cataloging purposes. All diameter measurements were made directly from the exposed Polaroid film using a scaled viewing magnifier. E_0 corresponds to the achievable resonator output when aligned. The aperture diameter of 0.030 inch was subtracted from the scan diameter and uniform lasing diameter, the latter of which was largely a fairly crude measurement necessarily. Representative beam scan photographs and burn patterns are given in Fig. F.1-2(a-e). From an examination of these figures, the following results can be seen:

a. The beam pattern gets narrower in the direction in which the resonator is misaligned, and the energy is redistributed in a direction away from the flashlamp as predicted earlier. (See Fig. F.1-2(a-c) Cases 12, 13, 20, 21, 26, and 27.)

b. A misalignment in a horizontal plane does not appreciably reduce the signal amplitude in that plane but does reduce the lasing diameter. (See Fig. F.1-2(a and b); Cases 20 and 21.) It does reduce the signal amplitude appreciably in the normal plane. (See Fig. F.1-2(b) Case 22.)

c. The curved mirror tendency to fold radiation back toward the lasing center is well known. The scan photograph of Fig. F.1-2(c), Case 26 shows this effect experimentally.

d. The burn pattern and the scan photograph show excellent correlation in detail. (See Fig. F1-2(a-c); Cases 12, 21, 26, and 27.)

e. The fine structure in the scan photographs is largely due to the laser pulse-to-pulse stability. (See Fig. F1-2(d); Case 9.) The photograph at the right is the energy output stability for a fixed aperture position; the camera was started at the time the laser was turned on for this particular test.

f. The roof prism tested did not lase particularly well near the roof edge, and the bimodal lasing structure normal to the roof edge is evident. (See Fig. F.1-2(d); Cases 7 and 8.)

g. A surprisingly small percentage of the rod is lasing uniformly. (See Table F.1-1 and all photographs, Fig. F.1-2(a-e).)
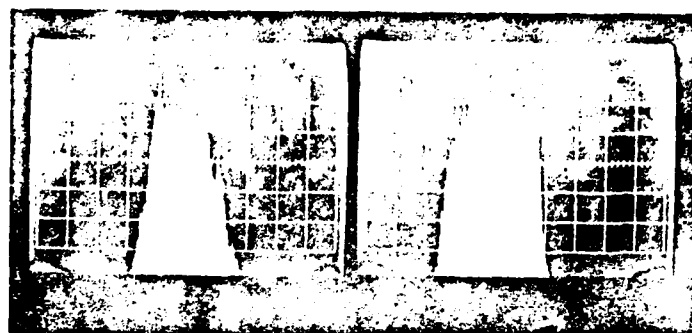
h. The flashlamp side of the scan pattern shows the nonuniform pumping effect due to the close proximity of the flashlamp. (See Fig. F.1-2 (a, c, and d); Cases 13, 20, 26, and 9.)

i. No correlation is possible in signal amplitude (at the photodiode) required for damage threshold on the film burn pattern.

j. For the aligned resonator cases, the pump uniformity for elliptical with inserts as compared to cylindrical shape is not significantly different for either curved or flat mirrors. (See Fig. F.1-2(a, c, d, and e); Cases 13, 20, 26, 9, 1, and 2.)
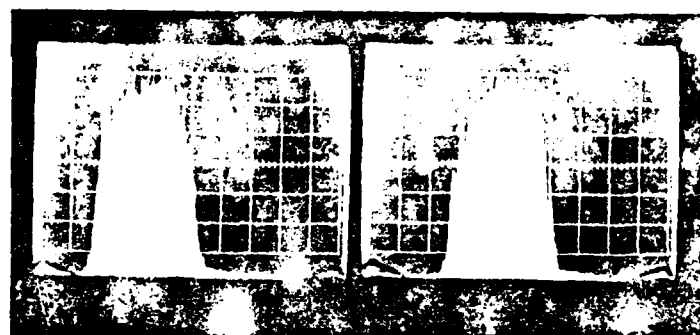
157

TABLE F.1-1. Test Data Summary.

| Case parameters	Burn diameter, in. (scan plane)	Scan diameter, in. (10% points)	Uniform lasing diameter, in. (20% points)
Elliptical with inserts:			
1. Aligned, 10-meter end mirror	N/A	0.252	0.156
2. Duplicate scan of Case 1	N/A	0.223	0.156
3. Misaligned to 0.6 E_o, 10 m, HORIZ ..	0.130	0.1?0	0.085
4. Case 3 at 0.8 E_o	0.170	0.212	0.141
5. Case 3 except VERT misalignment	0.175	0.178	0.065
6. Case 4 except VERT misalignment	N/A	0.195	0.085
7. Roof prism, aligned, scan perpendicular to roof edge	0.185	0.172	0.100
8. Case 7 except scan parallel to edge	0.145	0.143	0.041
9. Aligned, T-Beam 10-meter end mirror	0.210	0.238	0.143
10. 2 flats, misaligned to 0.8 E_o	0.150	0.219	0.098
11. 2 flats aligned	0.155	0.237	0.143
Cylindrical pump cavity:			
12. 2 flats, 0.75 E_o	0.140	0.210	0.100
13. 2 flats, aligned	0.160	0.217	0.160
14. Aligned, 10-meter end mirror	0.210	0.242	0.176
15. Misaligned to 0.8 E_o, 10 m, HORIZ ..	0.175	0.230	0.137
17. Case 15 except VERT misalignment ...	0.210	0.237	0.178
19. Case 17 with beamsplitter reversed	N/A	N/A	N/A
20. 2 flats, aligned, 2 scans	0.195	0.237	0.152
	0.200	0.235	0.143
21. Case 20 except 0.8 E_o, HORIZ, 2 scans	N/A	0.243	0.106
	0.175	0.232	0.104
22. Case 21 except VERT misalignment ...	0.195	0.230	0.158
	N/A	0.223	0.150
23. Aligned, 2 flats	0.200	N/A	N/A
24. Misaligned to 0.8 E_o, 2 flats, HORIZ	0.160	N/A	0.070
25. Aligned, 2 flats	0.195	0.237	0.152
26. Aligned, 10-meter end mirror	0.210	0.241	0.176
27. Misaligned to 0.8 E_o, 10 m, HORIZ ...	0.150	0.230	0.091
28. Case 27 except VERT misalignment ...	0.210	0.230	0.100

Case 12   Case 13

Case 20

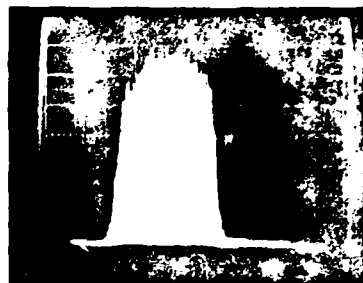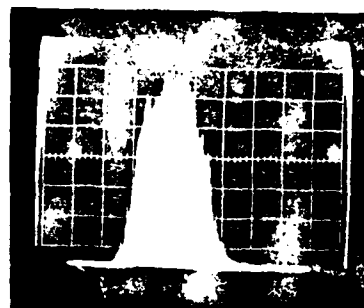FIG. F.1-2(a). Burn Patterns and Scan Photographs.
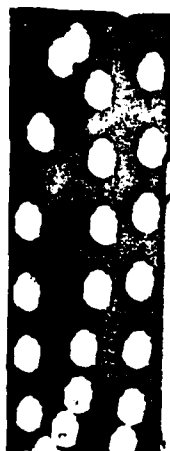
Case 21
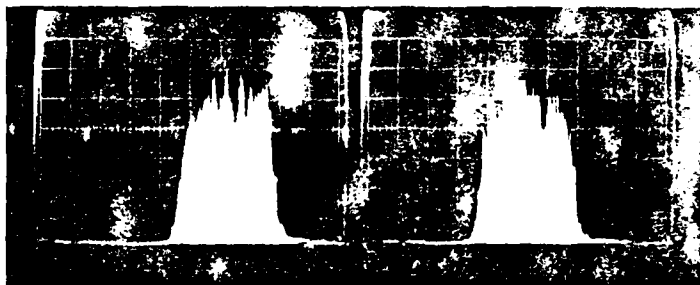
Case 22

FIG. F.1-2(b). Burn Patterns and Scan Photographs.
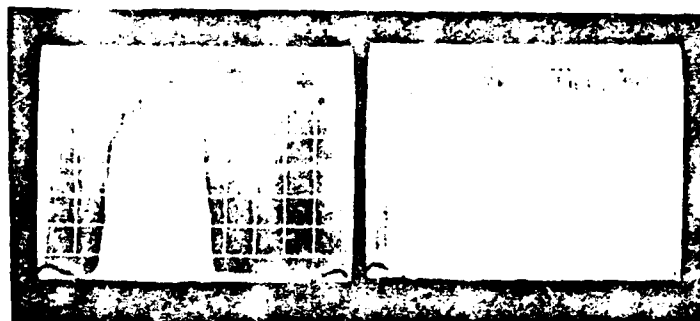
Case 26

Case 27

FIG. F.1-2(c). Burn Patterns and Scan Photographs.
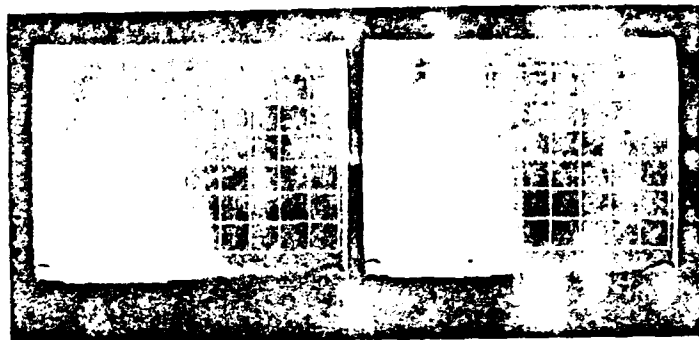
Case 9

Case 7   Case 8

FIG. F.1-2(d).   Burn Patterns and Scan Photographs.

Case 1   Case 2

Case 19

FIG. F.1-2(e). Burn Patterns and Scan Photographs.

k. The scan photographs are generally reproducible. (See Fig. F.1-2 (a and e); Cases 20, 1, and 2.)

l. The elliptical pump cavity with inserts has significantly better output stability than has the cylindrical pump cavity shape. The output stability is also better using curved mirrors rather than flat mirrors. This is attributed to the larger cross-sectional area for the cylindrical pump cavity shape where the coolant is exchanged less often; i.e., the coolant is exchanged about once every 4 and 10 pulses for the elliptical with inserts and the cylindrical pump cavity, respectively. The coolant flow pattern in the cylindrical pump cavity shape is less uniform than in the elliptical pump cavity.

m. From the discussion of paragraph 3, the data in Table F.1-1, and the photographs of Fig. F.1-2(a-e), the misalignment axis of a resonator is relatively predictable and allows at least a cursory evaluation of energy output reduction, for example, during the temperature tests of a resonator.

NOTES:

1. The non-Q-switched beam uniformity has very little similarity to the Q-switched beam uniformity.

2. Lasing diameter tests were made for a non-Q-switched resonator. These tests involved placing apertures of varying sizes in the resonator and measuring energy output versus aperture diameter. The tests showed that a 0.250-inch-diameter laser rod was lasing over a 0.233-inch diameter.

3. The small secondary "hump" shown by the arrow in Case 21 of Fig. F.1-1(b) was due to secondary reflection effects from the beamsplitter.

4. The roof prism used for these tests was also used in the reflector misalignment sensitivity tests of Appendix A-5. Undoubtedly the burn spots near the prism knife edge altered the lasing pattern significantly.

Appendix F-2

Q-SWITCHED BEAM UNIFORMITY TESTS

1. The output beam uniformity of a Q-switched Nd:YAG laser using four different flashlamp-laser rod pump-cavity coupling configurations is described in NWC TP 5315[1]. The test apparatus and the test procedure used to establish the beam uniformity parameter quantitatively are discussed in the report also.

2. A newly defined beam uniformity parameter M*--the ratio of maximum-to-average peak power density--has been shown to vary significantly for the pump cavities tested. The data obtained on beam uniformity are applicable toward (1) improving laser pump cavity design, (2) interpreting particular missile and seeker tracking behavior, and (3) comparing techniques for measuring laser-beam divergence. These data are also an aid to establishing the damage threshold level for retinal tissues and laser resonator components at 1.06 microns.

3. For complete details on this subject, see NWC TP 5315.

---

[1] Naval Weapons Center. *Beam Uniformity Measurements on Q-Switched Nd:YAG Lasers*, by Edward A. Teppo. China Lake, Calif., NWC, February 1972. (NWC TP 5315, publication UNCLASSIFIED.)

Appendix G

LASER COOLANT STUDIES

Appendix G-1

COOLANTS AND THEIR ULTRAVIOLET ABSORPTION

1. Tests were initiated on the new laser coolant, 2-methoxyethanol
(2-MOE). Since this coolant has a bond energy dictated by a C-H bond
(like ethylene glycol), a new xenon heliosil flashlamp is being used
with it. Preliminary tests indicate that its straight lasing efficiency
is nearly equivalent to that of FC-104 (with the well-used flashlamp)
as the coolant. So, it is anticipated that its Q-switched output will
be larger than that available from FC-104 due to its superradiating
character at an 8-J input level. The high viscosity of 2-MOE makes the
cooling system quite difficult to fill. No filter is used in the present
breadboard cooling system, inasmuch as this coolant reacts mildly with a
molecular sieve filter. However, it reacts violently with MgLi alloy.

2. From 29 December 1970 to 19 January 1971, some 50,000 shots were
put on a xenon heliosil flashlamp used with 2-MOE coolant and a typical
energy input of 8 J/pulse. Figure G.1-1 shows the transmission of this
coolant after use and the transmission as a function of incident wavelength
of a pure unused sample. In essence, the coolant absorbs the flashlamp
radiation above the flashlamp cutoff wavelength, which is also indicated
on the transmission curve. Figure G.1-2(a and b) shows, for comparative
purposes, the transmission of the 2-MOE coolant after 200,000 shots at a
nominal 10-J input level to the flashlamp. In terms of cooling system
performance, the absorption of this high-energy radiation (low wavelength)
by the coolant is desirable. Unfortunately, the increased UV absorption
is indicative of increased coolant degradation as well. As the coolant
begins to absorb strongly in the UV (at wavelengths higher than the flash-
lamp envelope cutoff) it degrades very rapidly. This degradation in turn
causes a reduction in lasing efficiency, mainly due to coolant reaction
with cooling system materials.

3. The performance of EGw as compared to FC-104 is described in part
in Appendixes C-2 and C-4. A 50-50 mixture of ethylene glycol/water
(EGw) has been used in the T-beam resonator performance tests. Although
EGw has not been used previously by our laser group, its thermal conducti-
vity, its specific heat, its superradiance limit, its compatability with
a silvered surface, and its extensive use in other designators warrants
its use in the PADS unit. The quality of FC-104 coolant after use was
related to its spectral absorbence cutoff wavelength (which increased as
the coolant degraded). This cutoff wavelength increased rapidly when it
exceeded the cutoff wavelength of the flashlamp (which is determined by
the envelope material used). Figure G.1-3 shows the spectral absorbence
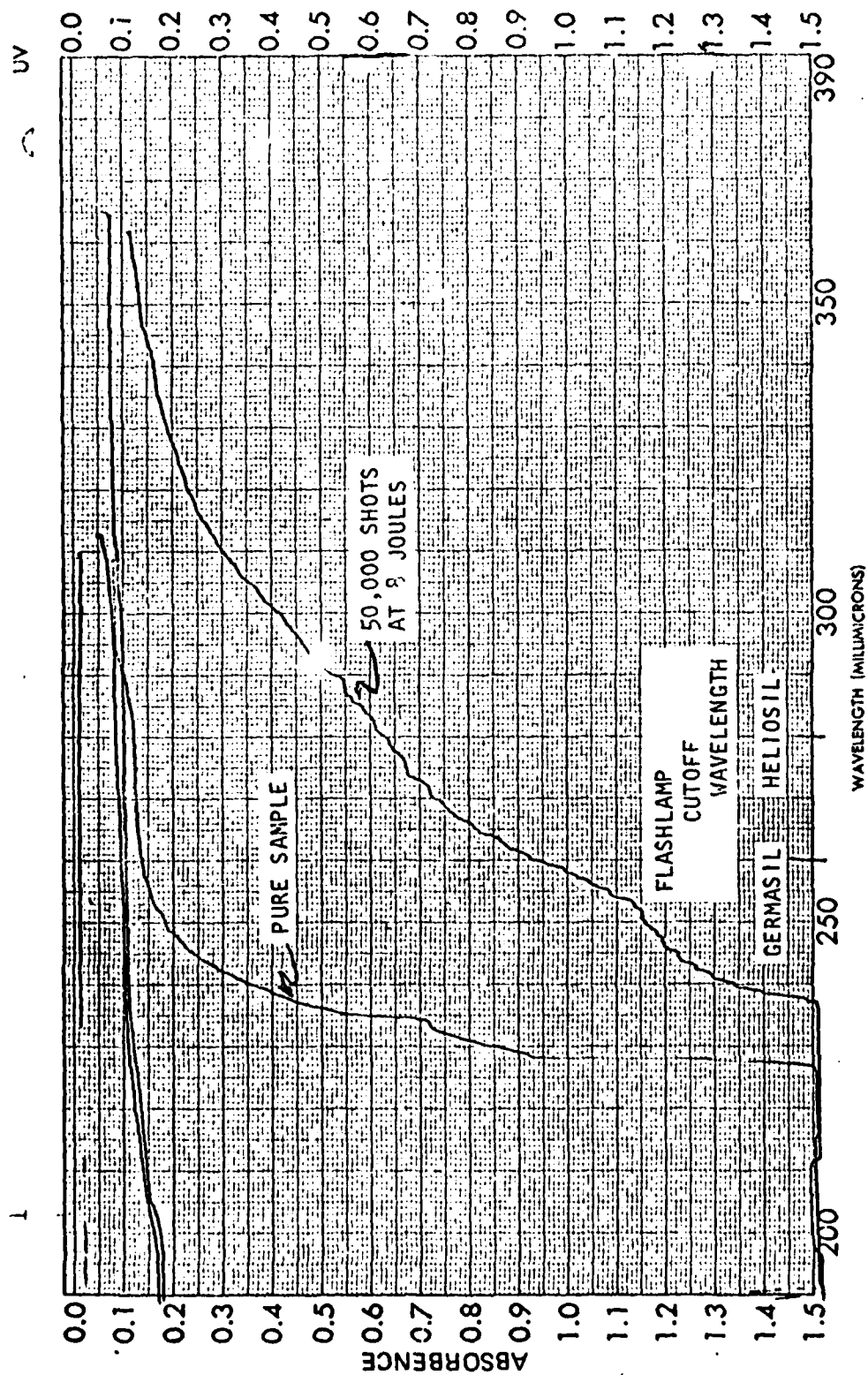of EGw for both pure and irradiated samples. Sample #1 was taken from
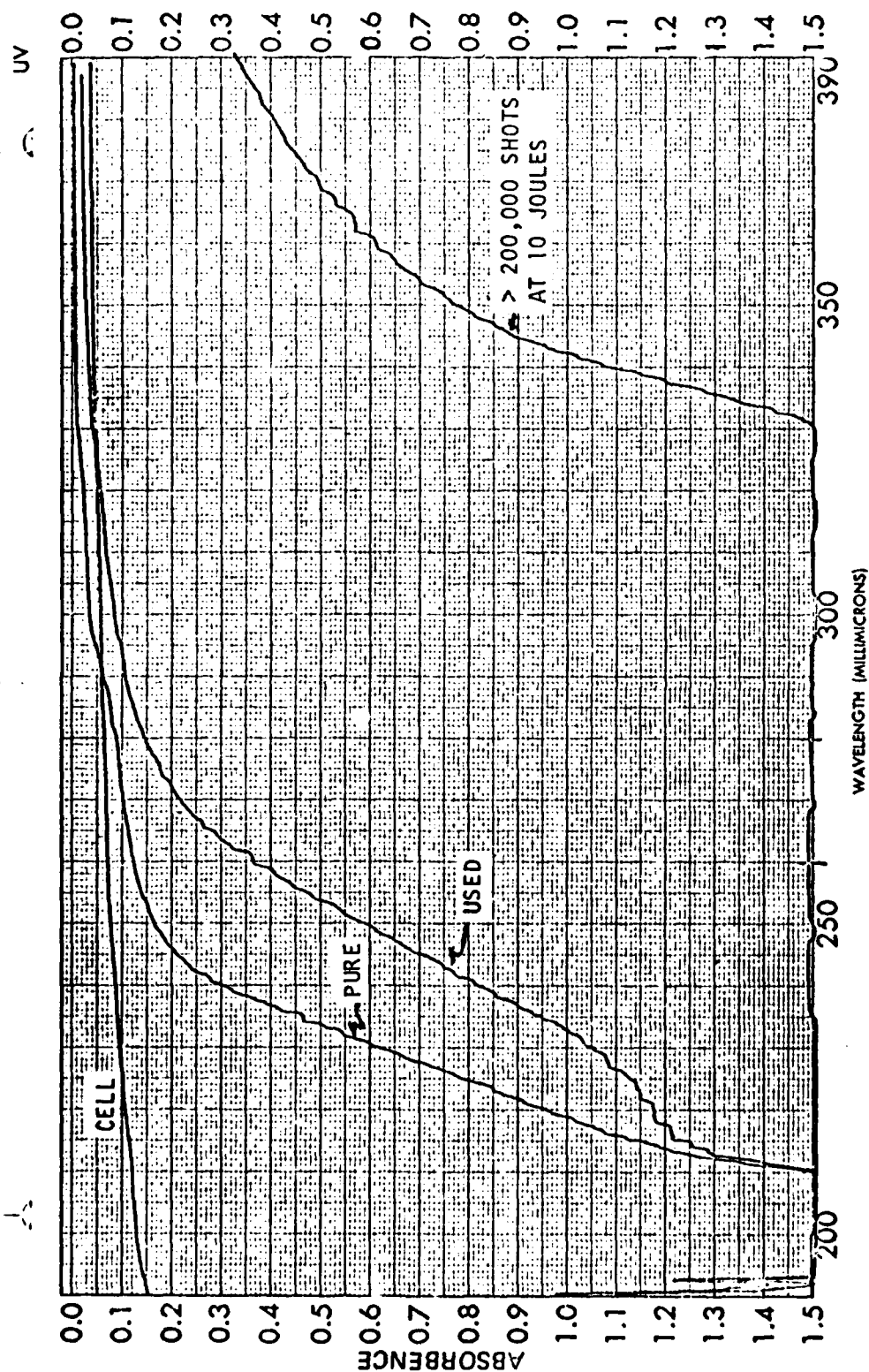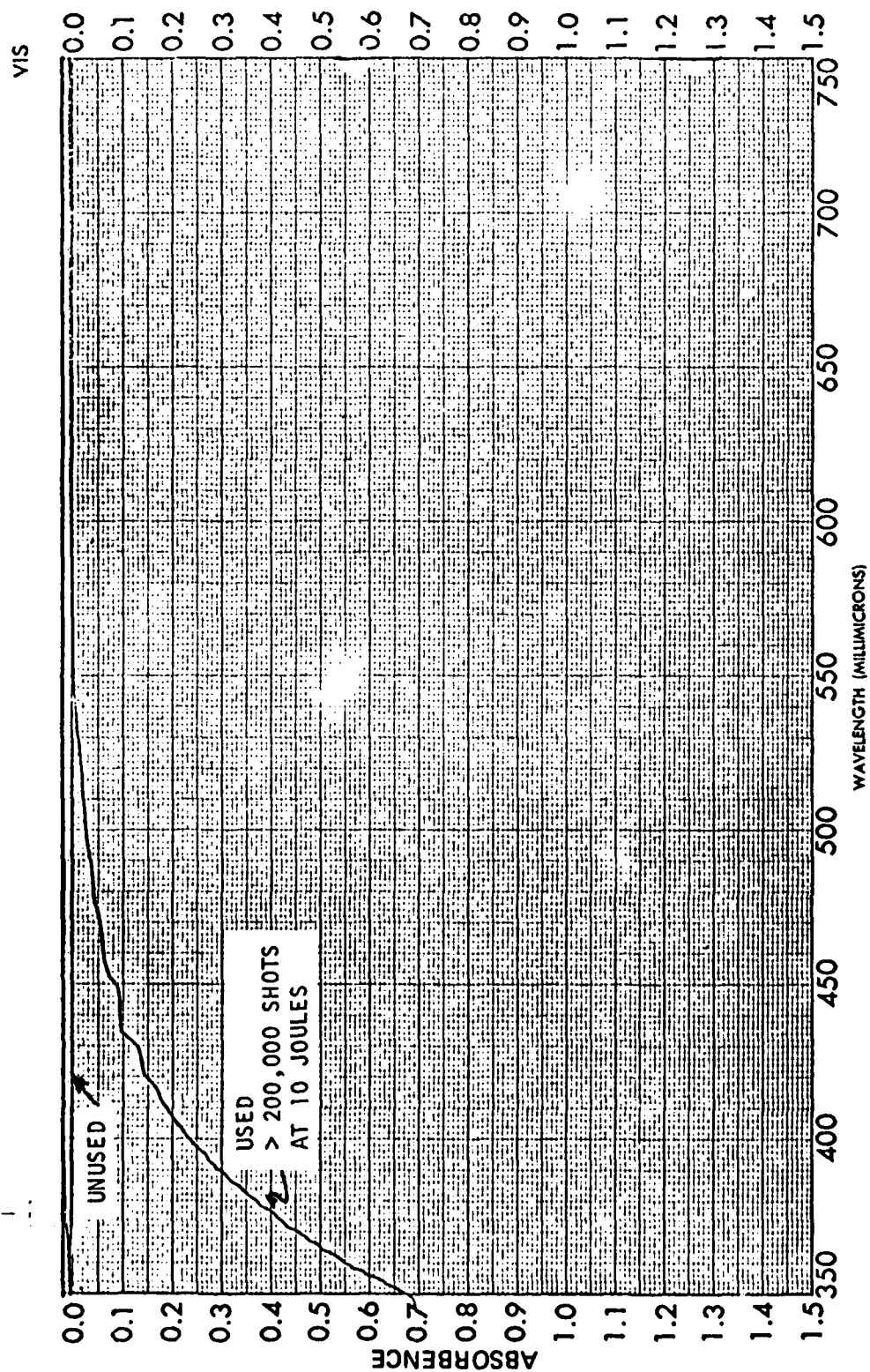
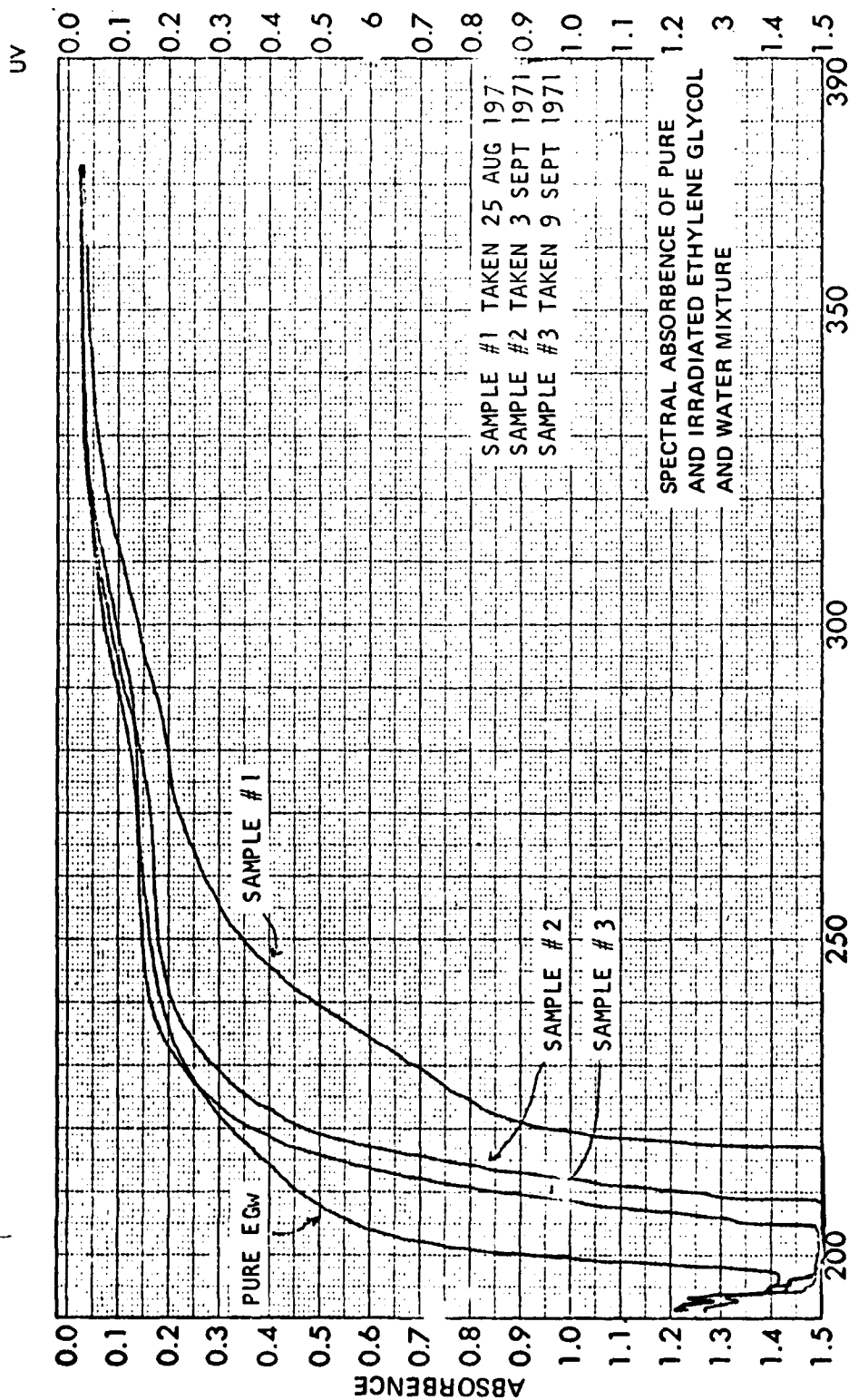FIG. G.1-1.

FIG. G.1-2(a).

FIG. G.1-2(b).

FIG. G.1-3.

SPECTRAL ABSORBENCE OF PURE
AND IRRADIATED ETHYLENE GLYCOL
AND WATER MIXTURE

SAMPLE #1 TAKEN 25 AUG 197
SAMPLE #2 TAKEN 3 SEPT 1971
SAMPLE #3 TAKEN 9 SEPT 1971

the pump cavity after approximately one month of regular use and indicates
that the EGw is absorbing little flashlamp radiation after this period of
use. (Although more shots were used on samples #2 and #3, their reduced
absorption is due to the fact that some irradiated EGw was replaced with
pure EGw when the pump cavity was removed. The spectral absorbence of
the irradiated EGw of sample #1 is similar to that of pure FC-104. The
wavelength cutoff of the flashlamp envelope is near 2600Å.

NOTES:

1. The coolant, 2-MOE, was tested extensively in nonlasing tests at the
    Naval Missile Center, (NMC) Point Mugu, California. It was shown to
    be thermally stable at operating temperatures of 200°F for 2 hours.
    Coolant performance was judged qualitatively by examining cooling
    system components and the pump cavity walls. UV absorption tests
    were not made at NMC.

2. The term *superradiance* is used to describe the effect of amplified
    off-axis spontaneous emission that changes the slope of the lasing
    efficiency curve, i.e., input versus output energy dependence.
    Lateral depumping is a more descriptive term for this lasing effi-
    ciency reduction.

Appendix G-2

THERMAL EFFECTS ON THE RESONATOR PERFORMANCE

1. The thermal misalignment of the resonator using FC-104 coolant was described in Appendixes C-2, C-3, and C-4. The pump cavity shape can affect the thermal misalignment magnitude from simple thermal considerations. Two pump cavity shapes were tested and compared as to thermal misalignment magnitude. The improvement in an elliptical pump cavity is that the coolant is exchanged more often (about every 4 output pulses at 10 pps repetition rate compared to about once every 10 pulses in a cylindrical configuration) because of its reduced cross-sectional area. This should reduce the thermal heating and lensing effect in the laser rod. The output stability plots of Fig. G.2-1 show this dramatically. (Most of the detailed oscillations in the output stability can be attributed to the measuring equipment itself and are not relevant here.) In both cases the resonator was aligned for maximum output after thermal equilibrium was established. The pump cavity environs were cooled to the ambient temperature and the plot of energy output versus time was started. Note that the elliptical pump cavity output immediately starts at about 90% of the achievable output number; whereas the cylindrical pump cavity configuration starts at about 50% of maximum output energy, and in about 10 seconds reaches its achievable output level. The energy output levels for the cylindrical and elliptical pump cavity configurations were 120 and 76 mJ, respectively.

2. An estimate of the magnitude of the thermal misalignment at the 10 pps repetition frequency is important to an understanding of the thermal distortion in the laser rod. Also of importance and related to this subject are the findings regarding the direction of the misalignment and the resultant redistribution of energy in the resonator as a result of this thermal misalingment. The raw-beam divergence measurements at 1 pps required that the resonator be tuned (realigned) from the 10 pps end-mirror setting. When the resonator was tuned for optimum 10 pps operation, then operated at 1 pps, the output energy was reduced about 50%, and the burn pattern showed a redistribution of resonator energy toward the top, flashlamp side of the laser rod. The end-mirror alignment correction needed to compensate for this thermal misalignment of the resonator at 10 pps was estimated for both the cylindrical pump cavity and the elliptical pump cavity shape with inserts. The former required an adjustment of about 30 arcsec in elevation and less than 10 arcsec in azimuth; the latter about 15 arcsec in elevation and less than 10 arcsec in azimuth. This optical wedge effect then essentially misaligns the resonator by some 20 or 30 arcsec and the energy output achievable is not reached until this thermal misalignment process is completed. The axes of this misalignment orientation is neither parallel nor perpendicular to the laser rod-flashlamp plane.
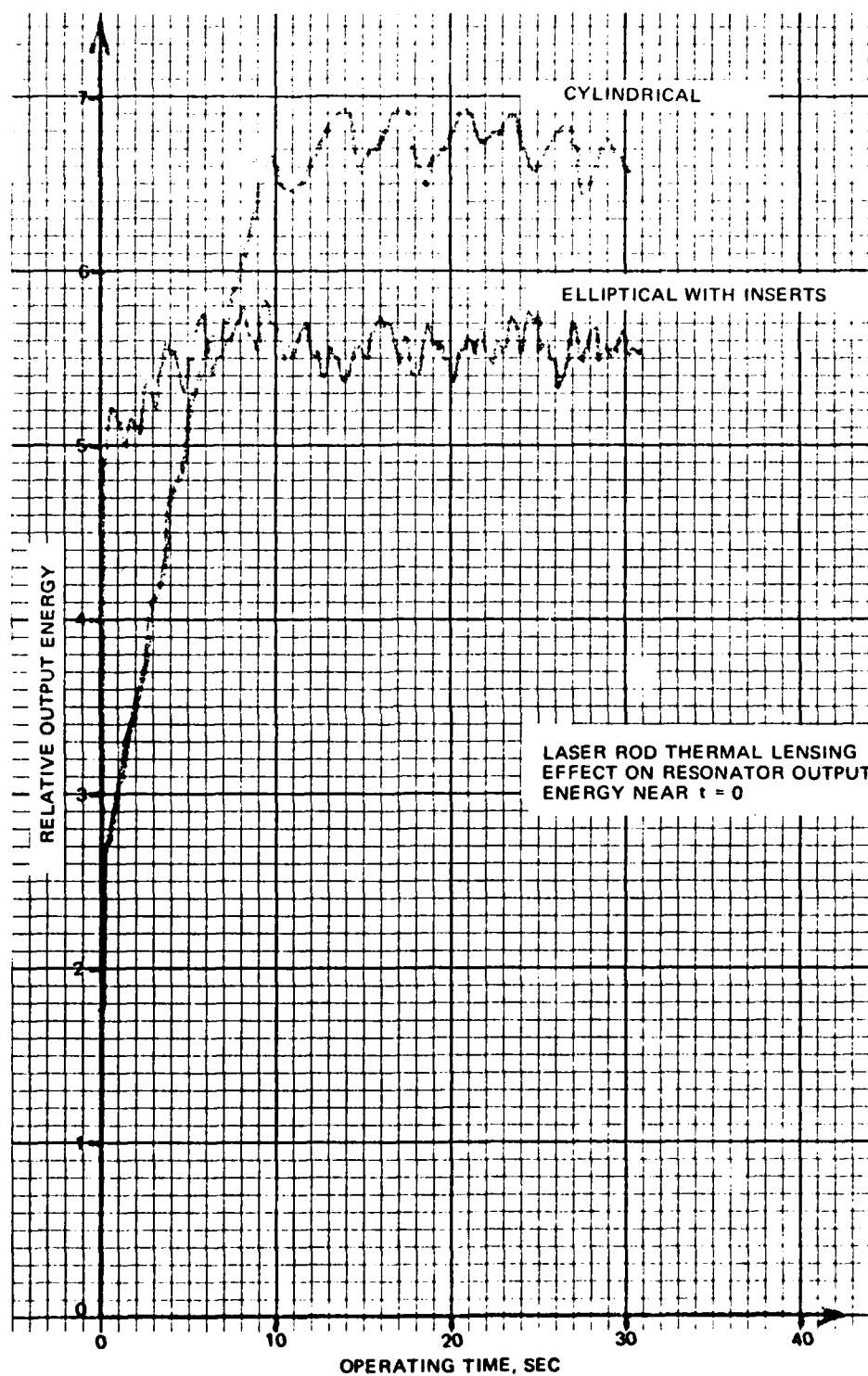
173

FIG. G.2-1. Thermal Misalignment Effect for Two Coupling Configurations.

NOTES:

1. The thermal effects described here are characteristic of the fluorocarbon (FC-104) and not of the ethylene glycol/water (EGw) coolant.

2. Coolant baffles in the pump cavity have been shown to reduce the thermal misalignment problem encountered with the use of the FC-104 coolant.

Appendix H

RELATED SUBJECTS

Appendix II-1

LOW-REPETITION-RATE TEST FACILITY

1. The purpose of the low-repetition rate test facility is threefold: (1) to allow the evaluation of pumping enclosure performance including comparison of laser rods, flashlamps, coupling geometries, and coolants independently; (2) to allow tests on delayed triggering of flashlamps; and (3) to provide a means of performing active tests on laser rods and flashlamps as a part of the incoming inspection procedure. No lasing in these tests is required, and it is intended that the integrated (laser rod) 1.06-µ fluorescence will be usable as a measure of achievable laser resonator output.

2. The power converter schematic developed for use in this test facility is shown in Fig. II.1-1. The power converter was derived from modifications to a laser rangefinder unit. The main energy storage capacitor is charged to a selectable voltage by the Ne68A which controls relay operation in the primary drive circuit. The variable voltage-divider network in the flashlamp trigger circuit ensures flashlamp-triggering for energy inputs as low as a few joules for both krypton and xenon flashlamps. The capacitor voltage is measured with a digital voltmeter.

3. The total integrated 1.06-µ fluorescence is a measure of the achievable laser output per pulse from the pumping cavity. Therefore, by placing the pumping enclosure and a narrow bandwidth 1.06-µ filter at the front of an integrating detector circuit (in a fixed geometry), a comparison of pumping enclosure geometries and components in terms of relative achievable output energy seems feasible. Since a plot for energy input to the main storage capacitor to energy output from the laser resonator is linear (assuming that superradiance is not a limiting factor) the integrated fluorescence voltage should be linear with input energy as well. Also, the fluorescence voltage at threshold for krypton versus xenon flashlamps should be proportional to the lasing threshold. The tests have been plagued with difficulties thus far including flashlamp radiation at 1.06µ, noise integration, and nonreproducibility of data from day to day. However, since the data taken during a single day seem reproducible, this integrated fluorescence technique is still being pursued. The flashlamp light output signal, weighted with the detector's spectral response, was attenuated by a factor of fifty relative to the 1.06-µ fluorescence waveform.

4. Further testing is planned to establish a reliable method of using the integrated fluorescence as a measure of pumping cavity performance. If successful, this technique would provide a means of comparing some resonator components directly. Planometric tests are being conducted as an alternate attempt of integrating the fluorescence voltage waveform.

FIG. H.1-1.

5. (Note: International Lamp Corporation, Inc. has developed a test
station which provides comparative information on flashlamp performance
by measuring peak fluorescence output voltage.)

Appendix II-2

WOUND INDUCTOR PER ORMANCE

1. Some inductors we'c tested for use in the L'IL unit. Since space is already at a premium, an air core inductor is prohibitive in size. All tests with powdered iron cores were found to reduce the energy output relative to an air core by some 40% or so. It was decided to test an inductor wrapped on the Sprague capacitor itself. The Sprague capacitor has an inductance of 22.9 μF; the wrapped inductance was measured as 28 μH. The measured output energy was 156 mJ for an 8.9-J input energy. This point lies on the same efficiency curve as does C = 18.8 μF, L = 33.7 μH. Hence, no degradation in output energy occurs using the wrapped capacitor approach.

Appendix H-3

RESONATOR EFFECTIVE REFLECTIVITY

1. In an end-dump laser resonator, the effective reflectivity of the resonator is that of the partially transmitting end reflector. In a two-element TVR resonator, the effective reflectivity is determined by the orientation of the quarter wave plate. For the T-beam resonator length, the energy output as a function of the effective reflectivity is shown in Fig. H.3-1.

2. The data apply to an energy input of 8 J per pulse. An increased input energy tends to decrease the optimum reflectivity value.
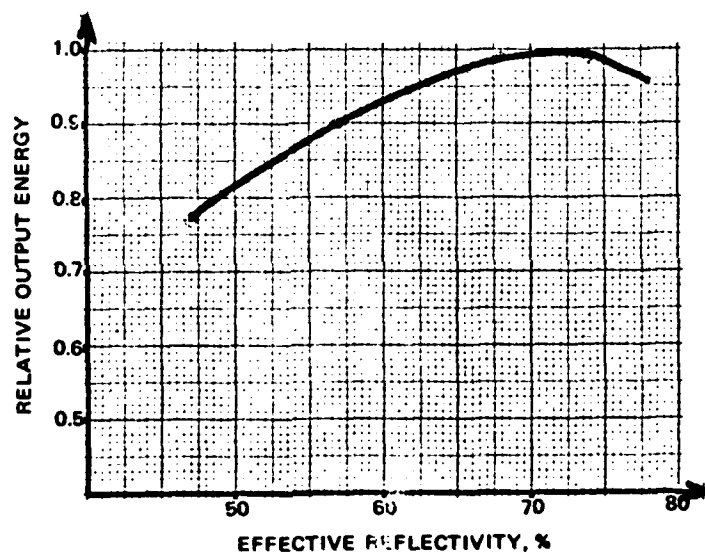

FIG. H.3-1. Relative Output Energy as a Function of Effective Reflectivity of the Resonator.

Appendix H-4

REPORTS IN PROGRESS

Tasks in the Nd:YAG laser lab presently in progress are listed with the objective of the individual task. This work will be documented and published at a later date.

Improved Extinction Ratio Tests: To reduce the likelihood of damage to modulator and to simplify modulator drive circuit.

Reduced Beam Divergence Resonator Tests: To improve resonator raw-beam divergence by thermal lens optical compensation.

"Keep Alive" Flashlamp Drive Circuitry: To improve laser efficiency and reliability.

Improved Pump Cavity Design: To improve laser efficiency; to reduce cost of pump cavity; to improve maintainability.

Dye-Enhanced Organic Coolants: To improve laser efficiency and pump cavity thermal properties and to compare with FC-104 coolant.

INITIAL DISTRIBUTION

7 Naval Air Systems Command
   AIR-360E (1)
   AIR-503E (2)
   AIR-5109C (1)
   AIR-604 (2)
2 Naval Ordnance Systems Command (ORD-0632)
1 Chief of Naval Research, Arlington (ONR-461)
1 Naval Air Test Center, Patuxent River
1 Naval Missile Center, Point Mugu
1 Naval Research Laboratory
1 Naval Weapons Laboratory, Dahlgren
2 Army Electronics Command, Fort Monmouth (M. Mirachi, J. Strozyk)
4 Army Missile Command, Redstone Arsenal
   N Bell (1)
   Dr. Emmons (1)
   G. Widenhofer (1)
   Redstone Scientific Information Center, Dr. Kobler (1)

On-Center:

  1 Code 122
  1 Code 222
  4 Code 3041
  1 Code 40
  1 Code 4013
  5 Code 405
  2 Code 40507
15 Code 4051
  2 Code 4052
  2 Code 4054
  2 Code 4056
  2 Code 4057
  1 Code 6041